THERMAL TRANSPORT AT CARBON NANOTUBE AND GRAPHENE INTERFACES USING ATOMISTIC MODELS

A Dissertation
Presented to
The Academic Faculty

by

Liang Chen

In Partial Fulfillment
of the Requirements for the Degree
Doctor of Philosophy in the
School of Mechanical Engineering

Georgia Institute of Technology
May 2015

THERMAL TRANSPORT AT CARBON NANOTUBE AND GRAPHENE INTERFACES USING ATOMISTIC MODELS

Approved by:

Dr. Satish Kumar, Advisor
School of Mechanical Engineering
Georgia Institute of Technology

Dr. Seung Soon Jang
School of Material Science and Engineering
Georgia Institute of Technology

Dr. Andrei G Fedorov
School of Mechanical Engineering
Georgia Institute of Technology

Dr. Azad Naeemi
School of Electrical and Computer Engineering
Georgia Institute of Technology

Dr. Samuel Graham
School of Mechanical Engineering
Georgia Institute of Technology

Date Approved: May, 2015

FOR MY MOTHER

ACKNOWLEDGEMENTS

Looking back at my six years' PhD life, I feel it is a hard but enjoyable journey. I find PhD life has redefined myself and allow me to explore the future with perseverance, courage and intellectual capability. At this moment, I would like express my appreciation and thanks to the people who have provide help and support to me during the PhD program.

Firstly, I would like to thank my advisor Dr. Satish Kumar. You have been a tremendous mentor for me. I would like to thank you for encouraging my research and for allowing me to grow as a research scientist. Your advice on both research as well as on my career have been priceless.

I would like to extend my appreciation to committee members: Dr. Samuel Graham, Dr. Andrei Fedorov, Dr. Seung Soon Jang, and Dr. Azad Naeemi for providing valuable research advice and insightful comments for the improvement of this work. I would like to express my special thank and appreciation to Dr. Zhuomin Zhang who has provided valuable advice and support to me during my hard times. I would like to thank Dr. Zhen Huang for their collaboration in several parts of this work. I am also very thankful to my colleagues Man Prakash Gupta, Owen Sullivan, Matthew Redmond, David Brown, and Zhequan Yan for providing a great company

My parents, Jianhai Chen and Fanai Chen, and my brother, Xiao Chen, have always been very supportive of my life and assisted enormously towards my personal, professional and spiritual development. I can never thank you enough for all of your love and encouragement during these years.

Table of Contents

LIST OF TABLES

LIST OF FIGURES

LIST OF SYMBOLS AND ABBREVIATIONS

Abbreviations

AGF	Atomistic Green's function
ACF	Auto-correlation function
BTE	Boltzmann transport equation
CNT	Carbon nanotube
CN-TFT	Carbon nanotube network thin-film transistor
CVD	Chemical vapor deposition
DFT	Density functional theory
DOS	Density of states
DWNT	Double-wall carbon nanotube
EAM	Embedded atom method
ELF	Electron localization function
FET	Field effect transistor
GFET	Graphene field effect transistor
GNR	Graphene nano-Ribbon
GULP	General Utility Lattice Program
HCACF	Heat current auto-correlation function
HOPG	Highly ordered pyrolytic graphite
IFC	Interatomic force constant
LA	Longitudinal acoustic
LAMMPS	Large-scale Atomic/Molecular Massively Parallel Simulator

LD	Lattice dynamics
LED	Light-emitting diode
LO	Longitudinal optical
MD	Molecular dynamics
MFP	Mean free path
MLG	Multilayer graphene
MLWF	Maximally localized Wannier functions
NEMD	Non-equilibrium molecular dynamics
NPT	Isothermal-isobaric ensemble
NVE	Micro-canonical ensemble
NVT	Canonical ensemble
PCFF	polymer consistent force field
RBM	Radial breathing mode
REBO	Reactive empirical bond-order
RTA	Relaxation time approximation
SED	Spectral energy density
SLG	Single-layer graphene
SMRT	Single mode relaxation time approximation
SWNT	Single-wall carbon nanotube
TA	Transverse acoustic
TBC	Thermal boundary conductance
TO	Transverse optical
VASP	Vienna *ab initio* package

ZA	Out-of-plane acoustic
ZO	Out-of-plane optical
vdW	van der Waals

Symbols

C	Specific heat
D	Dynamical matrix
E	Energy functional
E_f	Fermi energy
$\vec{F}$	Force vector
G	Green's function
H	Harmonic matrix
I	Identity matrix
J	Heat flux
L	Length
$\hat{L}$	Differential operator
N	Number of atoms, Bose-Einstein distribution
T	Kinetic energy functional, temperature
V	Interatomic potential, volume
a	Lattice constant
d	Diameter, distance between graphene and substrate
e	Energy density
e''	Energy flux

f	Scaling factor of interatomic force constants, Fermi-Dirac distribution
g	Velocity spectrum
$\hbar$	Planck constant
k	Electron wave vector, thermal conductivity
k_B	Boltzmann constant
m	Atom mass
p	Momentum
q	Phonon wave vector
$\vec{r}$	Atom position vector
t	Time
u	Atom displacement
$\ddot{u}$	Atom acceleration
v	Phonon group velocity
0^+	Small positive infinitesimal factor

Greek Letters

Φ	Second-order force constant matrix
Γ	Phonon escape rate in Green's function
Ψ	Wave function
Θ_D	Debye temperature
Ξ	Transmission function
χ	Scaling factor in Lennard Jones potential model

γ	Half-width at half-maximum of Lorentzian function
δ	Dirac delta function
ε	Strength parameter in Lennard-Jones potential
σ	Thermal conductance, distance parameter in Lennard-Jones potential
ρ	Electron density
θ	Spectral energy density
τ	Phonon lifetime, correlation time, relaxation time
υ	Phonon polarization
ω	Angular frequency

Superscript and Subscript

L, D, R, C	Left, device, right, and contact
ph	Phonon
xc	Exchange-correlation functional
α, β, γ	Indices of directions in Cartesian coordinate
i, j, k	Indices of atoms in a unit cell
l	Indices of unit cells

SUMMARY

Thermal transport at the interfaces of low-dimensional carbon nano-structures such as carbon nanotube (CNT) and graphene become very important in their nano-electronic devices. Phonons are primary heat carriers in CNTs and graphene; a fundamental understanding of phonon transport in these nano-structures and their interaction with electrons is required for the energy efficient design of their devices. In this work, atomistic simulations have been performed to investigate thermal transport at interfaces of CNT and graphene that are typically encountered in their applications, *e.g.*, CNT-CNT junctions on silicon oxide (SiO_2) substrate, interfaces between shells of double-wall CNTs (DWNTs), and graphene-metal/graphene-SiO_2 interfaces.

Heat dissipation at CNT junctions supported on the SiO_2 substrate is studied using molecular dynamics (MD) simulations by applying steady or transient heating power to CNTs. Inefficient heat transfer at CNT-CNT junctions is demonstrated by comparing temperature responses of different junction structures under high heating power. Spectral temperature decay in CNTs further elucidates the frequency dependence of phonon coupling at interfaces between the CNTs, and interfaces between the CNT and substrate. The energy exchange and coupling of the vibration modes between layers of DWNTs is then investigated using MD simulations in the framework of travelling wave packets. The spatiotemporal profiles of kinetic energy components and frequency spectrum of velocities are analyzed to identify the modes of radial vibration that are strongly coupled and can efficiently exchange energy between layers of DWNTs.

Effects of metal substrates on thermal transport in single layer graphene (SLG)

are investigated by computing thermal conductivity of suspended SLG and SLG supported on Cu using Green-Kubo method and relaxation time approximation (RTA) approach. The role of different phonon modes is explored by estimating phonon lifetimes and by comparing the corresponding contribution to the thermal conductivity.

The frequency dependent phonon transmission and thermal boundary conductance (TBC) across SLG/metal or multilayer graphene (MLG)/metal interfaces are determined using Green's function (AGF) calculations and density functional theory (DFT). The work shows how the bonding strength changes the graphene/metal and graphene/graphene phonon coupling, and demonstrated the transition of thermal transport mechanism from metal/graphene dominated resistance to graphene/graphene dominated resistance as the metal/graphene bonding strength increases in metal/MLG/metal structure.

CHAPTER 1

INTRODUCTION

In recent decades, advanced fabrication and characterization techniques have facilitated the development of novel carbon nanostructures including carbon nanotubes (CNTs) and graphene, and excited worldwide interest in their engineering applications. In carbon nanostructure based electronic devices, efficient thermal management can become challenging in achieving high performance due to high heat dissipation [1]. In electronic devices such as field effect transistors, field emission displays, and X-ray/microwave generators, efficient heat removal is required for reliable and long-life operation. Energy conversion or storage devices such as thermoelectric cooler, thermo-galvanic cell and super capacitor require low thermal resistance of the electrode material and at their interfaces to achieve high conversion efficiency and power density. A fundamental understanding of thermal transport in nanostructures is of great importance for improved heat dissipation in these devices [2]. In this chapter, the structure of CNTs and graphene is first introduced, followed by a brief description of their applications in electronic devices where their unique electronic and thermal properties are of great interest. Then atomistic models for analyzing thermal transport in nano-structures are introduced. Finally, the motivations, objectives and outlines of the current work are discussed.

1.1 Structure of Carbon Nanotubes and Graphene

Among many allotropes of carbon, CNT and graphene exhibit exceptional thermal, electrical and mechanical properties due to their unique structures The discovery

of multi-wall carbon nanotubes (MWNTs) is reported by Iijima in 1991 [3], and the single-wall carbon nanotubes (SWNTs) is first synthesized in 1993 [4]. As shown in Figure 1.1, a SWNT can be described by a single layer of carbon atoms in honeycomb lattice that is rolled up to a seamless cylinder with extremely high length-to-diameter ratio [5]. The pristine SWNT has exceptional electronic properties such as ballistic conductance and semiconducting properties due to the overlap between π-bonds which spans in the direction normal to the shell. The strong σ-bonds between carbon atoms result in very high mechanical strength. The thermal properties of SWNTs are also remarkable because of the 1D ballistic transport of phonons. A MWNT, as shown in Figure 1.1 (b), consists of several concentric SWNTs. While SWNTs can be either semiconducting or metallic depending on its chirality, MWNTs are generally metallic. Double-wall carbon nanotubes (DWNTs) have gained special attention because they have similar properties as that of SWNTs but their chemical resistance can be significantly improved [6].

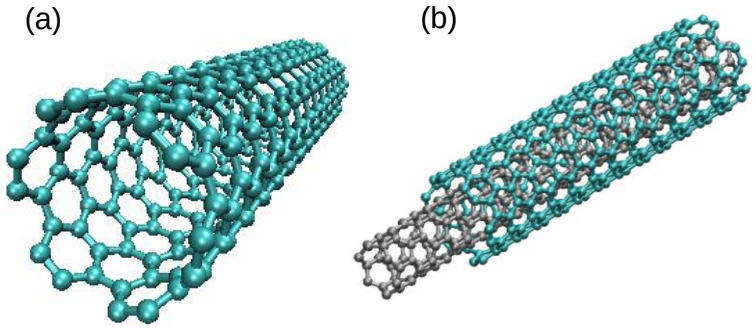

Figure 1.1 Schematic of carbon nanotubes (a) single wall carbon nanotube; (b) multiwall carbon nanotube

Graphene is a two-dimensional (2D) material which is first prepared using exfoliation method from bulk graphite by Geim and Novoselov in 2004 [7]. As shown in Figure 1.2, the single layer graphene (SLG) is a single atomic planar sheet which consists of sp^2 bonded carbon atoms in honeycomb lattices. Similar to CNTs, graphene also has extraordinary electronic, mechanical and thermal properties. The overlay of $2p_z$ orbitals between bonded carbon atoms in graphene leads to high electron mobility but zero bandgap, as shown in Figure 1.2 (a). Various methods such as doping, functionalization and oxidation can help to open the gap in Dirac cone. A sizable bandgap can be opened by making graphene narrow ribbons (GNRs) with sharp edges, as shown in Figure 1.2 (b). The bandgap of multi-layer graphene (MLG) can be tuned by controlling the stacking order while maintaining high carrier mobility. Figure 1.2 (c) shows a bilayer graphene which consists of two coupled monolayers with atoms arranged in 'dimer' sites.

Currently, CNTs and graphene are commercially available. The synthesis, purification and fabrication techniques have been advanced in the recent decade. Techniques such as arc discharge, laser ablation and chemical vapor deposition (CVD) are among popular methods to synthesize CNTs with controllable properties. In addition to exfoliation method, epitaxy and CVD have been developed to produce large-area, high-quality and uniform graphene monolayers. In order to achieve tunable electronic structures, the fabrication of MLG with specific stacking orders and GNR with controlled shaped has attracted enormous attentions.

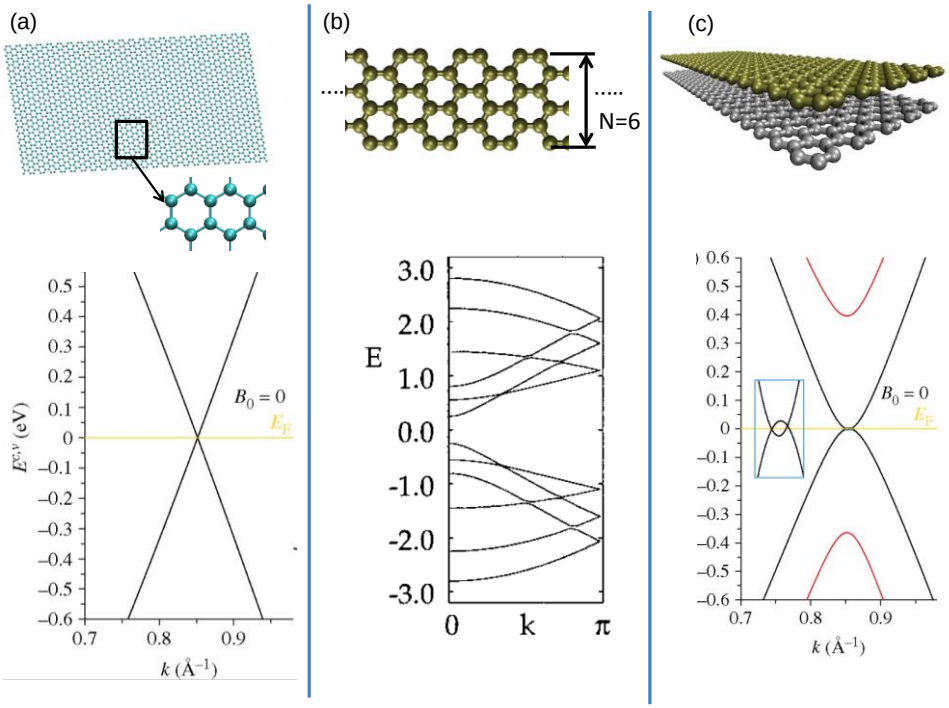

Figure 1.2 Schematic and electronic band structures of (a) single layer graphene [8]; (b) graphene nanoribbon [9]; (c) bilayer graphene [8]

1.2 Electronic Devices of Carbon Nanotubes and Graphene

1.2.1 Carbon Nanotube Thin Film Transistors (CN-TFTs)

Thin film transistors (TFTs) is a type of field-effect transistor which is made by depositing thin films of active semiconductor layer, dielectric layer and metal contacts on thin substrate. Currently, amorphous Si-based TFTs are the mainstream TFTs, but their performance and application is limited by the low carrier mobility of amorphous silicon, flexibility and transparency. Organic TFTs have been widely studied as a potential candidate for flexible and transparent electronics. However, organic TFTs cannot rival the performance of Si-based TFTs because of the low carrier mobility of the organic semiconductors. Due to the high carrier mobility and high current density of CNTs, thin

films made of SWCNT networks are semiconducting materials used for channel region of TFTs. Moreover, thin films of CNT networks can also be flexible and transparent, and the ease of fabrication with low-cost, low-temperature processing techniques makes CNTs attractive for flexible, transparent display applications. Figure 1.3 (a) shows the schematic diagram of a TFT using random CNT network as channel material, while Figure 1.3 (b) shows the photograph of a small circuit made by the SWNT transistors on a thin sheet of plastic. The CN-TFTs have been demonstrated to have a mobility as high as 50 ~ 180 $cm^2V^{-1}s^{-1}$, on/off ratios up to 10^5 ~ 10^7 and high switching speed [10, 11].

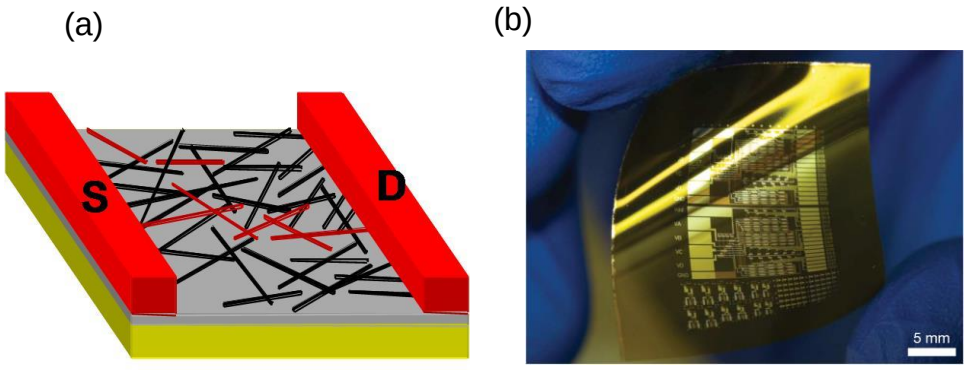

Figure 1.3 (a) Schematic of a carbon-nanotube-network thin film transistor; (b) Photograph of SWNT transistors and circuits on a thin sheet of plastic [12].

1.2.2 Carbon Nanotube Interconnects

With the continued miniaturization and increasing number of transistors in an integrated circuit, the current density has posed strict requirement for the design of interconnects. Electromigration is a current-assisted diffusion process which strictly limits the current carrying capacity of a wire [13]. This current limit for noble metals is approximately 10 nA/nm^2, a severe restriction for nanometer-sized wires [14]. Due to electromigration, a critical issue with interconnects in current Si-based circuits is the

breakdown of copper wires under high current density. Metallic CNTs have attracted extensive attention because of their outstanding current carrying ability. Ballistic transport of electrons has been observed and theoretically proved, which leads to extremely high electrical conductance. Due to their low resistance and strong mechanical properties, metallic CNTs, especially the MWNTs, are promising candidates of interconnects in high performance electronics. Figure 1.4 shows a schematic diagram of interconnects made of bundles of SWNTs and single MWNT. Wei et al. [15], demonstrated that MWNTs carry current densities approaching 10^9 Acm^{-2}. Kreupl et al. and Ngo et al. has demonstrated that bundles of CNTs can be integrated with silicon technology as vertical vias with current carrying capacity what is an order of magnitude larger than the conventional copper vias [16, 17].

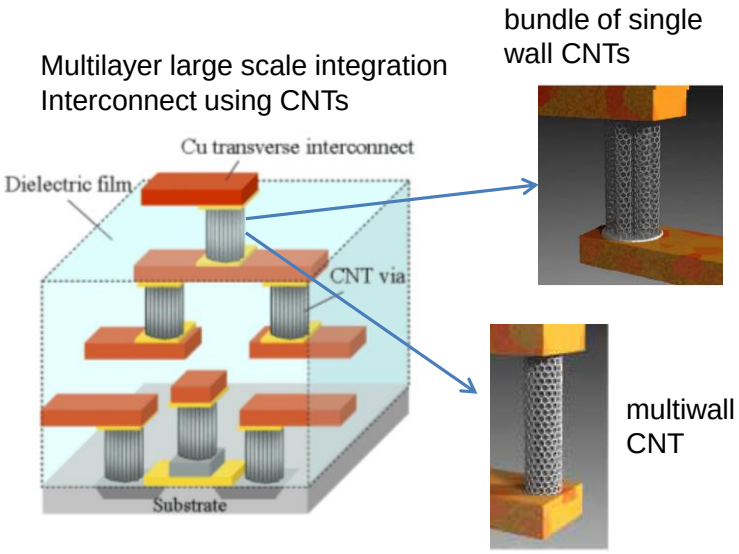

Figure 1.4 Schematic of the CNT interconnects and their application in large scale integration (Courtesy of Kawarada Laboratory and Infineon Technologies)

1.2.3 Graphene Field Effect Transistors (GFETs)

Field effect transistors (FETs) are the mainstream transistors for applications such as digital logic devices and radiofrequency (RF) devices. Nowadays, size scaling is the major approach to improve the performance of logic circuits which requires the number of transistors per chip to be doubled every 18 months. As the scaling of silicon-based FET is approaching its limit, novel material and structures are needed for further performance improvement. The development of new materials for RF devices is a more active area because of the growing need of high frequency operation and the less complexity of RF circuits.

Graphene shares many of the outstanding properties of CNTs including the high intrinsic carrier mobility, high mechanical strength and high thermal conductivity. By increasing the channel width, the current through graphene channels can also be easily scaled up. Besides, the 2D nature of graphene makes it suitable for integration with integrated circuit fabrication technologies. These advantages make graphene particularly promising to be used as the advanced materials in high-frequency transistors. Figure 1.5 shows the schematic diagram of a top-gated graphene field effect transistor (GFET) which consists of a gate/dielectric-barrier/channel/substrate layers, and source and drain electrodes. Preliminary study has demonstrated that graphene transistor can operate at gigahertz frequency as high as 26 GHz with a gate length of 150 nm [18]. Methods have been developed to fabricate GNR with width below 10 nm and with smooth edges [19]. The transistors using sub-10-nm GNRs show on-off ratios of about 10^6 to 10^7 at room temperature [19-21].

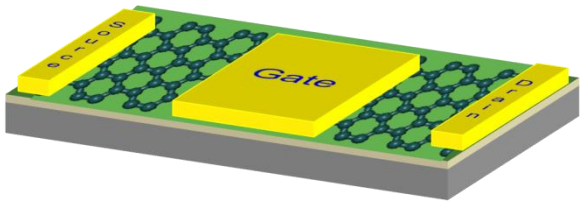

Figure 1.5 Schematic of a graphene nanoribbon field effect transistor

1.2.4 Graphene Electrodes

Because of its high transparency from ultraviolet to near-infrared region and the high electrical conductivity, graphene has been widely studied as transparent electrode materials for applications in photovoltaic devices and electroluminescent devices such as light-emitting diodes (LEDs) and solar cells [20, 22], as shown in Figure 1.6. Jo et al. [23] has demonstrated the use of patterned MLG as transparent conducting electrodes with transparency above 85% in the large-scale batch fabrication of GaN LEDs, as shown in Figure 1.6(a). The performance in terms of light output was comparable to that of conventional GaN LEDs with the expensive indium tin oxide electrodes. In high power LED devices, high operating temperature can degrade the performance. So the high thermal conductivity of graphene is another important advantage for application as electrodes in high power devices. For example, in high power LED devices, much of the localized heat can be dissipated through graphene-based transparent conductive electrode, [24] which can help to improve the heat removal and lower the operating temperature of high power LEDs.

Besides, graphene-based electrodes can also find important application in supercapacitors because of the high intrinsic surface capacitance and specific surface area of SLG. With graphene-based electrodes, the supercapacitors can reach a specific energy

density of 85.6 Wh/kg at room temperature and at a current density of 1 A/g, which are comparable to that of the Ni metal hydride battery [25].

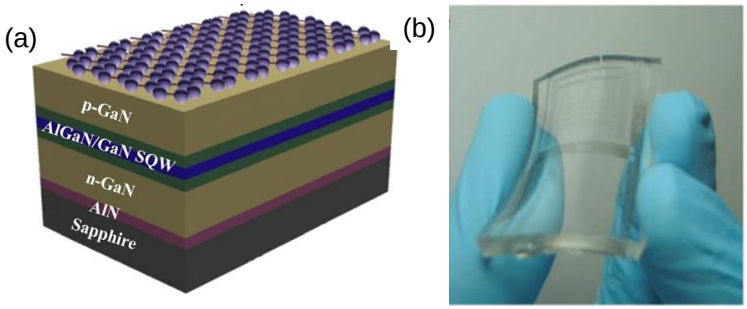

Figure 1.6 (a) GaN LED device using graphene in its electrode; (b) Photograph of transparent and flexible graphene electrode

1.3 Atomistic Models of Thermal Transport

Lattice dynamics (LD), molecular dynamics (MD), Boltzmann transport equation (BTE), and atomistic Green's function (AGF) based methods are popular approaches to study the thermal transport at nano-scale. MD simulation and AGF methods are efficient in handling boundary and interface scattering at complicated interface structures, *e.g.*, CNT and graphene interfaces in this work. In the absence of empirical potential models, density functional theory (DFT) calculations can be used to determine the equilibrium atomic positions and interatomic force constants. In this section, LD, MD, AGF, BTE and DFT methods will be briefly discussed in the context of simulation of thermal transport.

1.3.1 Phonons and Lattice Dynamics

In harmonic approximation, phonons are described as independent harmonic oscillators with normal mode frequency and polarization. For example, six phonon modes can be defined for a primitive unit cell in SLG: three acoustic modes of longitudinal

acoustic (LA), transverse acoustic (TA), out-of-plane acoustic (ZA), and their optical counterparts of LO, TO, and ZO. Figure 1.7 shows the vibrational directions of the two atoms in a unit cell for the six phonon modes.

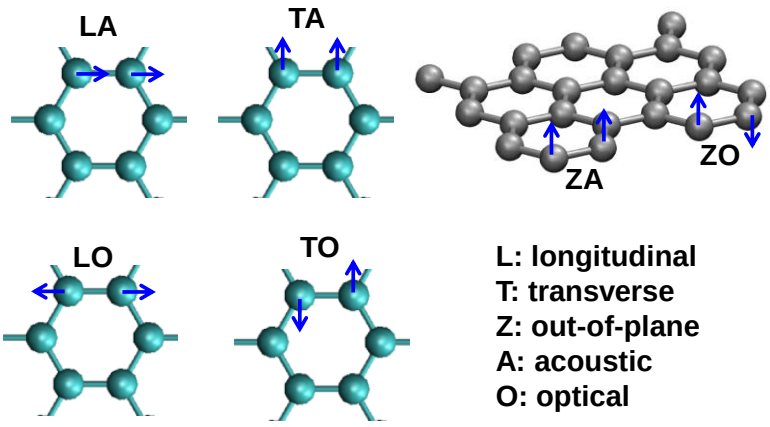

Figure 1.7 Illustration of atom vibration associated with the six phonon modes in single layer graphene

The normal mode frequency and polarization of the phonon modes can be determined by harmonic lattice dynamics. In the dynamical equations, Taylor series expansion of the system potential energy about the equilibrium atomic positions is truncated after second-order term. The equation of motion of the *j*th atom in *l*th unit cell is

$$m_j \ddot{u}_{jl} = \sum_{j'} \sum_{k'} \Phi\left(jl, j'l'\right) \cdot u_{jl} \tag{1.1}$$

where u is the displacement of atom $\left(j,l\right)$ with respective to its equilibrium position.

$\Phi\left(jl, j'l'\right)$ is the second-order force constant matrix.

The normal mode frequency $\omega(q,v)$ of phonon mode v at wave vector q can be obtained by diagonalization of the dynamical matrix $D_{jj'}^{\alpha\beta}(q)$ between atom j and j' in a selected unit cell [26].

$$D_{jj'}^{\alpha\beta}(q) = \frac{1}{\sqrt{m_j m_{j'}}} \sum_{l'} \Phi_{jj'}^{\alpha\beta}(0,l') \exp\left(iq \cdot \left[r_{j'l'} - r_{j0}\right]\right) \tag{1.2}$$

1.3.2 Molecular Dynamics Simulations

The classical MD simulation is based on the Newton's laws of motion.[26]

$$\frac{d\vec{r}_i}{dt} = \frac{\vec{p}_i}{m_i} \tag{1.3}$$

$$\frac{d\vec{p}_i}{dt} = \vec{F}_i \tag{1.4}$$

where m_i, $\vec{r}_i$, and $\vec{p}_i$ are mass, position, and momentum of particle i. The force acting on particle i is determined by the potential models

$$\vec{F}_i = -\nabla V(\vec{r}) \tag{1.5}$$

Verlet algorithm [27] is usually used to integrate equations of motion for positions and momenta of each particle at each time step. The thermodynamic parameters and transport properties can be expressed in terms of positions and momenta of particles in the system.

In MD simulations, empirical potential models are generally used to describe the interactions between atoms/particles. So the accuracy of MD simulation highly depends on the potential model. In CNTs and graphene, carbon atoms are covalently bonded with sp^2 hybridization. Several potential models have been developed for carbon materials.

The reactive empirical bond-order (REBO) model, Tersoff potential model, and polymer consistent force field (PCFF) force field model are widely employed for CNTs, graphene, and their interaction with hydrocarbons/polymers. Based on the MD simulations, thermal conductivity can be calculated using several methods including: 1) non-equilibrium molecular dynamics (NEMD) simulation by applying temperature gradient or heat flux; 2) equilibrium MD simulation based on Green-Kubo formalism; 3) phonon lifetime prediction using spectral energy density.

1.3.3 Green's Function Method

The Green's function method is a mathematical tool that solves non-homogeneous differential equations [28]. For a linear differential operator $\hat{L} = \hat{L}(x)$, a one-dimensional differential equation is

$$\hat{L}u(x) = f(x) \tag{1.6}$$

The Green's function $G(x,s)$ can be defined as the system's impulse response

$$\hat{L}G(x,s) = \delta(x-s) \tag{1.7}$$

Multiply the left hand side of Eq. (1.7) by $f(s)$, and then perform an integration, one can obtain

$$\int \hat{L}G(x,s)f(s)ds = \int \delta(x-s)\, f(s)ds = f(x) \tag{1.8}$$

The right hand side is given by Eq. (1.6). Therefore,

$$\hat{L}u(x) = \int \hat{L}G(x,s)f(s)ds = \hat{L}\left(\int G(x,s)f(s)ds\right) \tag{1.9}$$

Finally, the solution to linear differential equation (1.6) can be obtained

$$u(x)=\int G(x,s)f(s)ds \tag{1.10}$$

Therefore, one can solve the linear differential equation through the knowledge of Green's function that is the impulse response of the linear time-invariant system.

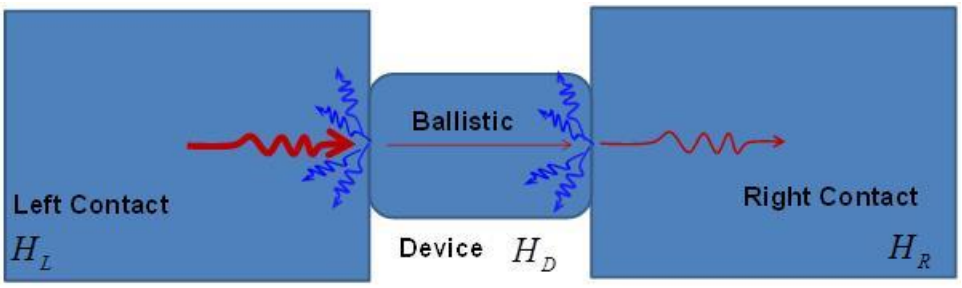

Figure 1.8 Schematic of a typical phonon transport problem considered in the AGF formulation. Only the phonon scattering at interfaces is considered, and the phonon transport in device region and contacts is ballistic. H_L, H_R and H_D denote the harmonic matrices of left contact, right contact and device, respectively.

In the AGF model as shown in Figure 1.8, the system consists of a device connected with: left semi-infinite contact and right semi-infinite contact. Considering phonons are waves that propagate through the system, the dynamics of phonons, to the second order, can be described as [29]

$$\left(\omega^2 I-H\right)\tilde{u}=0 \tag{1.11}$$

where ω, H, and $\tilde{u}$ are the angular frequency, harmonic matrix, and displacement, respectively. Equation (1.11) is actually the expression of dynamical equation (1.1) in frequency domain. The Green's function can be solved as

$$G(\omega)=\left[\left(\omega^2+i0^+\right)I-H\right]^{-1} \tag{1.12}$$

where 0^+ is a small positive infinitesimal factor that introduces damping in the open system. In time domain, the Green's function $G(t)$ satisfies the impulse response equation:

$$\left(-\frac{\partial^2}{\partial t^2} - H + i0^+\right) G(t) = \delta(t) I \tag{1.13}$$

Therefore, the Green's function in the atomistic model can be interpreted as the impulse response of the lattice dynamics equation (1.1). With the knowledge of Green's function, one can obtain the information of atom's displacements $\tilde{u}$ in the device region which consists of phonon vibrations including the effect of coupling with contacts [29].

1.3.4 Boltzmann Transport Equation

The transport characteristics of phonons can be described by BTE considering the phonon scattering events such as three phonon scattering, impurity scattering, defect scattering and boundary scattering. The single mode relaxation time (SMRT) approximation is widely employed where the relaxation time is used to include the scattering effects for each phonon mode. Under SMRT approximation, for the a phonon mode (q,v), the BTE is shown in Eq. (1.14) [30, 31].

$$\frac{\partial e_{ph}}{\partial t} + \nabla \cdot \left(v_{ph} \hat{s} e_{ph}\right) - \frac{e_{ph}^{eq} - e_{ph}}{\tau_{ph}} = 0 \tag{1.14}$$

where e_{ph}, v_{ph}, and τ_{ph} are the energy density, group velocity, and lifetime of a phonon mode (q,v). The phonon lifetime can be determined using MD simulations, empirical correlations, or different level description of three phonon scattering using Fermi Golden

rule. By applying proper boundary condition to create the temperature gradient, the heat flux and thermal conductivity can be obtained.

1.3.5 Density Functional Theory Calculation

Computational quantum mechanics is a fundamental method to predict electronic structure and material properties. The electronic structure of material at ground state can be obtained by minimizing the energy eigenvalues of the time-independent Schrödinger equation [32]

$$\hat{H}\Psi\left(r_1, r_2, ..., r_N\right) = E\Psi\left(r_1, r_2, ..., r_N\right) \tag{1.15}$$

Accurate solution of many-body wave function is an extremely time consuming and generally untenable task. Based on Hohenberg and Kohn [33], DFT has been developed as an alternative approach to solve Schrödinger equation using ground state electron density. To solve the many-body problem, Kohn and Sham approximated the Hamiltonian of an interacting many-body system with that of a non-interacting system and incorporated the interactions into an exchange-correlation functional of electron density. The Kohn-Sham expression [32] for the energy functional is

$$E\left[\rho\right] = T_s\left[\rho\right] + V_{ext}\left[\rho\right] + V_H\left[\rho\right] + E_{xc}\left[\rho\right] \tag{1.16}$$

where T_s, V_{ex}, and V_H are functionals of the non-interacting system for kinetic energy, interaction with external potential, and Hartree energy (classical Coulomb interaction), respectively. The exchange-correlation functional [32] is given by

$$E_{xc}\left[\rho\right] = \left(T\left[\rho\right] - T_s\left[\rho\right]\right) + \left(V_{ee}\left[\rho\right] - V_H\left[\rho\right]\right) \tag{1.17}$$

It represents the correction for approximating kinetic energy and electron interaction with a non-interacting kinetic energy and classical electron-electron interaction. Theoretically,

an exact solution can be obtained if the exact form of exchange-correlation term exists. However, approximation must be made for E_{xc} which is currently an active research area to improve DFT.

Local density approximation (LDA) and generalized gradient approximation (GGA) are the most popular treatment of E_{xc}. In LDA, E_{xc} is a functional of local electron density which is the same as that of uniform electron gas. Thus, LDA functionals are expected to yield good results for homogeneous systems such as periodic crystals. LDA is known to overestimate the cohesive energy of solid and underestimate the band gaps of insulators. However, LDA can give better prediction for binding energy arising from van der Waals (vdW) interaction which is actually absent in LDA functionals. GGA functionals depend on the local electron density as well as its gradient. GGA improves significantly on LDA's description of the band gap and cohesive energy. But it generally underestimates the binding energy with vdW interactions.

1.4 Motivation

In the application of electronic devices using CNT and graphene, *e.g.* CNT-TFTs, CNT interconnects, GFETs and graphene electrodes, thermal management can be a critical issue for the high performance and reliabile operation. This can be attributed to the high power density as well as the properties of CNT/graphene structures in those devices. In this section, the important factors that motivate the current research work is discussed.

1.4.1 Heat Dissipation in CNT Networks

In CNT-TFTs, films of CNT networks are generally deposited on low thermal conductivity substrates such as glass or polymer, and therefore the excessive self-heating in CNT-TFTs is likely to degrade the carrier mobility and may lead to breakdown of CNTs [34]. In a transparent or flexible display, the surfaces are usually cooled only through natural convection which can make self-heating critical especially for CN-TFTs operating in high frequency range (~ MHz) [35, 36] and high bias operation [37-39]. As a result, self-heating during operation may lead to early breakdown of CN-TFTs and therefore presents a serious challenge to the device reliability particularly under high frequency. The interfacial thermal conductance at CNT-substrate interfaces [40-45] and CNT-CNT junctions [46-50] are very low which can exacerbate the self-heating effects and can significantly degrade the TFT performance [50-56]. Previous studies are mainly focused on the electrical breakdown of single CNT [40, 45, 57], breakdown of CNT-networks [57, 58], and the CNT/substrate [41-43] and CNT/CNT contact resistance [46, 59-61]. However, the heat dissipation mechanism at CNT junctions and junction interaction with SiO_2 substrate are not well understood.

1.4.2 Inter-shell Thermal Transport in Multi-wall Carbon Nanotubes (MWNTs)

MWNTs, which are generally metallic, are expected to outperform copper, in terms of current density and power dissipation as interconnects for future gigascale integration [62, 63]. Under a high current density, self-heating in MWNTs may become critical, and the effective heat removal from MWNTs is required. Previous studies have investigated high energy transport in MWNTs as a candidate to replacemetal wire

interconnects [14, 17, 64, 65]. In contrast to metal wires, MWNTs do not fail via electromigration, but fail in a series of sharp steps associated with the destruction of individual nanotube shells [14]. These steps are regularly spaced in current regardless of the applied voltages due to the high bias current saturation in each shell, which suggested a shell-by-shell failure in MWNTs. Therefore, it is important to study the thermal coupling and energy exchange between shells in MWNTs in order to better understand the high power failure of MWNT interconnects.

1.4.3 Thermal Conductivity Reduction of Supported Graphene

The thermal conductivity of suspended single layer graphene (SLG) was measured to be as high as 3000 ~ 5300 W/mK [66-68]. Recent measurements show high thermal conductivity of suspended single layer graphene (SLG) grown by chemical vapor deposition (CVD) technique, *e.g.*, 2500 W/mK at 350K and 1400 W/mK at about 500K [69]. However, graphene-substrate interactions can significantly reduce the thermal conductivity of the supported SLG [70] and the supported few-layer graphene [71]. The thermal conductivity of SLG supported on SiO_2 was measured as 600 W/mK at room temperature, which is much lower than the suspended SLG but still considerably higher than many metals (~Cu) typically used in the electronic devices [70]. As graphene will be either supported or embedded in most of the applications such as field effect transistors or interconnects, a good understanding of the graphene thermal interaction with different materials such as dielectrics (~SiO_2) and metals (Cu, Au, and Pd) is crucial.

1.4.4 Heat Removal through Graphene/Metal Contacts

In the applications such as GFETs, graphene interconnects and graphene electrodes, the size scaling, high frequency, and high field operation can lead to very high current density as well as unusual Joule heating. The heat removal from SLG or MLG contacts in graphene devices becomes critical. Thermal transport across graphene-metal interfaces becomes particularly important when their contact resistance becomes an obstacle in the effective heat removal from the devices, especially in short channel field effect transistors (FETs) and graphene-Cu hybrid-interconnects [72, 73]. For example, the graphene/metal contacts can be the major heat transfer pathway when the channel length is smaller than certain value, *e.g.* $3L_H$ where L_H is the thermal healing length [74].

Thermal properties at MLG/metal interface can be very different from SLG/metal interface because of the different interface interactions. The interaction between graphene layers in MLG is described by the weak van der Waals forces. However, according to different bonding type, graphene/metal interfaces can be classified into two types: physisorption interface (*e.g.*, Au, Cu, Ag, Pt, and Al) formed by charge transfer and chemisorption interface (*e.g.*, Ti, Co, Ni, and Pd) formed by orbital hybridization [75-77]. The interfacial chemistry can significantly affect the strength of interaction as well as TBC at graphene/metal contacts [78]. Recent studies have shown TBC across graphene/metal interfaces depends on multiple factors such as interfacial structure [79, 80], interfacial bonding [81, 82], contaminants and defects, *etc*. [79, 83-85]. However, many aspects of the phonon coupling mechanism at graphene/metal interfaces, such as

the impact of interfacial bonding and number of graphene layers on TBC, have not been well understood by experimental measurements.

1.5 Objectives and Scope of Thesis

The proposed research is aimed to investigate the phonon interactions and heat dissipation at the interfaces involving CNTs and graphene, and to predict the phonon transmission and thermal boundary conductance (TBC) at graphene/metal interfaces. The objectives will be achieved using atomistic modeling techniques including MD simulations, AGF calculations, and DFT calculations.

The outline of the remainder of the thesis is as follows.

Chapter 2 reviews the literature regarding the thermal transport in CNT and graphene nanostructures, *e.g.* thermal conductivity measurement, thermal boundary conductance measurement, atomistic modeling of phonon transport and first principle study of electron-phonon interactions. It also summarizes the important contributions of the present work. Chapter 3 presents the atomistic models to study the thermal transport in CNT/graphene nanostructures.

The *first* part of the thesis deals with the various interfaces of CNTs such as CNT-CNT junctions, CNT-substrate interfaces, and inter-shell interfaces in DWNTs. Chapter 4 discusses the heat dissipation at CNT junctions on SiO_2 substrate based on the results of MD simulations and phonon spectrum analysis. Chapter 5 investigates the energy exchange and coupling of the vibration modes between shells of DWNTs using MD simulations in the framework of travelling wave packets.

The *second* part of the thesis aims at analyzing the thermal transport and phonon scattering at graphene and metal interfaces using MD and AGF method. Chapter 6 presents analysis on the effects of Cu substrate on SLG thermal conductivity based on the MD simulation and relaxation time calculation. Chapter 7 presents the results and

analysis on TBC across SLG/Cu interfaces using AGF calculations. Chapter 8 contains the AGF calculation and discussion of the phonon transmission and TBC across MLG sandwiched between different metal contacts.

Finally, Chapter 9 summaries the current work and presents suggestions for the future work.

CHAPTER 2

BACKGROUND

The phonons are primary heat carriers in dielectrics and semiconductors, and electrons in metals. In recent decades, the development of fabrication, characterization and modeling techniques has remarkably advanced our understanding on thermal transport mechanism in many novel nano-materials. In low-dimensional carbon nano-materials such as CNTs and graphene, phonons have been identified as the primary heat carriers. The recent experimental and numerical studies on CNTs and graphene are focused on elucidating phonon transport mechanism in order to better understand the heat dissipation in their devices. The electron-phonon coupling is another important focus of many studies where the electrons gain high energy from external sources, *e.g.*, high electric field in transistors and laser-irradiation process in applications such as micro-Raman spectroscopy measurements. In this Chapter, a literature survey is presented to summarize the recent experimental and numerical studies on the phonon-mediated thermal transport in CNTs and graphene, followed by a summary of the contribution of current thesis work.

2.1 Experimental Study of Thermal Transport in CNT and Graphene

In recent decades, the thermal measurement techniques have been greatly advanced for the study of thermal transport at micro/nanoscale. Many techniques, *e.g.* 3ω method, micro-Raman spectroscopy, pump-probe techniques and nanofabricated thermometer devices, have been successfully used for CNT and graphene nanomaterials,

which has remarkably improved our understanding of their thermal properties and facilitated their applications.

2.1.1 Thermal Conductivity Measurement of CNTs

Although the synthesis of CNTs by Iijima in 1991 sparked extensive interests in the study of their electrical and mechanical properties, the investigations of thermal properties received less attention until their ultrahigh thermal conductivity was measured by Kim, *et al.* in 2001 [86]. They used a microfabricated suspended device to measure thermal conductivity of individual MWNTs by applying temperature difference between two suspended islands; the measured thermal conductivity was higher than 3000 W/mK at room temperature. As shown in Figure 2.1, they also observed temperature dependence of thermal conductivity which showed a peak value at 320 K. The observed thermal conductivity peak is due to the onset of Umklapp scattering. Below room temperature, the phonon-phonon Umklapp scattering is minimal, and the phonon can transport ballistically with long mean free path. The thermal conductivity of bundles of MWNTs is much smaller due to the phonon scattering between tubes.

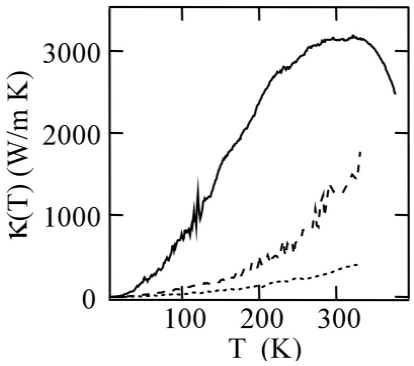

Figure 2.1 Thermal conductivity of multiwall carbon nanotubes (MWNTs) as a function of temperature. Solid line represents an individual MWNT with a diameter of 14 nm.

Broken and dotted lines represent small (d = 80 nm) and large bundles (d = 200 nm) of MWNTs, respectively. [86]

The 3-ω method is another viable technique for thermal measurements of CNTs. Choi et al., [87] microfabricated a device to measure thermal properties of individual MWNTs suspended between metal electrodes. They observed diffusive energy transport and obtained thermal conductivity between 650 and 830 W/mK in individual MWNTs at room temperature. Yu et al. [88] and Pop et al. [89] measured the thermal conductivity of suspended individual SWNTs, and obtained values of nearly 3500 W/mK at room temperature without showing signatures of phonon-phonon Umklapp scattering for temperatures between 110 K and 300 K. However, this remarkably high thermal conductivity of individual CNTs, dominated by ballistic phonon transport, was not seen in the CNT bundles [90-93], which was possibly due to the extrinsic phonon scattering such as tube-tube interactions, defect scattering and impurity scattering.

2.1.2 Thermal Conductivity Measurement of Graphene

Experimental study of graphene thermal conductivity are mainly based on measurements using Raman technique [94] and nanofabricated resistance thermometer device [70]. The ultrahigh thermal conductivity of suspended SLG was first experimentally revealed by Balandin's research group in 2008 [66, 67]. They performed micro-Raman spectroscopy measurements on large-area suspended graphene layers exfoliated from high-quality HOPG. The thermal conductivity of SLG was extracted for graphene from the dependence of the Raman G peak frequency on the excitation laser

power. They found thermal conductivity of SLG near room temperature exceeding ~3,000 W mK^{-1}, and estimated the phonon mean-free path to be ~775 nm [67, 95]. Another group repeated the Raman spectroscopy measurements, but obtained much smaller thermal conductivity of suspended SLG, ~630 W/mK between 500 K and 660 K. The difference can be attributed to different assumptions regarding the efficiency of the graphene's optical absorbance and the temperature dependence of thermal conductivity. Other Raman spectroscopy measurements generally suggested thermal conductivity of suspended SLG in the range from ~1500 to ~5000 W/mK [69, 96, 97] around room temperature.

The measurements by micro-Raman spectroscopy are normally performed under ambient conditions. The accuracy in estimating thermal conductivity is limited by the assumptions about the laser absorbance as well as unknown convective heat losses. Besides, the graphene needs to be suspended or partially suspended because the background reflection from substrate can further increase the uncertainty in the estimation of laser power absorbance. In spite of the large uncertainties, Cai et al. [69] performed micro-Raman spectroscopy measurements on both suspended and supported graphene, and obtained thermal conductivity of supported graphene around 370 W/mK with a large uncertainty of +650/-320 W/mK.

Microresistance thermometry has been developed with high temperature sensitivity (~0.05 K) for a wide range of nanomaterials such as individual CNTs and nanowires. This technique offers direct measurements of the heating power and accurate measurement temperature in vacuum. Seol et al., employed microresistance thermometry to study the effects of substrate interaction on the phonon transport in SLG. They

reported a thermal conductivity of ~600 W/mK near room temperature for SLG supported on SiO_2 substrate, a substantial reduction compared with the thermal conductivity around 3000~5000 W/mK for suspended SLG, as shown in Figure 2.2.

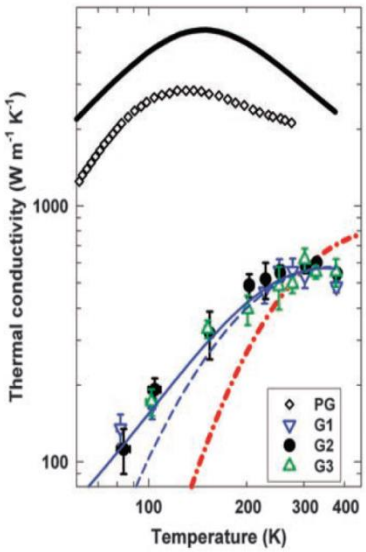

Figure 2.2 Measured thermal conductivity of SLG samples G1, G2, and G3 together with the highest reported values of pyrolytic graphite (PG); The results from BTE based model of suspended SLG (black solid line) and supported SLG (blue dashed lines), and the BTE calculation results with the relaxation time approximation (red dashed-dotted line) for supported SLG. [70]

Following Seol's work, Wang et al., developed a thermal-bridge device to measure the thermal conductivity of both suspended and supported few layer graphene (FLG) where the localized electron beam heating technique was employed. Similar substrate effects were observed for thermal conductivity of FLG. The reduction in thermal conductivity of SLG and FLG can be attributed to graphene-substrate coupling

and phonon leaking across the interface, which will be discussed in detail in the review of related numerical studies.

2.1.3 Thermal Boundary Conductance Measurement at CNT Interfaces

Before the ultrahigh thermal conductivity of individual CNTs was reported, several experiments have been performed to measure the thermal conductivity of CNT mat and bundles. The measured values around room temperature ranged from 2.3 ~ 35 W/mK for CNT mat [92, 98] and 25~200 W/mK for CNT bundles [90-93]. In addition to the effects of defect, impurity, and CNT-CNT interaction, the low thermal boundary conductance (TBC) at various interfaces is an important factor that leads to the low thermal conductivity. Those interfaces include CNT-CNT junction, inter-shell interface in MWNTs, CNT-substrate interfaces, and interfaces between CNT ends and their metal contacts. Table 2.1 lists the reported TBC at various CNT interfaces.

Table 2.1 Thermal Boundary Conductance (TBC) at CNT Interfaces. TBC at interface between CNT-side and SiO_2 is normalized to CNT length. The extraordinary TBC at CNT cross contact is due to the definition of small contact area between CNTs.

Contact type	TBC	Methodology	Reference
CNT-side/SiO2	0.14~0.2 W/mK	Joule heating meas.	[44, 99]
CNT-end/metal (Al, Ti, Pd, Pt, Ni)	0.1~0.26 MW/m^2K	thermo-reflectance thermometry	[100]
CNT-end/Cu	0.05 MW/m^2K	calorimeter with infrared temperature meas.	[101]
CNT-end/Ag	0.05~0.14 MW/m^2K	photoacoustic technique	[102]
CNT-end/Si	0.02~0.03 MW/m^2K	thermo-reflectance thermometry	[100]
CNT-end contact	~0.5 MW/m^2K	photoacoustic technique	[103]
CNT cross contact	~1000 MW/m^2K	micro-device	[47]

In a study of breakdown of a single CNT supported on SiO_2 substrate [14, 44, 58, 99], it has been demonstrated that interfacial resistance between CNTs and SiO_2 substrate limits the heat dissipation capability. The experiments on breakdown of CNT devices reveal that low TBC poses a fundamental challenge for the heat removal from CNT networks or CNT arrays. Detailed numerical studies suggested that the temperature profiles and breakdown behavior of the CNT network is more sensitive to TBC at CNT-substrate interface compared to that of the CNT-CNT interface. When aligned CNT arrays are used as thermal interface material, the thermal contact resistance between CNT end and substrate/metal will become the dominating thermal resistance. Many experimental studies [100, 104] [101-103] have been focused on improving the contact at CNT ends in order to reduce the effective thermal resistance of the thermal interface material.

However, the heat transfer at the CNT-CNT interfaces is even worse due to weak interactions and small contact area. This can result in local hot spot and breakdown of individual CNT. Experimental results in Ref. [47] showed that the thermal contact resistance between CNTs is on the order of 10^{-9} m^2K/W after normalization with respect to the contact area. They also found that the contact thermal conductance can increase by approximately two orders of magnitude (from 10^{-8} to 10^{-6} W/K) as the contact area increases from a cross contact to an aligned contact. In some extreme cases when the CNTs are packed as 3D random networks [50], the bulk thermal conductivity can be as low as 0.13 ~ 0.20 W/mK which is even smaller than that of amorphous polymers typically used for the thermal insulation.

2.1.4 Thermal Boundary Conductance Measurement at Graphene Interfaces

The experimental measurements suggested that the thermal conductance at interfaces of the graphene with other materials vary in a large range [69, 84, 105-108]. Chen et al. [105] performed differential 3ω measurements for the TBC between SiO_2 and graphene with different thickness. The measured TBC at room temperature ranged from 80 to 180 MW/m^{2}K without showing dependence on thickness of graphene layers. Mak et al. [109] employed an ultrafast optical pump pulse technique to measure TBC at interfaces between exfoliated SLG/MLG and SiO_2 substrate, and obtained an average value of 50 MW/m^{2}K at room temperature. Their measurements also suggested no systematic dependence on the thickness of the graphene layers.

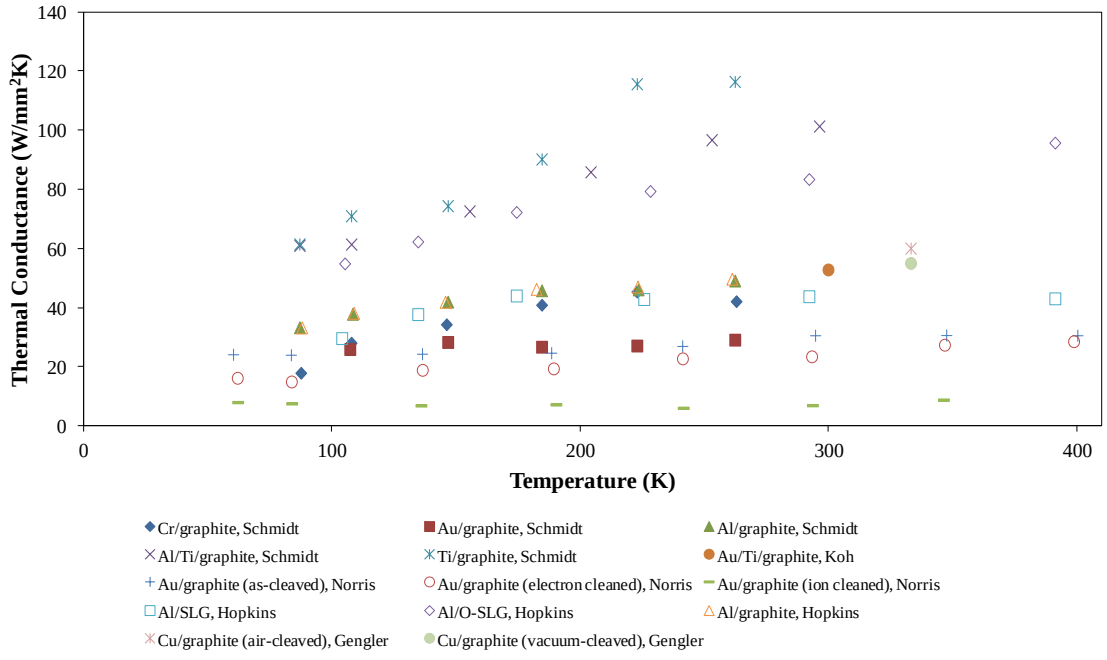

Figure 2.3 Thermal boundary conductance at metal-graphite or metal-graphene interfaces. Experimental data is taken from Refs. [69, 84, 106-108].

Several studies [84, 106, 110-112] have been recently performed to measure TBC at graphene (graphite) interfaces with different metals. The measurement results are summarized in Figure 2.3. The interfacial chemistry can significantly affect the strength of interaction as well as TBC at graphene/metal contacts [78]. According to different bonding type, graphene/metal interfaces can be classified into two types: physisorption interface (*e.g.*, Au, Cu, Ag, Pt, and Al) formed by charge transfer and chemisorption interface (*e.g.*, Ti, Co, Ni, and Pd) formed by orbital hybridization [75-77]. The TBC at physisorption HOPG/metal interfaces (*e.g.*, Au, Cu, and Al) has been reported in the range of 7 to 60 MW/m^2K around room temperature [113, 114] [115], while the TBC at chemisorption interfaces (*e.g.*, HOPG/Ti) has been reported as high as 120 MW/m^2K [107, 108].

2.2 Atomistic Modeling of Thermal Transport in CNT and Graphene

While the thermal conductivity of CNT and graphene and TBC at their interfaces can be experimentally measured under some conditions, atomistic models can provide crucial insights into phonon transport mechanism and can predict the thermal conductivity and TBC if the problem involves complicated structures, novel material design, and extreme conditions. Regarding to the atomistic simulations of thermal transport, a large number of papers have been published in past decades. Instead of a comprehensive review on the simulation results of various materials and nanostructures, this section focuses on the mechanism of phonon interaction that features thermal transport in CNTs/graphene as well as their interfaces.

2.2.1 Size Effects on Thermal Conductivity Prediction using MD Simulations

Due to the 1D/2D nature of their structure, pristine CNTs and graphene are ideal candidates for the study of phonon transport physics, especially the ballistic transport phenomena. So phonons in long CNTs and large graphene sheet will travel with long MFP up to few microns when the impurity and defect scattering is absent [116]. When the size is smaller than the phonon MFP, boundary scattering can limit their thermal conductivity. Therefore, strong size effects are observed in most of the studies on prediction of thermal conductivity for CNTs and graphene using atomistic models.

Moreover, one main concern of using MD simulations to calculate the thermal conductivity is the size effects. Due to periodic boundary conditions, phonons in a small system will get scattered more frequently which leads to a reduction in the phonon MFP as well as the underestimation of thermal conductivity. The capability of MD simulations is limited by the number of atoms and the computational complexity of potential models. For MD simulations of thermal transport for CNTs and graphene, 10^7 time steps are required to get reasonable sampling, and the number of atoms is generally limited to order of 10^5 which corresponds to dimension of submicrons for CNTs and graphene.

Length Dependence of CNT Thermal Conductivity in MD Simulations

Very short CNTs (< 40 nm) were simulated in the early studies using MD simulations [117-120] which yield inconsistent or unrealistic values of thermal conductivity. In those MD simulations, Tersoff-Brenner bond order potential [121, 122] was used to describe C-C interactions. Later, Maruyama et al. [123-126] performed an extensive MD simulations using Brenner potential [127], and the thermal conductivity is

predicted for a range of CNT length up to 1.6 μm. They observed a gradual transition from nearly pure ballistic to diffusive-ballistic heat conduction. The thermal conductivity profile shows power law length dependence ($k \propto L^{\alpha}$ where α ranges from 0.11~0.33), which is consistent with the ballistic-diffusive mechanism of the thermal conductivity. They also find the length dependence is particularly strong for CNTs with small diameter. However, the thermal conductivity does not converge even for a tube length of 1.6 μm. Many other studies using MD simulations also found similar length dependence [116, 128, 129] using the same Tersoff/Brenner potential models.

Reactive bond order potential (REBO) [127] is an improved second-generation version of the Tersoff-Brenner potential. Padgett and Brenner [130] used REBO potential in their NEMD simulations and found a thermal conductivity of 160 W/m K for SWNTs at 61.5 nm. Lukes and Zhong [131] reported similar values of thermal conductivity which range from 10 ~ 375 W/mK depending on the length (5 ~ 45 nm). Using REBO potential, McGaughey's group [132] performed MD simulations for SWNTs with length up to 1 micrometer, and obtained converged thermal conductivity at room temperature from 280 W/mK to 500 W/mK, depending on the CNT diameter. Specifically, they found that the required CNT length to obtain fully diffusive phonon transport decreased from 1090 nm for the 0.83-nm-diameter CNT to 510 nm for the 1.36-nm-diameter CNT. In contrast to the overestimation of thermal conductivity in previous studies using Tersoff-Brenner potential models, the REBO potential tends to underestimate the thermal conductivity.

Thermal Conductivity of Graphene Nanoribbon in MD Simulations

Unlike 1D CNTs, the MD simulations of large graphene sheet requires much more computational cost because the number of atoms in a 2D square graphene sheet is order of L^2 where L is the dimension of graphene sheet. McGaughey et al., [132] performed NEMD simulations to calculate thermal conductivity of graphene sheet which has a narrow width of 5 nm. In order to represent infinite graphene sheet, they apply periodic boundary conditions in the width direction. Using the REBO potential, they obtained converged thermal conductivity of 350 W/mK at a length 600 nm. Evans et al. [133] performed equilibrium MD simulations with Tersoff potential for a square graphene sheet up to 15 nm $\times$ 15 nm. Using the Green-Kubo formulism, they find the conductivity can converge after 5 nm within 8000 W/mK to 10000 W/mK at room temperature. Similar with the thermal conductivity prediction of CNT, Tersoff potential tends to overestimate the graphene thermal conductivity. Zhang el al. [134] use the optimized REBO potential in their equilibrium MD simulations with the Green-Kubo method for calculation of graphene thermal conductivity at 300 K. They report a converged value of 2900 W/mK for a graphene size as small as 2.5 nm $\times$ 2.5 nm.

Alternatively, most of MD simulations are focus on the thermal conductivity of GNRs which has smaller dimension as well as number of atoms. In GNRs with different width [133, 135, 136], edge roughness [133, 137], edge-passivation [133, 136], defects [134], and isotope doping [136, 138], phonon scattering can be enhanced, leading to a ballistic-to-diffusive transition of phonon transport as well as a reduction of their thermal conductivity. However, in many of MD simulations, the GNR length is small (< 10 nm), and strong size effects can still exist. Evans et al. [133] find the GNR thermal

conductivity increase from 1000 W/mK to 7000 W/mK with the width varying from 1 to 10 nm. They fixed the length of GNR at 10 nm. Hu et al. find that the calculated thermal conductivity is nearly doubled after doubling the length (5.7 nm) of GNRs (with width unchanged ~1.5 nm), but the calculated thermal conductivity remains nearly the same after doubling the width of GNRs (with the length unchanged).

2.2.1 Size Effects on Thermal Conductivity Prediction using BTE based Models

The BTE model considers the transport of phonons in nanostructures, and computational cost depends on the methodology to consider phonon modes and system dimension. BTE models can be performed for thermal transport in CNTs and graphene with size of micrometers to millimeters. BTE simulations with different level of approximations have been reported for prediction of thermal conductivity of CNTs and graphene. However, without an accurate, full scope description of phonon scattering, the BTE prediction of thermal conductivity in CNTs and graphene will generally diverge as system size increases.

Size Effects of BTE Models for Thermal Transport in CNTs

Early studies using BTE models for prediction of CNT thermal conductivity are based on SMRT approximation. Cao et al. [139] [140] calculated the relaxation rate of zigzag SWNTs by taking into account only the acoustic branches. They find thermal transport in SWNT's is dominated by the phonon boundary scattering at low temperature and by Umklapp scattering process at high temperature. However, they employ a constant relaxation time (50 ps) for boundary scattering without considering the dependence on

temperature and phonon energy. So their study did not include the size effects caused by the boundary scattering. Hepplestone and Srivastava [141] calculate the intrinsic lifetime of phonon modes including the effects of both three-phonon normal and Umklapp processes for SWNTs. They find the total relaxation rates of the longitudinal and twist modes are doubled when the two optical branches are involved in the phonon scattering. However, they only consider four acoustic branches and the two lowest nonzero optical branches. The length is explicitly included in the calculation of scattering rate which will result in divergence as length increases. Gu and Chen [142] performed the BTE calculations with SMRT approximation by including all possible Umklapp scattering processes (the three phonon combing and splitting) based on complete phonon dispersion relations. They find that combining (splitting) Umklapp process is predominant in the low (high) frequency regime; they obtained a thermal conductivity of 474 W/m K for a one-micron-long SWNT at 300 K.

Instead of using SMRT approximation, Mingo and Broido [143] [144] developed BTE models for SWNTs by including a full spectrum of anharmonic three-phonon scattering processes. They demonstrated that Umklapp scattering will be prohibited if only the acoustic phonon branches are considered and scattering of acoustic phonons by optic phonons is required to produce thermal resistance in SWNTs. Besides, Lindsay and Broido [145] optimized Tersoff and Brenner potential models for lattice dynamics and phonon thermal transport in CNTs and graphene. The BTE calculations using the optimized parameter sets can predict thermal conductivity values in SWNTs and graphene that are considerably improved compared to those obtained from the original parameter sets.

Size Effects of BTE Models for Thermal Transport in Graphene

Similar with the BTE study of CNT thermal transport, the BTE study of graphene thermal transport can also fall into two categories: 1) SMRT approximation; 2) iterative solution of linearized BTE with full description of three phonon scattering. With SMRT approximation and full description of phonon dispersions, studies by Balandin's group [95, 146, 147], Askamija et al. [148, 149], and Kong et al. [150] employ the Gruneisen parameter determined from DFT calculations to account for the anharmonicity for three-phonon scattering rates without considering phonon selection rules, which is similar to the Klemens approach [151]. However, their predictions of thermal conductivity tend to diverge if boundary scattering or other scattering event is included.

Lindsay and Broido [152, 153] investigate the thermal transport in graphene based on an exact numerical solution of the linearized BTE which can accurately incorporate the inelastic phonon-phonon scattering. They calculated thermal conductivity for both SLG and MLG with size up to 10 μm. The size effects are more significant for SLG than MLG, but no convergence of thermal conductivity has been observed neither in SLG nor MLG. Following Broido's work, Singh [154-156] compute the thermal conductivity of graphene for a wide range of parameters giving spectral and polarization-resolved information. They find that thermal conductivity of graphene strongly depends on sample dimensions, increasing strongly with size smaller than 1 μm, but saturates for values larger than 10 μm. They reveal that the neglect of normal processes of three phonon scattering is the reason that produces a diverging thermal conductivity with increasing size. In the study of MLG thermal conductivity [71, 156], a significant reduction in the thermal conductivity of the out-of-plane acoustic modes is apparent even with weak

coupling between layers because the interlayer coupling opens many new three-phonon scattering channels.

2.2.2 Contribution of Phonon Modes to Thermal Transport

In thermal transport of CNTs and graphene, phonon modes can play different roles, and their contribution to the thermal conductivity is a fundamental question. Based on the BTE calculations, Mingo and Broido [143] find that low frequency phonons, particularly two flexural modes, disproportionately contribute to the thermal conductivity of SWNTs. If BTE with only three-phonon processes to the first order is used, the thermal conductivity will diverge as length increases. After inclusion of high order processes, the low frequency singularity can be addressed and a finite thermal conductivity can be obtained at large lengths. Donadio and Galli [116] predict the phonon lifetime of different phonon modes in a (10, 0) SWNT based on the equilibrium MD simulations with the normal mode decomposition method [157-159]. They find acoustic and flexure modes with mean free paths of the order of a few microns as major contributors to the high value of SWNT conductivity, which is in good agreement with their estimation using Green-Kubo method. Recently, spectral energy density (SED) method is developed by Thomas and McGaughey [132] to determine by phonon lifetime based on the equilibrium MD simulations. Studies [43, 132] using SED method find that the four acoustic branches are responsible for 44% of the thermal conductivity with the majority of this contribution coming from acoustic modes with small wave vectors.

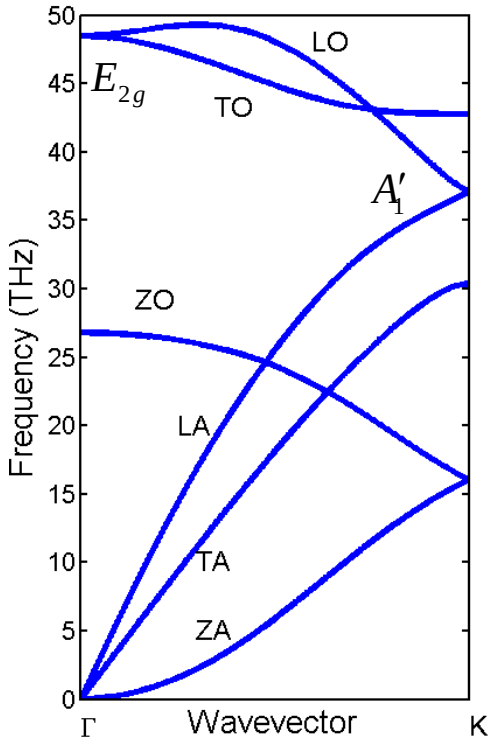

Figure 2.4 Phonon dispersion curves along Γ-K direction of single layer graphene (SLG). Six phonon modes can be defined in SLG: longitudinal acoustic (LA), transverse acoustic (TA), out-of-plane acoustic (ZA), longitudinal optical (LO), transverse optical (TO), and out-of-plane optical (ZO). Also labeled in the figure are E_{2g} mode at Γ point and A_1' mode at K point.

Unlike CNTs, the phonon modes for a primitive unit of graphene can be well defined: three acoustic modes of longitudinal acoustic (LA), transverse acoustic (TA), out-of-plane acoustic (ZA), and their optical counterparts of LO, TO, and ZO, as shown in Figure 2.4. The relative contribution to the thermal conductivity of SLG by LA, TA and ZA phonon modes is still unclear, although it has been studied by different methods. BTE calculations show a significant discrepancy in the role of the out-of-plane acoustic

(ZA) phonons [70, 147, 152, 154, 156, 160]. D.L. Nika et al. [95, 161] found that the contribution of ZA phonons is negligible due to the large Gruneisen parameter and small group velocity. More recent BTE studies include both the normal and Umklapp scattering process and demonstrated that the out-of-plane acoustic (ZA) modes could dominate the thermal transport in suspended SLG [70, 152, 156]. The dominant contribution from ZA modes can be attributed to the large density of flexural phonons associated with the quadratic ZA branch dispersion and the restricted phase space for the ZA phonon scattering due to the reflection symmetry of two-dimensional graphene [152].

2.2.3 Effects of Extrinsic Interaction on Thermal Conductivity

Effects of Interaction with Substrate/Surrounding on Thermal Conductivity of CNTs

When the CNT forms an interface with substrate or surrounding, the phonons with long MFP, which are responsible for its high thermal conductivity, can be scattered with extrinsic phonons and leads to reduction in thermal conductivity. MD simulations have been reported to investigate the effects of extrinsic interaction on CNT thermal conductivity. For the individual CNTs supported on SiO_2 substrate, Ong and Pop [43] performed equilibrium MD simulations with SED method to determine phonon lifetime. They observe a significant lifetime reduction for low-frequency acoustic phonons which has strong polarization dependence. The thermal conductivity of the supported CNT is ~33% lower than that of the suspended CNT.

Besides the interactions with the substrate, CNTs may interact with surroundings, *e.g.*, air and fluids. Thomas et al. [132] performed NEMD simulations to investigate the thermal conductivities of empty and water-filled single-walled CNTs with diameters

between 0.83 and 1.36 nm and lengths ranging from 200 to 1400 nm. They demonstrate that the thermal transport in water-filled CNTs can become fully diffusive for a relative short length (< 40 nm), and their thermal conductivity is 20%-35% lower than that of empty CNTs. They attribute the thermal conductivity reductions to an increase in low-frequency acoustic phonon scattering due to interactions with the water molecules. Based on equilibrium MD simulations, Donadio and Galli [116] find that that the interaction with an external medium may substantially decrease the lifetime of the low-frequency vibrations, reducing the thermal conductivity by up to 2 orders of magnitude. MD simulations also demonstrate a significant reduction (over a factor of 3) of thermal conductivity in CNTs that are functionalized by chemical moieties, *e.g.*, phenyl rings through covalent bonding (chemisorption) at random positions [130].

Effects of Interaction with Substrate on Thermal Conductivity of SLG

As demonstrated by recent studies using BTE [70, 71, 152, 156], the out-of-plane acoustic (ZA) modes dominate the thermal transport in SLG. These BTE studies show that the significant reduction of thermal conductivity of supported SLG (Figure 2.2) or multi-layer graphene can be well explained by the large suppression of ZA modes due to the SLG-substrate interaction or the interlayer interaction. The dominant contribution from ZA modes can be attributed to a selection rule in BTE method that require an even number of ZA phonons in the three-phonon scattering process [152]. The incorporation of this selection rule can significantly restrict anharmonic phonon-phonon scattering of the ZA modes.

Ong and Pop [162] examined thermal transport in graphene supported on SiO_2 using MD simulations. They find that coupling to the substrate reduces the thermal conductivity of supported graphene by an order of magnitude due to damping of the ZA phonons. However, they find an interesting trend for the thermal conductivity of supported SLG: increasing the strength of the graphene-substrate interaction enhances the heat flow and effective thermal conductivity along supported graphene. They explained that the enhancement is due to the coupling of graphene ZA modes to the substrate Rayleigh waves, which linearizes the dispersion and increases the group velocity of the hybridized modes. However, they use NEMD simulations to determine the thermal conductivity of the thin SLG support on SiO_2 substrate, which can yield a large uncertainty in the calculations of the small portion of heat flux through SLG because the large portion of leakage to the substrate is difficult to quantify.

Contemporarily with this thesis work, Qiu and Ruan [163] performed the equilibrium MD simulations to investigate the relative contributions of ZA phonons to thermal transport. They find that the out-of-plane ZA phonons contribute about 25%-30% to the thermal conductivity of suspended SLG while the in-plane TA and LA phonons make a major contribution in suspended SLG. However, they did not compare the prediction with the values by direct MD simulations and the effects of interaction strength at interfaces remains unclear.

2.2.4 Thermal Transport at CNT Interfaces

MD simulations are extensively used to study the phonon coupling at interface and estimate contact thermal resistances. The previous work on prediction of TBC between CNT and different materials is shown in Table 2.2.

Table 2.2 Thermal boundary conductance calculation at carbon nanotube interfaces.

Contact type	TBC	Methodology	Reference
CNT/SiO_2	0.04 ~ 0.1 W/mK	molecular dynamics	[42]
CNT parallel contact	~ 10000 MW/m^2K	molecular dynamics	[49]
CNT-end/Si	1000 MW/m^2K	molecular dynamics	[164]
CNT-end/Si	5~550 MW/m^2K	molecular dynamics	[165]
CNT/octane-matrix	6~22 MW/m^2K	molecular dynamics	[166, 167]
CNT/Ar-matrix	1.5~2.5 MW/m^2K	molecular dynamics	[168]
CNT/metal-matrix	17 ~ 45 MW/m^2K	molecular dynamics	[83]

MD Simulations for Thermal Transport at CNT-CNT Interfaces

A MD based study by Greaney and Grossman [169] for a system of two SWNTs arranged parallel to each other show that energy exchanges efficiently between two nanotubes for modes in resonance and strongly dependent on the strength of the van der Waals interaction between CNTs. Kumar and Murthy [170] investigated the interfacial thermal interaction between two CNTs placed in the crossed configuration. Their thermal pulse analysis showed that the coupling between the two tubes is very weak and may be dominated by slow-moving phonon modes with high energy. Recently, Xu and Beuhler demonstrate ,using MD simulations, that the thermal resistance at carbon nanotube junctions can be significantly improved by modifying the molecular structure at the interface due to enhancement in the matching of phonon spectra and phonon mode coupling [171]. Polymer wrapping is suggested to improve both the structural stability

and interfacial thermal conductivity of carbon nanotube junctions. Most of the previous studies for exploring the interfacial thermal transport are focused on SWNTs. The mechanism of thermal transport in MWNTs, especially the energy exchange and phonon interaction between different shells of a MWNT is still not well understood.

MD Simulations for Thermal Transport at Interfaces between CNT and Surroundings

MD simulations are primarily used in the previous studies to study thermal transport at interfaces between CNTs and their surroundings. The thermal transport at interfaces between CNT and SiO_2 substrate is of particular interest because of their presence in CNT-TFTs. Ong and Pop [42] investigate thermal coupling between CNTs and SiO_2 using NEMD simulations, and estimate the TBC per CNT length. They find the TBC scales proportionally with the strength of the van der Waals interaction, and the CNT diameter. The TBC also has power-law temperature dependence ($\sim T^{1/3}$) between 200 and 600 K. They show the thermal coupling is dominated by long wavelength phonons between 0-10 THz. Besides, they observe non-negligible high frequency (above the highest phonon frequency in SiO_2, > 40 THz,) components of heat flux power spectrum which indicates inelastic scattering between the CNT and substrate phonons also contributes to interfacial thermal transport (temperature between 300 K ~ 500 K in their simulations) [41, 43].

At interfaces between crystalline Si and vertically oriented CNTs, a small TBC has been reported by several studies [79, 164, 165]. Hu et al. [165] shows adding chemical bonds between CNTs and Si can enhance the TBC by two orders of magnitude. Chalopin et al. [79] and Diao et al. [164] find a large effect of pressure on the thermal

conductance of silicon/carbon nanotube junctions. Chalopin et al. [79] further demonstrate that the opening of pressure induced inelastic phonon channels can result in a several fold increase of the thermal conductance. Besides, the thermal coupling at interfaces between CNT and other materials is also widely studied by MD simulations, including Si, argon matrices [168], metal matrices [83], and liquid solutions [166, 167].

2.2.5 Thermal Transport at Graphene Interfaces

Table 2.3 lists recent calculation of TBC at graphene interfaces. MD simulations and AGF calculations have been reported for the thermal transport at graphene interfaces with various materials, *e.g.*, organic matrix and SiO_2 substrate. Hu et al. [172] perform MD simulation to investigate the thermal transport at interfaces between graphene in organic matrix, and they demonstrate that the thermal conductivity of the graphene filler-organic matrix composites is limited by the interfacial thermal resistance. They find that this limitation can be alleviated by the use of high aspect ratio fillers and by good dispersion. Using a Lennard-Jones (LJ) potential in MD simulations for the non-bonded van der Waals interactions between graphene layers and between graphene and substrate, Ni et al. [173, 174] shows the thermal contact resistance between MLG and SiO_2 is more than one order of magnitude larger than the inter-layer resistance in graphite. They further demonstrate that SiO_2/MLG superlattices have a thermal conductivity as low as 0.30W/mK which is promising for nano-scale thermal insulation.

Table 2.3 Thermal boundary conduction prediction at graphene interfaces

Contact type	TBC	Methodology	Reference
Graphene/organic-matrix	20~170 MW/m^{2}K	Molecular dynamics	[172, 175]
Multilayer graphene/SiO_2	25 ~ 100 MW/m^{2}K	Molecular dynamics	[173]
Graphene/graphene	100~300 MW/m^{2}K	Molecular dynamics	[174]
Graphene-edge/TiC	~750 MW/m^{2}K	Atomistic Green's function	[176]
Graphene on metal (Ni, Cu, Au, Pd)	30~260 MW/m^{2}K	Atomistic Green's function	[81]

Although many experiments have been reported for the TBC at graphene/metal interfaces, few atomistic modeling has been reported to investigate the phonon interaction at such interfaces, especially for MLG/metal interfaces. Huang *et al.* [176] perform AGF calculation to investigate thermal transport across heterogeneous interface between bulk TiC substrates and GNR. The GNR is placed between two TiC substrates in a direction perpendicular to the substrate surfaces and the two edges of GNR are connected to the substrates. The configuration can be used to illustrate the contact of carbon nanotubes with metal substrates, and their results can be extrapolated to get the thermal resistance at CNT interface. They extrapolated Xu and Fisher's measurement on Cu-CNT-Si interface where Ti/Al/Fe metal layer was coated on Si substrate as catalyst, and by scaling the contact area according to the CNT density [177] they obtained a total resistance of 0.4 mm^{2}K/W for the CNT array and its interfaces with Cu and Si. However, the equivalent thermal resistance estimated by AGF calculation was only about 0.0013 mm^{2}K/W which was much smaller than the reported experimental results [177]. The reason can be primarily attributed to the imperfect interface structures in experiments. For CNT arrays grown on Si substrate, the contact structure can be complicated and many CNTs may not make contact with the substrate and many of them may make bad contact leading to large

variation in contact structure and interfacial resistance from one CNT contact to other. The metal layer of Ti/Al/Fe catalyst in experimental samples was amorphous or polycrystalline rather than the single crystalline as in Huang's study using AGF [176]. The nanotubes in Xu and Fisher's study [177] are multi-walled and effective contact area will be significantly reduced if the heat is conducted primarily through the outer wall. The defects in nanotubes will further increase their overall thermal resistance. All these factors are reason for the large mismatch in the AGF and experimental results.

Contemporarily with this thesis work, Mao et al. perform AGF calculation to investigate the TBC at interfaces between graphite and metal including Cu, Au, Ni and Pd. However, their predictions are much larger than the experimental measurements, *e.g.*, TBC at graphite/Au interface is more than two times the highest reported measurement.

So it can be found that previous predictions of TBC at CNT and graphene interfaces using MD simulations and AGF methods vary in a large range, and have a large discrepancy with the experimental measurements. This can be attributed to the limitations of the atomistic modeling methods as well as the complicated interface conditions in experiments.

In MD simulations, empirical potential models are employed to describe the interatomic interactions. Those empirical potential modes are generally developed by fitting the elastic properties, lattice constants, phonon dispersions and energy surfaces for a limited group of materials. Therefore, the transferability of the empirical potential model will affect the accuracy of the MD prediction on TBC. Moreover, quantum effects which are absent in classical MD simulations can introduce uncertainties for materials with high Debye temperature. In the MD simulations of thermal transport, all the phonon

modes available in the simulated materials are fully excited which is valid near and above the Debye temperature of material. Besides, MD simulations are limited to systems below hundreds of nanometers due to the high computational cost. So, the size effect is another important factor that caused the large variations in the studies discussed above. However, MD simulations are still efficient to handle complicated structures and high-order anharmonic phonon scattering. Therefore, in this work, MD simulations are performed for CNT interfaces where the interface structure is complicated.

In AGF calculations, the second-order IFCs used to describe interatomic interactions can be determined using first principle calculations which involve few empirical parameter and has improved accuracy compared with the empirical potential models. Moreover, phonons with all the wavelengths are properly considered using a fine sampling in K-space, and therefore the phonon distribution can be correctly described without quantum effects as in MD simulations. However, anharmonic phonon scattering is absent in AGF simulations because the second-order IFCs only describe the two-body interactions. In cases where anharmonic phonon scattering dominates the thermal transport, *e.g.*, thermal conductivity of bulk materials, the AGF calculation is not suitable unless the anharmonic effects are included properly. So AGF calculations are widely used to study the thermal transport across interfaces where the interface scattering due to phonon mismatch dominates the thermal transport. Since the calculations of IFCs using first principle method are limited to hundreds of atoms, the AGF calculations are generally used for simple interfaces. The AGF modeling of complicated interfaces with roughness and defects requires a real space implementation in which empirical potential models are generally used to describe the interatomic interactions. The simplification of

interface condition is the major source of uncertainty, *e.g.*, the comparison between Huang's AGF calculation of graphene-edge contact with metals and the experimental measurement of the CNT-end/metal interfaces [176]. In current work, AGF calculations are used to predict the TBC at graphene/metal interfaces with well-defined structure. The DFT calculations of IFCs can capture different bonding chemistry at interfaces between graphene and various metals, and provide a good description of interface phonon coupling.

2.4 Contributions of Current Work

The major contributions and important findings of the current work are listed below.

In the study of thermal transport at CNT interfaces:

(1) An atomistic model and MD simulation scheme for CNT junctions on SiO_2 is developed to study the critical heat dissipation process frequently encountered in CNT-network TFTs. The inefficient heat removal from CNTs not making direct contact with the oxide substrate is responsible for the breakdown of CNT network. The low frequency phonon band (0-5 THz) of CNT suspended on other CNTs exhibits two-stage energy relaxation which results from the efficient coupling of low frequency phonons in the CNT-oxide system and the blocking of direct transport of high and intermediate frequency phonons of top CNT to the oxide substrate by bottom CNT.

(2) The energy exchange and coupling of the vibration modes between shells of DWNTs are revealed using MD simulations in the framework of travelling wave packets.

The radial vibration modes are identified as phonons that are strongly coupled and can efficiently exchange energy between shells of DWNTs.

In the study of thermal transport at graphene interfaces:

(3) The thermal conductivity of suspended SLG and SLG supported on Cu is determined using equilibrium MD simulations following Green-Kubo method and relaxation time approximation approach at room temperature. It is demonstrated that the interaction with Cu substrate can significantly reduce the thermal conductivity of SLG, and that the reduction of thermal conductivity from LA (12 %), TA (25%), and ZA (78%) phonons is the major reason.

(4) Using AGF and DFT calculations, the thermal boundary conductance at interfaces across SLG/MLG sandwiched by different metals including Cu, Au, and Ti is predicted. The work shows how the bonding strength changes the graphene/metal and graphene/graphene phonon coupling, and demonstrated the transition of thermal transport mechanism from metal/graphene dominated resistance to graphene/graphene dominated resistance as the metal/graphene bonding strength increases in metal/MLG/metal structure. As a result the TBC can be enhanced through a moderate attenuation of bonding strength at Ti/MLG interfaces which will reduce the mismatch in phonon DOSs between graphene layers and effectively enhance the phonon coupling between Ti and MLG.

CHAPTER 3

METHODOLOGY

Molecular dynamics, lattice dynamics, Boltzmann transport equation, and atomistic Green's function based methods are popular approaches to study the thermal transport at nano-scale. MD simulation and AGF methods are efficient in handling boundary and interface scattering at complicated interface structures, *e.g.*, CNT and graphene interfaces in this work. In the absence of empirical potential models, density functional theory (DFT) calculations can be used to determine the equilibrium atomic positions and interatomic force constants. In this section, MD, AGF, and DFT methods will be briefly discussed in the context of simulation of thermal transport. The specific approaches to determine thermal conductivity and TBC will be discussed.

3.1 Thermal Transport Modeling using Molecular Dynamics Simulations

3.1.1 Spectral Temperature Analysis

In order to investigate the role of phonon interactions in the thermal transport at CNT junctions on SiO_2 substrate, transient relaxation method and SED approach are used to obtain the transient decay of spectral temperature. The SED is obtained by taking the Fourier transform of velocities of C atoms with respect to the frequency ω and wave vector k [168].

$$\theta(\omega,k)=\frac{m}{2}\sum_{j}^{p}\sum_{\alpha}^{3}\left|\frac{1}{N}\sum_{n=0}^{N-1}exp\left(i\frac{n\cdot k}{N}\right)\int v_{j,\alpha}(n,t)exp(-i\omega t)dt\right|^{2} \tag{3.1}$$

where p is the atoms in each unit cell, and N is the total number of unit cells. j, n, and

α are the indices for p, N, and co-ordinate axes, respectively. The dispersion relations can be obtained by plotting the contour of the SED with respect to ω and k. The frequency dependence of the phonon energy distribution can be obtained by analyzing the spectrum of velocity which is determined by taking the Fourier transform of atom velocities with respect to frequency ω [168].

$$\mathrm{g}(\omega)=\frac{1}{3N_{\mathrm{a}}}\sum_{j}^{N_{\mathrm{a}}}\sum_{\alpha}^{3}\left|\int v_{j,\alpha}(t)\,exp(-i\omega t)\,dt\right|^{2} \tag{3.2}$$

where N_{a} is the total number of atoms. By assuming the energy is evenly distributed among all the phonon modes for CNTs at equilibrium, the equilibrium spectrum energy, g^{eq}, can be written as:

$$g^{\mathrm{eq}}(\omega)=\rho(\omega)k_{B}T^{\mathrm{eq}} \tag{3.3}$$

where $\rho(\omega)$ is the phonon density of states and T^{eq} is the equilibrium kinetic temperature. It is further assumed that $\rho(\omega)$ does not change during the transient relaxation, and introduce the spectral temperature $T_{\mathrm{sp}}(\omega,t)$ [168]. The transient spectrum energy can be written as:

$$g^{\mathrm{neq}}(\omega)=\rho(\omega)k_{\mathrm{B}}T_{\mathrm{sp}}(\omega,t) \tag{3.4}$$

In the calculation of transient spectrum energy, the short time Fourier transform is used. The velocities are sampled every 5 fs, which corresponds to the sampling rate of 200 THz. Then the entire time series are divided into blocks of 5 ps length and shift of 0.5 ps. Finally, the spectral temperature of each frequency band can be determined by

$$T_{\mathrm{sp}}(t)=\frac{T^{\mathrm{eq}}}{\omega_{1}-\omega_{2}}\int_{\omega_{1}}^{\omega_{2}}\frac{g^{\mathrm{neq}}(\omega)}{g^{\mathrm{eq}}(\omega)}\,d\omega \tag{3.5}$$

3.1.2 Green-Kubo Formalism for Thermal Conductivity Calculation

In the equilibrium MD simulation, the system is in the linear response regime, and the Green-Kubo method can be used to calculate transport coefficients. The thermal conductivity is related to the equilibrium current-current auto-correlation function by the Green-Kubo expression [178]:

$$k_{\alpha\beta}(\tau_m) = \frac{1}{Vk_BT^2}\int_0^{\tau_m} \left\langle J_\alpha(\tau) J_\beta(\tau) \right\rangle d\tau \tag{3.6}$$

where V is the system volume, k_B is the Boltzmann constant, and $J_\alpha(\tau)$ is the heat flux in x, y or z direction. Periodic boundary conditions should be employed in the heat transport direction. The average of thermal conductivity over the calculated directions can be used as the thermal conductivity of the isotropic system. The Green-Kubo method generally needs a very long simulation time to sufficiently converge the current-current autocorrelation function, especially for a system that has phonon components with a long MFP.

The general expression to calculate the heat flux is

$$\vec{J}(t) = \frac{d}{dt}\sum_i \vec{r}_i E_i \tag{3.7}$$

where E_i is the total energy of an atom. For the three-body potential, it can be expanded as[178]:

$$\vec{J}(t) = \sum_i \vec{v}_i \varepsilon_i + \frac{1}{2}\sum_{i,j}\left(\vec{F}_{ij}\cdot\vec{v}_i\right)\vec{r}_{ij} + \frac{1}{6}\sum_{i,j,k}\left(\vec{F}_{ijk}\cdot\vec{v}_i\right)\left(\vec{r}_{ij}+\vec{r}_{ik}\right) \tag{3.8}$$

The first term is associated with convection, and the second and third with conduction [26]. For a solid system without convection, the first term can be neglected [179, 180].

3.1.3 Relaxation Time Approximation Approach

The anisotropic thermal conductivity ($k_{\alpha\beta}$) can be calculated considering relaxation time approximation [159, 161]:

$$k_{\alpha\beta} = \frac{1}{V}\sum_{s,\vec{q}} \tau(s,\vec{q}) v_{\alpha}(s,\vec{q}) v_{\beta}(s,\vec{q}) C_{ph}(\omega_s) \tag{3.9}$$

Here, v and τ is the phonon group velocity and lifetime, respectively. C_{ph} is the specific heat of a phonon mode of frequency ω:

$$C_{ph}(\omega) = \hbar\omega \frac{dN^0}{dT} = \frac{(\hbar\omega)^2}{k_B T^2} \frac{\exp(\hbar\omega / k_B T)}{[\exp(\hbar\omega / k_B T) - 1]^2} \tag{3.10}$$

The averaged thermal conductivity of SLG is determined by performing integration in the cylindrical coordinates using the dispersion along Γ-M direction while neglecting the anisotropy of the phonon dispersion [161]:

$$k = \frac{1}{4\pi t}\sum_{s} \int_{q_{\min,s}}^{q_{\max,s}} v_s(q)^2 \tau(s,q) C_{ph}(\omega_s) q dq \tag{3.11}$$

Here $t = 3.35$ Å is the thickness of the SLG.

The phonon group velocities are calculated from the phonon dispersion relations predicted using spectral energy density (SED), $v(s,q) = \partial\omega_s / \partial q$. The SED of each branch at certain wave vector and frequency is determined by [132]:

$$\Phi(q,\omega,s) = \frac{1}{4\pi\tau_0 N}\sum_{\alpha}\sum_{b}^{B} m_b \left| e_s \begin{pmatrix} q & \omega \\ \alpha & b \end{pmatrix} \int_0^{\tau_0} \sum_{n_{x,y}}^{N} \dot{u}_{\alpha}\left(n_{x,y}, b, t\right) \times \exp\left[i\vec{q}\cdot\vec{r}\begin{pmatrix} n_{x,y} \\ 0 \end{pmatrix} - i\omega_s t \right] dt \right|^2 \tag{3.12}$$

where α and b are the subscript for direction and basis atom in a unit cell. $n_{x,y}$ is the index for unit cell and $\vec{r}_0\left(n_{x,y}\right)$ is the equilibrium position of each unit cell. e_s is the polarization vector of the basis atom b for the phonon branch α at wavevector q. The

effect of phonon polarization vector is incorporated in the calculation of mode dependent SED which has been neglected in the previous studies [132]. It is obtained from the harmonic lattice dynamics calculations using the GULP [181] code with optimized Tersoff potential. The phonon lifetime ($\tau = 1/2\gamma$) is obtained by fitting the SED to the Lorentzian function as [132]:

$$\Phi(q,\omega,s) = \frac{I}{1+\left[\left(\omega-\omega_c\right)/\gamma\right]^2} \tag{3.13}$$

where I is the magnitude of the SED peak, ω_c is the peak center frequency, and γ is the half-width at half-maximum. In this method, the full anharmonicity of the atomic interactions can be incorporated into the prediction of phonon lifetime and dispersion relations. The scattering of phonons at the interface with substrate due to the nonperiodic interactions can also be taken into account.

3.2 First Principle Calculations of Interatomic Force Constants

In this work, DFT is used to calculate the second order force constants $\Phi_{ij}^{\alpha\beta}$ for the harmonic matrix of AGF calculations [182].

$$\Phi_{ij}^{\alpha\beta} = \frac{\partial^2 E}{\partial r_i^\alpha \partial r_j^\beta} = -\frac{\partial F_j^\beta}{\partial r_i^\alpha} \tag{3-14}$$

A finite displacement method is used to calculate $\Phi_{ij}^{\alpha\beta}$ using forces acting on atom j in β direction under displacements $\pm\Delta r_i^\alpha$ of atom i in α direction [183, 184].

$$\Phi_{ij}^{\alpha\beta} \approx -\frac{F_j^\beta\left(r_i^\alpha+\Delta r_i^\alpha\right)-F_j^\beta\left(r_i^\alpha-\Delta r_i^\alpha\right)}{2\Delta r_i^\alpha} \tag{3-15}$$

3.3 Atomistic Green's Function Calculations

In the AGF model as shown in Figure 3.1, the device (D) region is sandwiched between two contacts: left contact (LC) and right contact (RC). The region beyond LC or RC is defined as left contact bulk (LCB) or right contact bulk (RCB) which does not interact with the device region. A group of unit cells whose primitive atoms share the same z coordinate are considered to be in the same layer. A unit cell can interact with unit cells in the nearest layer on either side of it. The purpose of defining the unit cell layers is to write the harmonic matrices in a finite plane-wave form so that an efficient sampling in transverse Brillouin zone $\vec{k}_{\parallel} = (k_x, k_y)$ can be used to include the phonons with all wavelengths [185, 186].

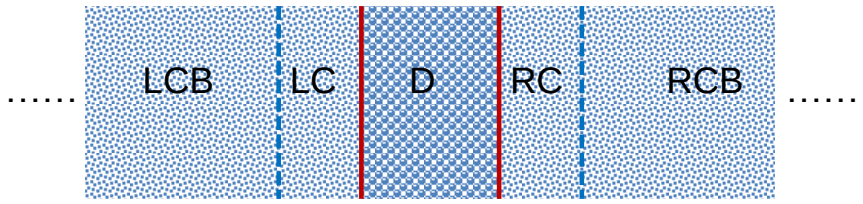

Figure 3.1 Schematic of contact-device-contact setup in AGF calculation. LCB, LC, D, RC, and RCB are left contact bulk, left contact, device, right contact, and right contact bulk, respectively.

The thermal conductance across the device region is determined by:

$$\sigma = \int_0^{\infty} \int_{\vec{k}_{\parallel}} \frac{C_{ph}(\omega, T)}{2\pi} \Xi\left(\omega, \vec{k}_{\parallel}\right) \frac{d\vec{k}_{\parallel}}{(2\pi)^2} d\omega \tag{3.16}$$

where $C_{ph}(\omega,T)$ is the specific heat of a phonon mode of frequency ω at temperature T. $\Xi\left(\omega,\vec{k}_{\|}\right)$ is the transmission function at frequency ω and transverse k-point $\vec{k}_{\|}=(k_x,k_y)$. [185-187]

$$\Xi\left(\omega,\vec{k}_{\|}\right)=\text{Trace}\left[\Gamma_{\text{L}}G_{\text{LD,RD}}\Gamma_{\text{R}}G_{\text{LD,RD}}^{\dagger}\right] \tag{3.17}$$

where Γ_{L} and Γ_{R} are the escape rates to the LC and RC, respectively. $G_{\text{LD,RD}}$ and $G_{\text{LD,RD}}^{\dagger}$ are the upper right block matrix in the device Green's function matrix and its complex conjugate. The density of states (DOS) in each region shown in Figure 3.1 can be directly obtained from its Green's function. [187]

$$D(\omega)=\frac{i\left(G-G^{\dagger}\right)\omega}{\pi} \tag{3.18}$$

CHAPTER 4

MOLECULAR DYNAMICS SIMULATIONS OF HEAT DISSIPATION AT CARBON NANOTUBE JUNCTIONS ON SILICON OXIDE SUBSTRATE

In applications such as CN-TFTs, the random CNT network is supported on an oxide substrate [40, 188]. Inefficient heat removal from CNT network can lead to breakdown of the device as shown in Figure 4.1. A close observation of these networks [40, 188] reveals that many CNTs may not be directly touching substrate, but partially or fully supported by other CNTs. Such structures can lead to the localized hot spots in the CNT networks and can pose severe reliability issues to the TFTs. The phonon transport at these CNT junctions significantly affect their TBC, temperature rise and hence CN-TFT performance and reliability. However, the phonon transport across CNT junction structures supported on a SiO_2 substrate has not been explored. MD simulations are suitable for the modeling of thermal transport at CNT junctions which have complicated interface structures. This type of atomistic modeling using MD simulation can provide important inputs for device scale models. For example, the MD results of the junction structures have been used in a coupled electro-thermal model by Gupta *et al.* [189] to analyze the effects of TBRs at CNT interfaces on electrical breakdown of CN-TFTs. Based on the MD simulation results, further calculation and analysis of phonon coupling can provide insights into possible modifications of molecular structure at the interface to enhance the phonon spectra matching for better heat removal from the CN-TFTs [46].

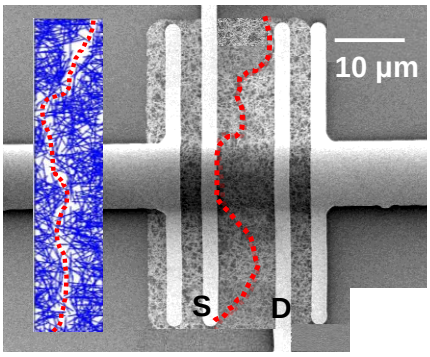

Figure 4.1 Random CNT network after the breakdown from electro-thermal simulations [189](left inset, channel region) to scanning electron microscopy (SEM) image of the CN-TFT in experiments [37].

This chapter presents analysis of the heat dissipation and phonon interactions at CNT junctions supported on SiO_2 substrate (shown in Figure 4.2) using MD simulations. The morphology of CNT junctions supported on an oxide substrate is obtained after equilibration process in MD simulations. At similar power densities, the temperature in hanging CNTs (~ supported by only other CNTs) can be hundreds of degree higher compared to the CNTs well-contacted with the substrate leading to early breakdown. The decay of thermal energy in CNTs fully suspended on other CNTs and substrate supported CNTs is investigated using the spectral temperature, and the frequency dependence of energy relaxation from CNTs to SiO_2 is analyzed.

4.1 Simulation Setup and Parameters

4.1.1 MD Simulation Parameters and Procedure

In CN-TFT, CNT networks are made from randomly distributed CNTs. IR measurements of temperature distribution in CN-TFT with 25 nW power dissipation [37]

showed that the CNT network could breakdown at an average temperature (~105 ^{o}C) in the channel region which was well below the breakdown temperature (~600 ^{o}C in air) of individual CNTs [190]. It is suggested that such the early breakdown at relatively low temperature could be attributed to highly localized nanometer-scale hot-spots at the CNT junctions, which cannot be captured by the IR microscopy with a resolution of ~2 μm [37]. Therefore, the thermal transport at CNT junctions on SiO2 substrate is the critical process for the heat dissipation in CN-TFT. In current work, three configurations of CNT junctions on SiO_2 are modeled in MD simulations (see Figure 4.2) in order to develop an understanding of heat dissipation and phonon interactions in CNT networks supported on SiO_2 substrate. System I consists of a single CNT directly supported on the SiO_2 substrate, while the CNTs in System II and III are placed on one and two perpendicular CNTs, respectively. System II represents a typical crossed CNT junction in the CNT network of a CN-TFT, while system III represents CNTs in a high density network which is only supported by other CNTs and which do not make direct contact with the substrate. The substrate is periodic in x (length) and z (width) directions; it has 24,052 atoms and its dimensions are 285.0 Å × 23.7 Å × 59.6 Å.

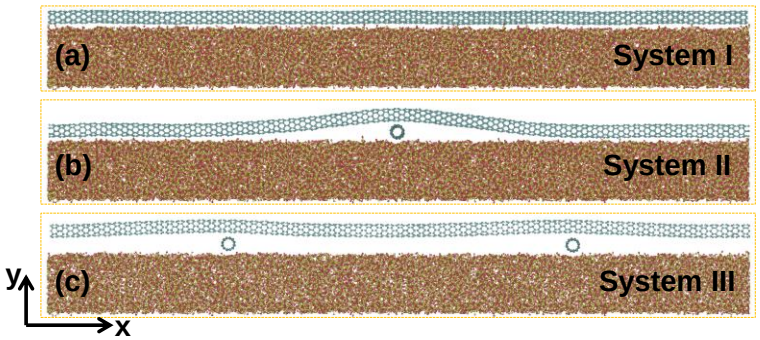

Figure 4.2 Configurations of (a) System I, (b) System II, and (c) System III. These Systems are equilibrated at 375K.

The distance between the two bottom CNTs in System III is half of the substrate length in x-direction which ensures a symmetric configuration on two sides from the center of substrate. The CNTs in the simulations have a chirality of (6, 0) and diameter of 4.7 Å. The MD simulations are implemented in Lammps package [191]. To describe C-C interactions in CNTs, the adaptive intermolecular reactive empirical bond order potential (AIREBO) [192] is used. For the amorphous SiO_2, the Munetoh parameterization [193] of the Tersoff potential is used to describe the Si-Si, O-O, and Si-O interactions. The vdW interactions between the CNT atoms at the interface are modeled by Lennard-Jones potential, $V_{ij}(r) = 4\varepsilon_{ij}\left[\left(\sigma_{ij}/r\right)^{12} - \left(\sigma_{ij}/r\right)^{6}\right]$. The present study employs the L-J parameterization used by Zhong and Lukes [49], with $\varepsilon_{\text{C-C}} = 4.41\,\text{meV}$ and $\sigma_{\text{C-C}} = 0.228\,\text{nm}$. The vdW interaction between the C-Si and C-O are also modeled using a L-J potential with the parameters from the universal force field (UFF) model by Rappe et al [194]. The parameters are $\varepsilon_{\text{C-Si}} = 8.909\,\text{meV}$, $\varepsilon_{\text{C-O}} = 3.442\,\text{meV}$, $\sigma_{\text{C-Si}} = 0.3326\,\text{nm}$, and $\sigma_{\text{C-O}} = 0.3001\,\text{nm}$ similar to parameters used in Reference [195, 196].

In the MD simulations, the atoms in the bottom layer of substrate are fixed to anchor the substrate. A time step of 0.25 fs is used for all simulations. In order to obtain the equilibrium structures, an energy minimization on the CNTs and amorphous SiO_2 system is first performed and then the system is equilibrated using NPT at 1 bar and 375 K for 1 ns. A very small force (<0.001 eV/Å on each atom) is applied on the top CNT during the first 0.25 ns simulation in NPT to prevent the CNT to fly away from the system, and afterward the force is removed. Following the NPT equilibration, the volume

of simulation box is determined, and the equilibration is continued using NVT at 375 K for 1 ns.

4.1.2 Equilibrium Structures of CNT Junctions

The structures after equilibration are shown in Figure 4.2. The deformation in CNTs due to the interaction with substrate is observed to be very small and its cross-section remains in circular shape after the equilibration, which is expected for small-diameter CNTs (d<21 Å) [40]. The single CNT in System I is completely supported by the substrate and remains straight after the equilibration like an isolated CNT. The top CNT in System II has a curvature near the region supported by the bottom CNT. The minimum distance between the top CNT and SiO_2 substrate in System II is shown in Figure 4.3. The curvature region spans 91 Å, which is about 20 times of the CNT diameter. As the spacing between the bottom CNTs supporting top CNT decreases, the top CNT get fully detached from the substrate as in System III and only has a slight bending toward the substrate at the ends.

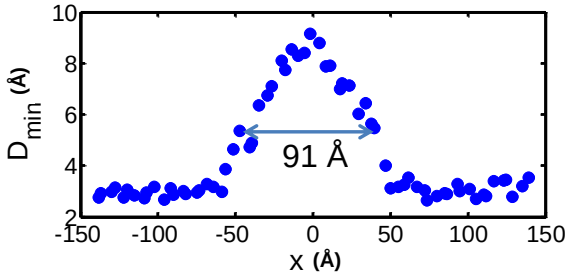

Figure 4.3 Minimum distance between top CNT and SiO_2 substrate in System II (see Figure 4.2 (b)). Here, x=0 corresponds to the mid-point of the bottom CNT.

4.2 Validation of Simulation Parameters

4.2.1 Justification of Empirical Potential Models

REBO potential models [127, 192] have been used for MD simulations of CNTs by many studies. In this work, the selection of REBO potential is further justified by validating its prediction of radial breathing mode (RBM) frequency of CNT with different diameters. The RBMs are formed when the out-of-plane acoustic modes of a graphene sheet are rolled into a nanotube [197]. RBMs are optical phonon modes with non-zero frequency at Gamma point of first Brillouin zone. The RBM is Raman-active, and its frequency has strong dependence on CNT diameter. So the measurement of RBM frequency by Raman spectroscopy is one of the most popular techniques to characterize CNT structures [198, 199]. The frequencies of phonon modes at Gamma point including RBM are determined using LD calculations with REBO potential model. Figure 4.4 shows the comparison of LD prediction and experimental measurements [198]. The experimental results were well fitted by the function $\omega_{\mathrm{RBM}} = 223.75\left(\mathrm{cm}^{-1}\mathrm{nm}\right)/d\left(\mathrm{nm}\right)$. The good agreement between LD predictions and measurements indicates the REBO potential model can well describe the phonon properties of CNTs.

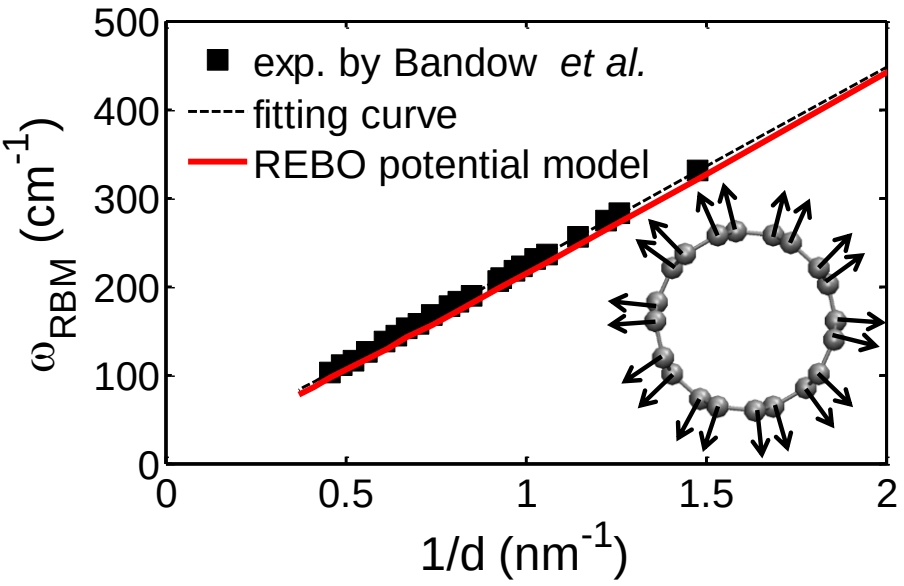

Figure 4.4 Dependence of the frequency of radial breathing mode on nanotube diameter. The experimental measurements and fitting curve are from Ref. [198]. The inset shows the displacement of carbon atoms corresponding to radial breathing modes.

The interatomic interactions in SiO_2 are described by Tersoff potential. The potential parameterization by Munetoh et al. [193] is employed. This parameterization has been validated by reproducing the lattice constants, density, and cohesive energy. In particular, the prediction of vibrational DOS of bulk amorphous SiO_2 was in good agreement with experimental data [200]. At non-bonded interfaces including CNT-CNT interface and CNT-SiO_2 interface, the nature of van der Waals interaction can be described by L-J potential model which has been widely used in many MD simulations of CNTs [41-43, 49, 168].

4.2.2 Length Effects

Length effect is significant for thermal conductivity of CNTs. For thermal transport at CNT junctions or between CNT and SiO_2, phonon scattering at interfaces is the dominating factor which make length effects insignificant. It has been demonstrated by Carlborg et al. [168] that the SWNT-length effect on the TBC was absent for SWNT lengths from 20 to 500 Å. The lengths of top CNT and bottom CNT are 285 Å and 59.6 Å, respectively. The length effect is checked by increasing the length of top CNT to 400 Å and performing the energy relaxation simulations for structure of System I. The results are shown in Figure 4.5. The relaxation time for 40 nm CNT is 121 ps which is quite closed to that of 28.5 nm CNT (119 ps).

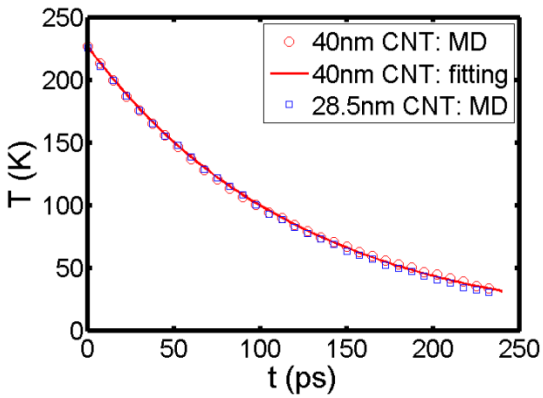

Figure 4.5 Transient decay of temperature difference between top CNT and substrate. CNT is fully supported on SiO_2 substrate as in System I of Figure 4.2. Red circles and red line are for 40 nm CNT while blue squares are for the 28.5 nm CNT used in the manuscript.

4.3 Heat Dissipation under High Power Density

In the direct MD method, the heating power in the range of 5 nW to 26.5 nW is applied on the top CNT by rescaling the velocities of atoms. The maximum value 26.5

nW is selected following the experimental results [188] of the breakdown power of CNTs at high temperatures. A thermostat is applied to a 5 Å thick region above the fixed layer of SiO_2 substrate to control its temperature at 375 K. The simulations are performed on the three configurations prepared by the equilibration (Figure 4.2). Each case is simulated for 15 ns (25 ns for system III) to obtain a steady state, and then the data are sampled for 5 ns. During the sampling period, the temperature is calculated within 67 slabs along the CNT by

$$\frac{3}{2} n k_B T = \frac{1}{2} \sum_i^n m_i v_i^2 \tag{4.1}$$

where n is the number of atoms per slabs, and m_i and v_i are the mass and velocity of each atom. k_B is the Boltzmann's constant.

4.3.1 Temperature Variations along CNTs

Since the CNTs in the present simulations are relatively short and have very large thermal conductivity in the length direction, the temperature variations along the top CNTs are very small. The top CNT in System I is in complete contact with the substrate and in system II is also primarily supported by the substrate; consequently small temperature variations (< 3 K) has been observed.

The top CNT in System III is supported by two bottom CNTs with a small contact. The section of top CNT between the supports can be treated as suspended CNT, and the contact with the bottom CNTs acts as heat sinks. The temperature distribution along the top CNT in System III at heating power of 26.5 nW is shown in Figure 4.6; the variations are within 10 K, but larger than that in the other two Systems. The two minima

in temperature are at coordinates of around -75 Å and 75 Å (Figure 4.3), where the bottom CNTs are located. So the input power to top CNT is first transferred to two bottom CNTs through the small contact area at CNT junctions, and then conducted to the substrate through the bottom CNTs.

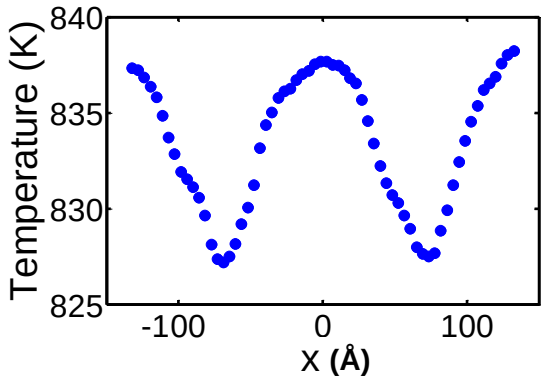

Figure 4.6 Temperature distribution along the top CNT in System III at heating power of 26.5 nW

4.3.2 Temperature Rise under High Heating Power

The temperature variation in top CNT at different heating power is shown in Figure 4.7. The temperature rise for the fully supported (~System I) or partially supported CNT on SiO_2 (~System II) is not large, even at a high power density. However, the temperature increases rapidly when the top CNT is only supported by bottom CNTs and do not make any direct contact with the substrate (~System III). The contact area between the small diameter tubes is very small, and the inefficient heat conduction between CNTs can lead to this overheating in the top CNT at high power density. In present simulations, the temperature of top CNT increases beyond 834 K at the heating power of 26.5 nW which suggests that the breakdown temperature (873 K) [44, 188] will be easily reached in such CNTs even though the other CNTs in the network will be at much lower

temperatures (~ 400 K).

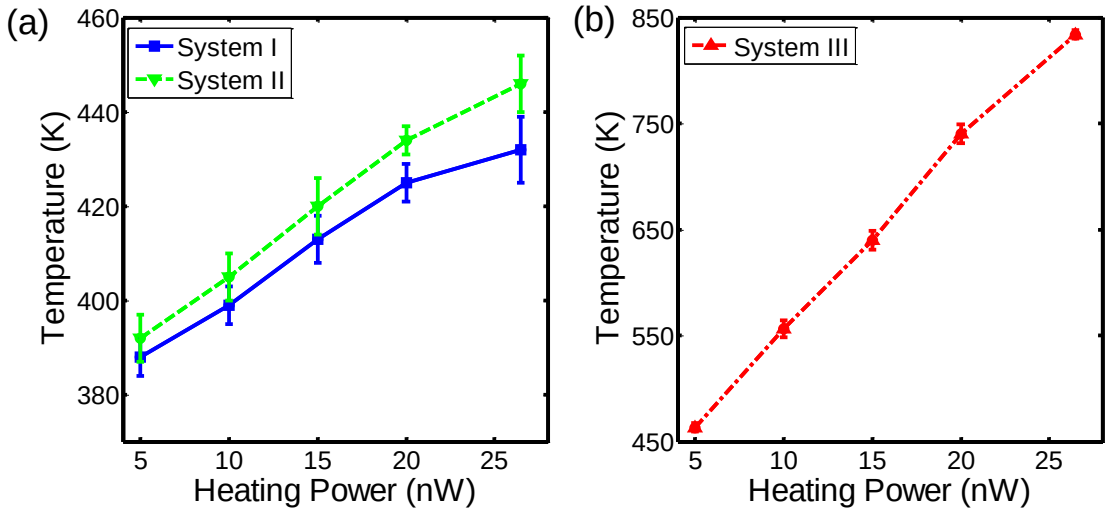

Figure 4.7 Temperature variations of top CNT in (a) Systems I and II and (b) System III as a function of heating power. The error bars indicate the standard deviations calculated from ten MD samples for 0.5 ns each.

4.3.3 Thermal Resistance Network Analysis

As shown in Figure 4.3, the CNT contact area with the substrate in System II is reduced by 32% compared to System I but its temperature rise is only about 10 K (Figure 4.6) larger than that in System I. So it is of high interest to find how the heat is conducted to the substrate in System II. As shown in Figure 4.8 (a), there are two heat conduction paths: (i) in the first path heat is directly conducted from top CNT to the substrate and the important thermal conductance is $g_{\text{CNT-sub}}$ (see System I), and (ii) in the second path heat is conducted first to bottom CNT and then to SiO_2 substrate; the important thermal conductance are $G_{\text{CNT-CNT}}$ and $g_{\text{CNT-sub}}$ (see System III).

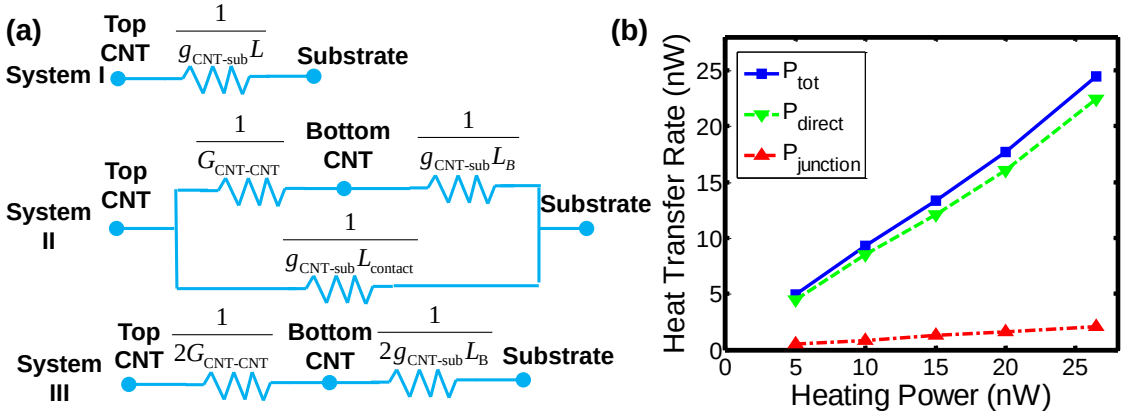

Figure 4.8 (a) Equivalent thermal resistor circuit of Systems I, II and III. (b) Rate of heat transfer via CNT-SiO_2 direct contact and CNT-CNT junction in System II. L and L_B are the lengths of top and bottom CNTs, respectively. $L_{contact}$ is the length of top CNT directly contacted with SiO_2 in System II.

Due to the 1-D structure of CNT, thermal conductance between CNT and substrate is defined as the rate of heat transfer per unit length (W/mK). Thermal conductance at CNT junction is not normalized with contact area and has unit of W/K. It is further assumed that interfacial thermal conductance through these two paths in System II equals to corresponding values in System I and III, respectively. Based on the thermal resistor circuit shown in Figure 4.8 (a), the overall conductance from top CNT to SiO_2 substrate for each system can be obtained.

$$G_{\mathrm{I}} = g_{\text{CNT-sub}} \cdot L \tag{4.2}$$

$$G_{\mathrm{II}} = g_{\text{CNT-sub}} L_{\text{contact}} + \left(\frac{1}{G_{\text{CNT-CNT}}} + \frac{1}{g_{\text{CNT-sub}} \cdot L_{\mathrm{B}}} \right)^{-1} \tag{4.3}$$

$$G_{\mathrm{III}} = \left(\frac{1}{2G_{\text{CNT-CNT}}} + \frac{1}{2g_{\text{CNT-sub}} \cdot L_{\mathrm{B}}} \right)^{-1} \tag{4.4}$$

Using the temperature response at different heating power (Figure 4.7), thermal conductance $g_{\text{CNT-sub}}$ and $G_{\text{CNT-CNT}}$ can be determined. Thermal conductance $g_{\text{CNT-sub}}$ is estimated as 0.014 W/mK. Reference [195] gave an expression to estimate thermal conductance between CNT and SiO_2 substrate for the CNT diameter in the range of 0.81~1.63 nm and temperature in the range of 200~600 K. However, CNT diameter considered in present work is only 0.47 nm which is much smaller than the lower limit in Ref. [195]. By extrapolating beyond the diameter range studied in Ref. [195], the thermal conductance of 0.029 W/mK is obtained at 375K. The thermal conductance of CNT junction is 0.042 nW/K which is approximately twice of the value (~0.02 nW/K for CNTs with diameter of 0.5 nm) determined by atomistic Green's Function Calculations in Ref. [48].

Based on thermal conductance $g_{\text{CNT-sub}}$ and $G_{\text{CNT-CNT}}$, the rate of heat transfer via two different paths in System II can be determined, as shown in Figure 4.8 (b). It can be observed that heat is mainly conducted through the direct contact with the substrate, and less than 10% of the power is dissipated through the CNT-CNT junction. Since the CNTs have a high thermal conductivity, the heat generated in the buckled section of the top CNT can be first efficiently conducted along the tube to the sections supported by the SiO_2 substrate and then get dissipated to the substrate. Even if the contact length with the substrate is reduced by 32% in System II, the heat can still be effectively dissipated through the reduced contact length (~18 nm) with a relatively small temperature rise. This agrees well with the previous measurements which suggest that relatively short contact lengths (10-30 nm) to a typical solid should be sufficient to transfer heat efficiently [201].

The overall thermal conductance can be estimated at each interface in System III. Thermal conductance at CNT-CNT interfaces is about 0.084 nW/K which is half of the thermal conductance (0.172 nW/K) between bottom CNT and SiO_2 substrate. This indicates enhancing heat transfer at CNT junction will yield the largest gain. Besides, a low CNT junction density can also help to maintain a good contact between CNT and SiO_2 and avoid the fully suspended CNT structures as in System III; such CNTs should be removed from the CNT network in order to avoid hot spots.

4.4 Spectral Analysis of Transient Thermal Relaxation

In the simulations, an initial temperature difference ΔT is set between the top CNT and bottom CNTs/SiO_2 substrate. The bottom CNTs and SiO_2 substrate is set at 375 K, and the top CNT is set at 600 K. This is achieved by first equilibrating the top CNT 600 K for 100 ps in the three configurations previously prepared by equilibration. The temperature of the bottom CNTs and SiO_2 substrate is kept at 375 K. The temperature is controlled by the velocity rescaling thermostat. Then, the thermostat is switched off, and the system is allowed to relax for 0.25 ns and 0.5 ns for System I and System III, respectively. The relaxation is simulated in a NVE ensemble [195, 196]. The temperature profile and the SED are averaged over every 10 time steps to reduce the random fluctuations of MD simulations.

In order to develop an understanding of the phonon coupling at the interfaces, the entire frequency range is divided into four bands, as shown in Figure 4.9 (b). Band 1 is the low frequency region below 5 THz which is most important for the energy transfer across interfaces. Band 2 and 3 corresponds to the frequency range of 5-12 THz and 12-

40 THz. The overlap between the frequency spectrum of CNTs and SiO_2 exists in all the first three bands. Band 4 spans from 40 THz to 55 THz which has no overlap between frequency spectrum of CNTs and SiO_2. The SED $\theta(\omega,k)$ and the frequency dependence of the spectral energy $g(\omega)$ of the CNT in system I are similar to system III.

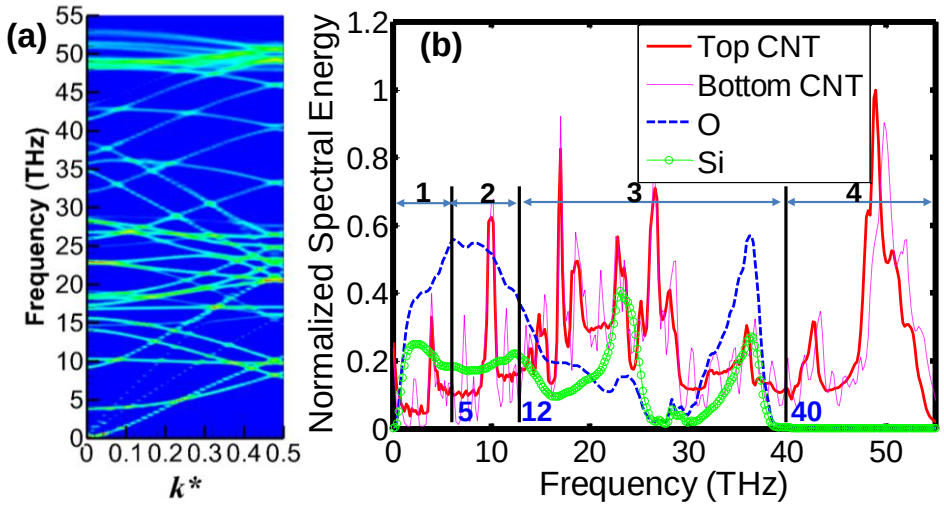

Figure 4.9 (a) Phonon dispersion relations of top CNT in system III at T=375 K. k^* is wave vector normalized with respect to $2\pi/a_z$. (b) Normalized phonon spectral energy of system III at different frequencies at T=375 K. The spectral energy of C (in top and bottom CNTs), Si, and O is normalized to the maximum value of spectral energy of C atoms in top CNT. The frequency ranges of four phonon bands (1-4) are shown.

The transient decay of spectral temperature $T_{sp}(t)$ and its difference to the substrate temperature $\Delta T_{sp}(t)$ are shown in Figure 4.10 (a) and (b) for system I and in Figure 4.10 (c) and (d) for system III. The relaxation time constant, τ, of the spectral energy of each band is obtained by fitting the spectral temperature with an exponential function, i.e., $\Delta T_{sp}(t) = \Delta T_0 \exp(t/\tau)$. The relaxation time of the overall temperature of

the top CNT in System I is 119 ps (Figure 4.10 (b)). The spectral energy of band 1 decays fast with a relaxation time of 70 ps, while the spectral energies of the other three bands decays slowly with relaxation times (~115-121 ps) close to the overall temperature (Figure 4.10 (b)). The fast relaxation of the low frequency spectral temperature indicates an efficient energy transfer across the interface, which confirms the importance of the low frequency phonons in the interfacial heat transfer [196, 202]. As shown in Figure 4.9 (b), there is no overlap in phonon spectrum of CNT and SiO_2 in band 4. It can be observed that ΔT_{sp} of the band 4 (not overlapping with SiO_2) also decays at nearly the same rate as the overall temperature. The phonons in band 4 of CNT have to dissipate energy to its own bands 1-3 (below 40 THz and overlapping with SiO_2) to transfer energy to SiO_2 substrate. This intra-tube energy transfer must be much faster than the interfacial energy transfer [203]. The similarity between the energy relaxation of bands 2, 3 and 4 may also indicates that the energy in band 4 primarily dissipate to band 2 and 3 (Figure 4.10 (b)).

Compared to System I, System III has a much larger relaxation time (~1372 ps) for the overall temperature decay of the top CNT (Figure 4.10 (c) and (d)). The spectral temperature in band 2 to 4 decays similar to the overall temperature. However, the energy in band 1 has a two-stage decay characteristic, and cannot be described by a single relaxation time. So the $\Delta T_{sp}(t)$ is fitted to the sum of two exponential functions: $\Delta T_{\mathrm{sp}}^{1}(t) = \Delta T_{0,a}\exp(t/\tau_{1,a}) + \Delta T_{0,b}\exp(t/\tau_{1,b})$. The first stage is very fast with a relaxation time, $\tau_{1,a}$, of 47 ps, but the second stage is much slower ($\tau_{1,b}$=2132 ps).

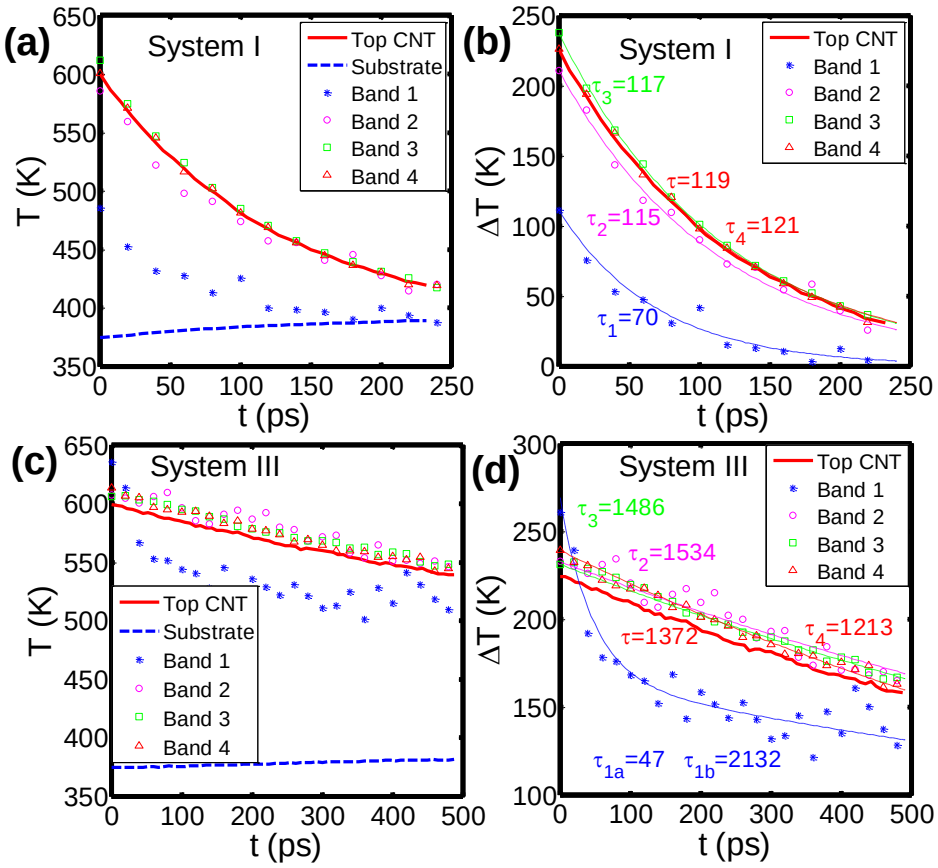

Figure 4.10 Top CNT total temperature, substrate temperature, and spectral temperature (T_{sp}) of four frequency bands (see Figure 4.9 (b)) of top CNT in (a) System I and (c) System III. The transient decay of difference between top CNT total temperature (or spectral temperature of phonon bands) and substrate temperature (ΔT) for (b) System I and (d) System III. The unit of time constant is picosecond.

In System III, the top CNT is supported only by bottom CNTs and have a small contact area and weak vdW interactions at the interface. The tube-tube energy transfer is mainly achieved by the low frequency phonons [46, 48]. As shown in Reference [48] using the atomic Green's function calculation, the phonon transmission above 10 THz is strongly suppressed, and this frequency threshold becomes even smaller for small

diameter CNTs. For the CNT of chirality (6, 0) in this work, the phonon transmission has diminished to nearly zero for frequency above 8 THz [48]. In this stage the energy carried by low frequency phonons, which are excited during heating process, is transferred to the lower CNTs/substrate rapidly due to the efficient coupling between the low frequency modes.

The second stage ($\tau_{1,\,b}$=2132 ps) may corresponds to the phase when the energy in high frequency bands (2 to 4) is first transferred to band 1 before getting transferred to lower CNT and the substrate. As shown in Figure 4.10 (d), the time constant of spectral temperature relaxation is smallest for the highest frequency band but largest for the second stage of the low frequency band ($\tau_4 < \tau_3 < \tau_2 < \tau_{1b}$). This is because bottom CNTs block the energy transfer through the direct coupling of high frequency phonons and the energy from high frequency band need to be first transferred to the lower frequency band. The energy can get accumulated in these high frequency modes. As dominant energy content is in the high frequency bands, the slower relaxation of energy in high frequency bands (~2 to 4) to low frequency band (~1) as reflected in high $\tau_{1,\,b}$ and absence of direct coupling of high frequency phonons may become bottleneck for energy exchange at interface.

In system III, the bottom CNT works as a frequency filter which blocks the direct energy transfer via the high frequency phonons from top CNT to substrate. Coupling of higher frequency phonons can help to enhance the heat transfer at CNT junctions, which may be achieved by nano-engineering the CNT-CNT interfaces through polymer wrapping, metal coating and linker molecules [46, 60]. Polymer molecules or smaller linker molecules can also be used as fillers to bridge the gap between top CNT and SiO_2.

Besides, CNTs with larger diameter can have larger interfacial thermal conductance and contact area [46, 189]. But larger diameter can increase the buckling length of top CNTs, and thereby significantly reduce the contact area with substrate and deteriorate the heat dissipation around CNT junctions [189].

4.4 Closure

In summary, the present section investigates the heat dissipation at CNT junctions supported on SiO_2 substrate using direct method and transient relaxation method of MD simulations. A CNT junction can reduce the contact of top CNT with the SiO_2 substrate by about 20 times of the CNT diameter, but the temperature of top CNT heated by high power does not increase rapidly until it becomes fully suspended. The relatively short contact length (~18 nm in present work) of CNT with substrate is sufficient for the heat removal at a high power density with an acceptable increase of temperature rise. However, CNTs fully suspended on other CNTs can reach to breakdown temperature at similar power density. In a CN-TFT with high density network, such suspended CNTs will be prone to early breakdown. The role of phonons in the interfacial energy transfer in the supported CNT junctions is examined by analyzing the spectral temperature decay. The importance of the low frequency phonons in the interfacial thermal transport is confirmed by its fast relaxation. The bottom CNT in the supported CNT junctions blocks the direct transport of high frequency phonons of top CNT to the oxide substrate. The primary energy exchange in CNT-CNT-oxide junctions is through low frequency phonons in the range of 0-10 THz. The energy carried by these low frequency phonons in the fully suspended CNTs decays in two stages. The second stage seems to corresponds

to intra-tube energy exchange from high frequency bands to low frequency bands in top CNT and then to the bottom CNT and substrate.

The MD simulation results in this chapter can be validated against measurements of temperature in CNTs with varied electrical heating. Experimental work has been reported to study the heat dissipation in single CNT on SiO_2 [40, 44, 45, 89] and thermal contact resistance at suspended CNT junctions [47]. It is possible to fabricate a micro-device which consists of CNTs with single or several junctions on SiO_2 substrate. With the connection to metal electrodes at both ends of CNT, electrical heating can be generated in the CNT [40, 44, 45, 89]. For better comparison with experimental measurements, the current work should be extended to CNTs with larger diameter, *e.g.*, CNTs with 1-2 nm diameters as typically observed in the experiments related with CNT TFTs. Once validated with the experimental measurements for representative cases, extensive MD simulations can be carried out for various CNT junction structures, and a database that summarizes the results can provide important inputs for the CNT network based TFT devices and other applications.

CHAPTER 5

MOLECULAR DYNAMICS SIMULATIONS OF HEAT PULSE PROPAGATION IN DOUBLE-WALL CARBON NANOTBES

MWNTs, which are predominately metallic, have been studied for interconnect application in order to improve current carrying capacity [16, 17, 65]. Due to their high thermal conductivity, MWNT interconnect can also serve as important heat transfer pathway. Due to the imperfect contact at MWNT ends with surroundings, the heat conduction may not be uniformly distributed across the shells of MWNTs. In order to maximize the heat conduction along MWNTs, it is import to understand and improve the thermal coupling between shells of MWTNs.

In this chapter, thermal energy transport between shells of DWNTs is investigated in the framework of travelling wave packets. The thermal transport in DWNT subjected to a heat pulse is compared against the thermal transport in SWNTs in similar conditions. A strong heat pulse is generated in the middle of inner or outer layer of DWNTs; the energy exchange and coupling of the vibration modes between these layers is analyzed through the kinetic energy corresponding to the velocities in the radial, tangential, and longitudinal directions. The wavelet analysis is then performed on these velocity components in order to elucidate the thermal interaction between layers of DWNTS in the frequency domain. This work can help to understand the phonon interactions between shells of DWNTs and identify the vibration modes which are strongly coupled between shells and which efficiently exchange energy.

5.1 Simulation Setup and Parameters

5.1.1 Structures of DWNTs

In order to develop such understanding of energy exchange and phonon interactions in DWNTs, heat pulse propagation is studied using MD simulations and wavelet methods on six different configurations of CNTs shown in Figure 5.1.

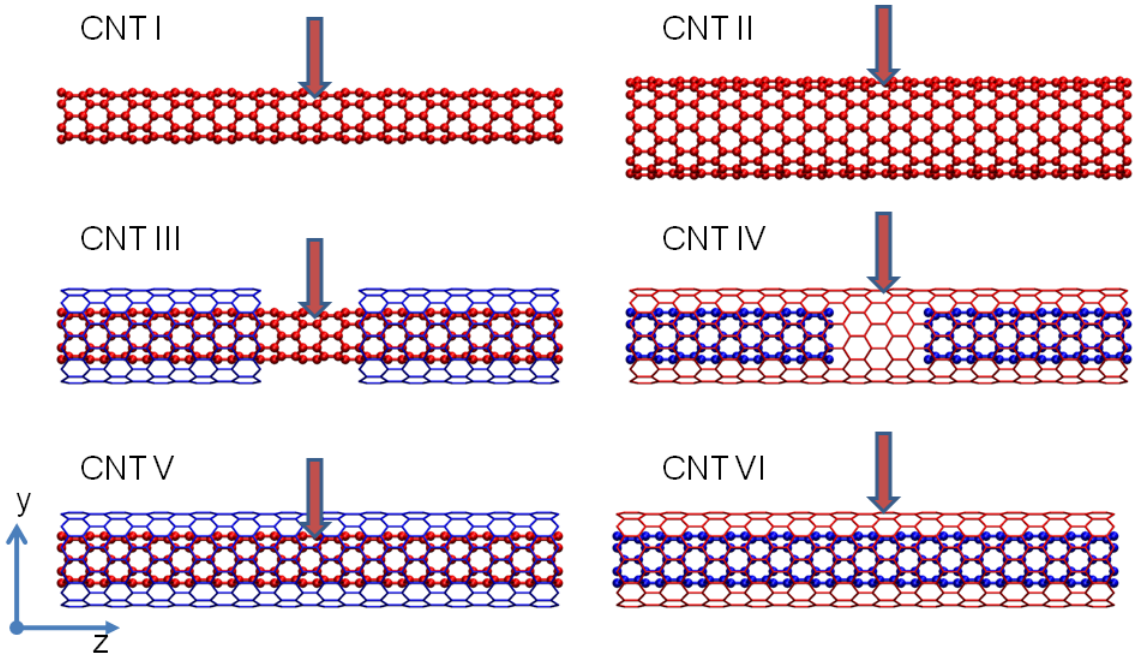

Figure 5.1 Schematic of CNTs in simulations (atoms of the outer layers are not shown for clarity). CNT I and CNT II are 200 nm long SWNTs with chirality of (6, 0) and (12, 0) respectively; heat pulse is applied in the middle 10 slabs for these CNTs. CNT III is a 200 nm DWNT with a 50 nm cut in the middle of the outer CNT. CNT IV is a 200 nm DWNT with a 50 nm cut in the middle of the inner CNT. CNT V and CNT VI are 100 nm complete DWNTs. The chirality of inner tube is (6, 0) and chirality of outer tube is (12, 0) for DWNTs III to VI. The heat pulse is applied in the middle 10 slabs of the inner tube for CNT III and V and middle 10 slabs of the outer tube for CNT IV and VI.

In order to reduce the background noise and effectively analyze the interfacial energy transfer, the background temperature of CNTs is set at a low value (~0.01 K) and an intense heat pulse (~800 K) is applied using Brendsen thermostat. The major trends of interfacial energy transfer remain same at smaller temperature differences and by using different thermostats. Heat pulse method to study the role of specific phonon modes in thermal transport of SWNTs through MD simulations has been employed before [204, 205]. To illustrate the difference between the heat pulse propagation in SWNTs and DWNTs, simulations are first performed on SWNTs (CNT I and CNT II in Figure 5.1). Then, the heat pulse analysis is performed for two different configurations of DWNTs with a 50 nm cut in the middle (CNT III and CNT IV in Figure 5.1), and thermal energy transport between layers of DWNTs is investigated in the framework of travelling wave packets. These two configurations with cut in the middle help to avoid inter-layer energy transfer during the heating process, and focus on the inter-layer thermal transport by the travelling heat wave packets. Next, the heat pulse is applied to two complete DWNTs (CNT V and CNT VI in Figure 5.1) in order to analyze the inter-layer energy transport during the heating process for the comparison with two previous configurations with a cut in the middle.

5.1.2 MD Simulation Parameters and Procedures

The present MD simulations use the reactive empirical bond order (REBO) potential for C-C bond interaction and a truncated 12-6 type Lennard-Jones (LJ) potential for non-bonded van der Waals interactions between CNTs with fixed time step of 0.5 femtosecond (fs). Several different values of the energy and distance parameters in the LJ

potential are considered for the interaction of C-C atoms in the CNT. The present study employs the parameterization used by Zhong and Lukes, with ε =4.41 meV and σ =0.228 nm [49]. The details of the MD code used for the present analysis may be found in Reference [127]. For CNTs with finite length, the boundary conditions have a significant effect on the thermal transport. In present study, the two ends of the CNTs are set free, and the analysis is focused on the thermal transport before the heat pulses reach the ends. Simulations were also performed for CNTs with fixed ends, but no obvious difference was observed in the results before the heat pulses reach the ends.

The procedure of the MD simulation is as follows: first CNTs are quenched using Berendsen thermostat [206] to a very low temperature of 0.01 K for 900 000 time steps to 1100 000 time steps (450 ps - 550 ps) as required to achieve thermal equilibrium at 0.01 K. Then, a strong heat pulse with 0.9 ps duration and a peak temperature of 800K is applied to the ten slabs in the middle of the CNT of interest using the Berendsen thermostat. The heat pulse consists of a 0.1 ps rise time and a 0.8 ps duration with a constant temperature of 800 K. Finally, the CNTs are disconnected with the thermostat, and the system is kept at constant total energy for the rest of simulations.

5.1.3 Decomposition of Kinetic Energy in Cylindrical Coordinates

In order to investigate the contribution due to directional vibrations of atoms, kinetic energy corresponding to velocities in radial, tangential and longitudinal directions is calculated, denoted as radial component KE_r , tangential component KE_t , and longitudinal component KE_l . These three components are calculated using the radial,

tangential, and longitudinal velocities respectively, *e.g.*, $KE_r = \frac{1}{2}\sum_i^n m_i v_{i,r}^2$, where $v_{i,r}$ is the radial component of the velocity. Figure 5.2 shows the decomposition of velocity into three directions of the cylindrical coordinates for each atom in a ring of SWNT (6, 0).

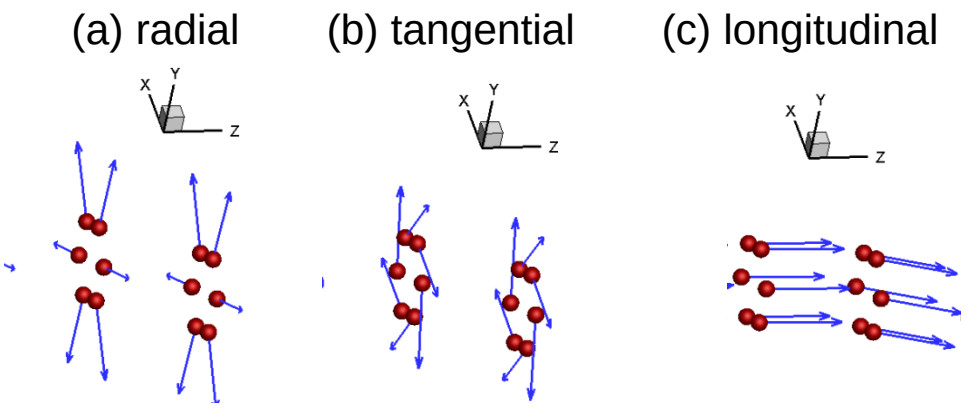

Figure 5.2 Velocity decomposition in cylindrical coordinates for an atom ring in a (6, 0) SWNT: (a) radial direction; (b) tangential direction; (c) longitudinal direction.

These components basically represent directional energy intensity in the corresponding direction. Besides, the kinetic energy of each slab is first time averaged over 200 time steps (0.1 ps) and then spatially averaged over ten slabs centered at the slab of interest to reduce the effect of statistical fluctuations. In order to examine the thermal transport along the CNTs, each CNT is divided in to 471 slabs per 100 nm along its axis. Each slab in (6, 0) and (12, 0) CNTs contains 12 and 24 atoms respectively. The z-direction axis is along the longitudinal direction of CNTs, and its origin is located at the middle of the CNTs. The origins of x axis and y axis are at the center of the cross section of CNTs.

5.1.4 Wavelet Analysis Method

Following the heat pulse analysis, the wavelet analysis is performed on all three velocity components of CNT atoms in order to analyze the evolution and propagation of different modes in the frequency space, which helps in illustrating phonon interactions between CNT layers. In particular, the acoustic phonon modes and radial breathing modes are of high interest to understand the thermal transport characteristics. The doubly degenerate transverse acoustic (TA) modes involve the tangential and radial vibrations, and the longitudinal acoustic modes are due to the vibrations along the tube axis. The twisting modes (TW) are related to the rigid rotation around the tube axis. The radial breathing modes (RBM) are associated with the radial vibrations and correspond to the out of plane tangential acoustic mode in graphene sheet. Analysis of the propagation and frequency spectrum of the directional components of kinetic energy can provide information about the phonon modes excited by the heat pulse.

The wavelet transform (WT) is an analysis tool well suited for the study of transient processes which occur over finite spatial and temporal domains [170]. A WT uses generalized local functions known as wavelets which can be stretched and translated with a desired resolution in both the frequency and time domains [207, 208]. Wavelets decompose a time series in the time-frequency space and are useful for identifying the evolution of dominant frequency modes with time. The WT of a signal ($s(t)$) is given as the convolution integral of $s(t)$ with ψ^*, where ψ^* is the complex conjugate of the mother wavelet function ψ,

$$W(b,a) = \frac{1}{a^{0.5}} \int \psi^* \left(\frac{t-b}{a} \right) s(t)\, dt \tag{5.1}$$

where a and b are parameters that control dilation and translation, respectively. The parameter a is also known as the scale in the wavelet analysis. The power spectrum of a WT is defined as $|W|^2$. In the present study, a Morlet wavelet is used as the mother wavelet which has the form of a plane wave with a Gaussian envelope and can be given by $\psi = e^{iwt} \times e^{-0.5|t|^2}$.

5.2 Spatiotemporal Heat Pulse Propagation and Energy Exchange

5.2.1. Heat Pulse Analysis of SWNTs

Heat pulse analysis is first performed on SWNTs of chiralities (6, 0) and (12, 0) which are denoted as CNT I and CNT II. Kinetic energy profiles along tube axis of CNT II after heating are shown in Figure 5.3. The characteristics of kinetic energy profiles of CNT I are similar to CNT II with differences only in magnitude. Kinetic energy profiles corresponding to three velocity components at different time instants along CNT II are shown in Figure 5.3. During the heating process, 143.5 eV is added into the CNT I, while 198.6 eV is added into CNT II. Comparing the kinetic energy for three velocity components, it can be observed that the heat pulse excites strong radial components for both CNT I and CNT II, but they diffuse slowly around the middle of the tubes.

Moreover, the magnitudes of radial components in CNT I are smaller than that in CNT II after heating, but their leading wave front propagate towards the end with similar speed. The diffusive characteristics of radial components can be attributed to the phonon modes related to the radial vibrations, *e.g.*, RBM and other high frequency optical phonons with smaller group velocity than the high speed LA and TW modes. The frequency spectrum of radial components shows that the leading wave fronts of the radial

components may mainly involve TA modes. Referring to the dispersion curves in Reference [140], the TA phonons have similar group velocity for CNTs with different diameters at small wave vectors, which may result in the similar propagation speed of the front radial components of CNT I and CNT II.

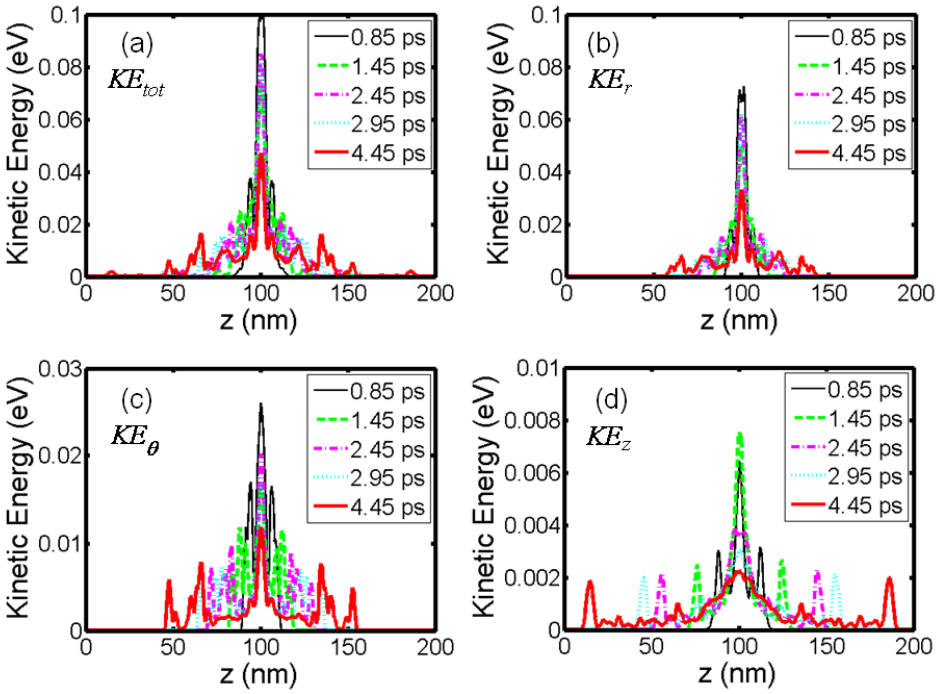

Figure 5.3 The location and shape of the heat pulse and kinetic energy corresponding to three velocity components at different time instants along CNT II: (a) Total kinetic energy (KE_{tot}); (b) Radial component (KE_r); (c) Tangential component (KE_θ); (d) Longitudinal component (KE_z).

As shown in Figure 5.3 (c), the heat pulse excites the tangential components with energy lower than radial components but higher than longitudinal components. The leading wave packets of tangential components propagate at the speed of about 13.1 km/s and 11.9 km/s in CNT I and CNT II respectively, and can effectively spread energy along

the tubes. This propagation speed falls into the speed range (11~15 km/s) of TW phonons [204, 205]. Reference [205] showed some high energy wave packets associated with second sound waves with similar speed (12.2~12.9 km/s). But further observation of the atom vibrations shows the rigid rotation around the tube axis and tube deflection during the heating process. Thus, the leading wave packets of the tangential components should be mainly contributed by TW and TA phonons excited by the heat pulse. The longitudinal components excited by the heat pulse are relatively small, but they propagate very fast along the tube with a speed of 20.9 km/s and 20.2 km/s in CNT I and CNT II respectively, Figure 5.3 (d). This speed is in good agreement with speed of the sound waves associated with the longitudinal phonon modes (19.9 km/s to 21.7 km/s) in Reference [205]. By comparing Figure 5.3 (a) with (d), it is found that the leading wave packets in the total kinetic energy profiles are only contributed by this high speed longitudinal component.

5.2.2 Heat Pulse Analysis of DWNTs with Cut in the Middle

In this section, heat pulse analysis is performed on two DWNTs, one of which has 50 nm cut in the outer layer (CNT III) and the other one has 50 nm cut in the inner layer (CNT IV), Figure 5.1. These two configurations have been chosen to avoid the inter-layer energy transfer during the heating process at the middle of the tube and thus focus on the inter-layer thermal transport due to the interaction of propagating heat wave-packets of high speed, *e.g.,* tangential components and longitudinal components as indicated in CNT I and CNT II.

When the heat pulse is applied to the DWNTs with cut in the middle, 220.7 eV and 381.8 eV are added into CNT III and CNT IV respectively. This energy is much higher than the energy added into the SWNTs (CNT I and CNT II). This is because some strong tangential components are excited by the heat pulse, as shown in Figure 5.4 (d). Figure 5.4 (a) and (b) show the energy transfer between the heated and unheated tubes after the heating. Till the heat wave packets reached the end of the CNTs (4.5 ps), 6.8 eV is transferred from inner tube to outer tube in CNT III, while a maximum of 4.9 eV is transferred from outer tube to inner tubes in CNT IV in 3.0 ps, Figure 5.4. Comparing this energy transfer with the energy gained by the heated tube, it is observed that the energy transfer between the heated tube and unheated tubes is very inefficient.

Moreover, the energy transfer in CNT III from inner to outer tubes starts a little earlier than that in CNT IV from outer to inner tube because the leading wave packets (longitudinal waves) propagate a little faster in CNT III, as indicated by CNT I (20.9 km/s) and CNT II (20.2 km/s). From Figure 5.4, it can be also observed that the energy transfer from the heated tube to unheated tube in CNT III increases monotonically until the heat wave packets reach the end of the tube. However, the energy transfer in CNT IV reaches the maximum at 3 ps after which energy is transferred back and forth between the heated and unheated tubes. This can be also attributed to the slight difference in speed of longitudinal components: the faster propagating longitudinal components excited in the inner tube of CNT IV (corresponding to CNT I at 20.9 km/s) at beginning may interfere with the slower propagating longitudinal components of the outer heated tube (corresponding to CNT II at 20.2 km/s), and thereby counteracting further energy transfer across the interface.

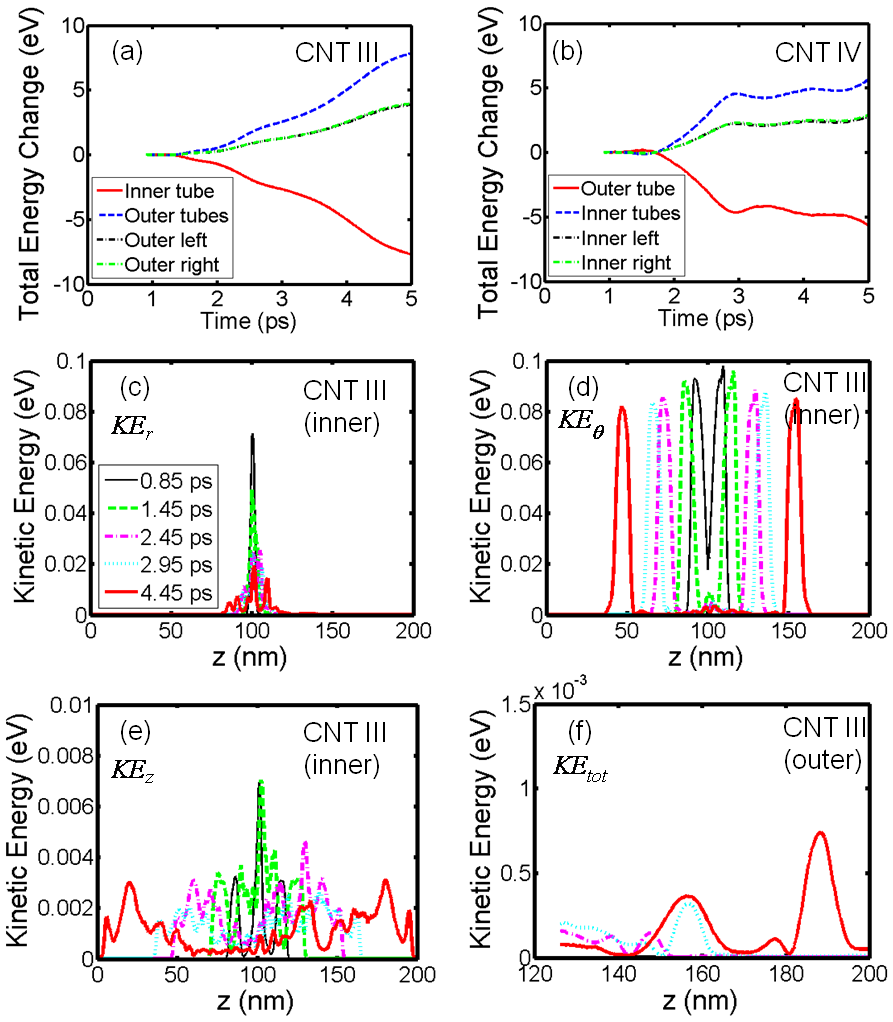

Figure 5.4 Total energy variation as a function of time with reference to total energy at t=0.9 ps for (a) CNT III and (b) CNT IV. The heating process is completed at 0.9 ps. The location and shape of the heat pulse and kinetic energy corresponding to three velocity components at different time instants of CNT III: (c) Radial component (KE_r) of heated (inner) tube; (d) Tangential component (KE_θ) of heated (inner) tube; (e) Longitudinal component (KE_z) of heated (inner) tube; (f) Total kinetic energy (KE_{tot}) profiles along unheated (outer) tube. (d)~(f) shares the same legend with (c).

In comparison to SWNTs (see Figure 5.3 (b)), the heat pulse also excites strong radial components in CNT III and CNT IV, but the radial components of CNTs III and IV (see Figure 5.4 (c)) diffuse more slowly during the simulation period of 4.45 ps and are confined in the middle 50 nm. The magnitude of radial components in CNT III is smaller than that in CNT IV. Observations of atom vibrations of CNT III and CNT IV do not show any deflection perpendicular to the tube axis which is related to TA phonons. The absence of TA phonon can be also confirmed by the absence of low frequency portion in frequency spectrum of radial velocity. So the absence of TA phonons can lead to the lower propagation speed of radial components of CNT III and CNT IV.

Moreover, unlike the SWNTs, the excited tangential components are much stronger and carried the largest part of the kinetic energy. As shown in Figure 5.4 (d), the tangential components propagate with a speed of 12.5 km/s which is approximately equal to the tangential wave speed in SWNTs (CNT I and CNT II). Since the TA phonons may not be present for CNT III and CNT IV, the strong leading wave packets of tangential components are mainly contributed by TW phonons. The longitudinal components excited by the heat pulse in CNT III and CNT IV have little difference with CNT I and CNT II in terms of both magnitude and propagation speed, Figure 5.4 (e).

The kinetic energy in the unheated tubes is very small in comparison with kinetic energy in the heated tubes, Figure 5.4 (f). The kinetic temperature corresponding to the radial component and the tangential component in the unheated tubes are approximately close to the background temperature (0.01K), and the longitudinal component is nearly equal to the total kinetic energy. It indicates that only longitudinal modes are excited in the unheated tubes during the energy transfer process, which might be the reason for the

inefficient energy transfer between the tubes. This will be further discussed in the following wavelet analysis.

5.2.3 Heat Pulse Analysis of Complete DWNTs

As shown in the above heat pulse analysis for CNT III and CNT IV, the radial components diffuse slowly in the middle of the CNTs, and it does not reach the other layer region during the simulation period. Thus, in order to investigate the energy transfer through these slowly diffusing radial components, heat pulse analysis is performed on the complete DWNTs. The heat pulse is applied in the middle of the inner layer and outer layer of CNT V and CNT VI respectively.

As shown in Figure 5.5 (a) and (b), the energies gained by the CNT V and CNT VI during the heating (0.9 ps) are 197.0 eV and 303.8 eV respectively. Out of this total gained energy during the first 0.9 ps, 195.7 eV and 291.2 eV were directly gained by the heated tubes of CNT V and CNT VI, and 1.3 eV and 12.6 eV were transferred to the unheated tubes respectively. It indicates that the energy transfer from inner tube to outer tube for CNT V during the heating period is negligible. Moreover, the energy transfer to the unheated tube is still very low during the first 0.5 ps, and it increases dramatically after 0.5 ps. The abrupt increase of energy transfer occurs again at 0.9 ps when the heating process ends. After the heating process, the energy transfer to the unheated tube of CNT V is also much smaller than that of CNT VI.

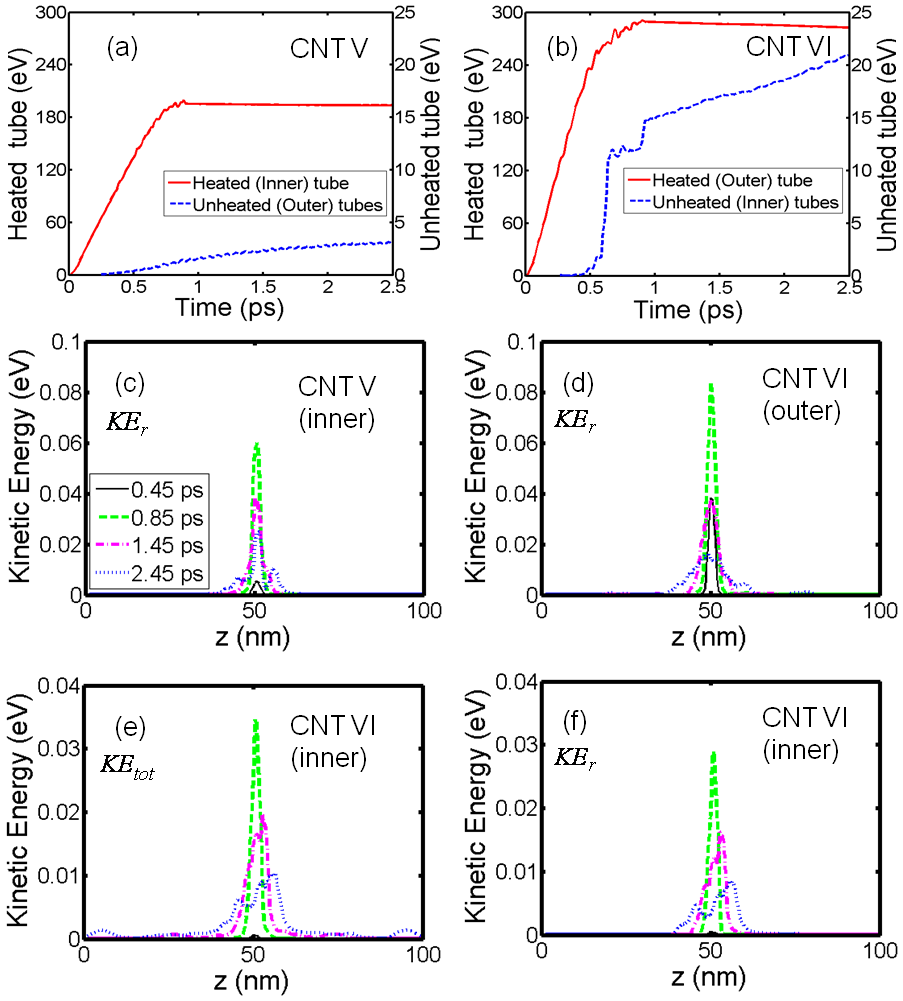

Figure 5.5 Total energy variation as a function of time with reference to total energy at t=0.9 ps for (a) CNT V and (b) CNT VI. The heating process is completed at 0.9 ps. The location and shape of the heat pulse and kinetic energy corresponding to three velocity components at different time instants of CNT V and CNT VI: (c) Radial component (KE_r) of heated (inner) tube of CNT V; (d) Radial component (KE_r) of heated (outer) tube of CNT VI; (e) Total kinetic energy (KE_{tot}) profiles of unheated (inner) tube of CNT VI; (f) Radial component (KE_r) of unheated tube (inner) of CNT VI. (d)~(f) shares the same legend with (c).

The energy transfer between CNTs is dependent on the distribution of energy in different phonon modes. The excitation of radial phonon modes exhibit strong dependency on the CNT diameter, *i.e.*, under the applied heat pulse CNTs with different diameters may excite different distribution of radial phonon modes that participate differently in transmitting energy. The radial breathing modes of outer tube of CNT VI have a lower frequency than that of the inner tube of CNT V. So, a larger population of radial breathing modes and other radial modes may be excited by the short heat pulse in the outer tube of CNT VI which effectively transfers heat to inner CNT in comparison to the case V (~ energy transfer from inner to outer tube). As shown in Figure 5.5 (d), the radial components of CNT VI are small before 0.5 ps. After 0.5 ps, the peak of radial components has increased up to 0.07 eV which lead to large energy transfer to the unheated tube as shown in Figure 5.5 (b) and (e). However, at 0.55 ps, the peak of radial components of CNT V has kinetic energy below 0.02 eV which is much smaller than 0.07 eV of CNT VI. During the entire heating process (0.9 ps), the peak of radial components of CNT V is below 0.06 eV and energy transfer to other tube is also low. Therefore, the larger magnitude of radial components of CNT VI indicates more radial modes are excited, and leads to the large energy transfer in CNT VI.

Besides, before 0.5 ps, most of the energy goes to the tangential components, and generates strong leading wave packets involving twisting acoustic modes. As demonstrated by the simulation of CNT III and CNT IV, these strong leading wave packets do not transmit energy efficiently. So before 0.5 ps, there is little energy transferred to the unheated tube for CNT VI.

From Figure 5.5 (f), it can be observed that the radial components are dominant in unheated tubes of CNT VI, and have similar profiles as the radial components in the heated tubes (Figure 5.5 (d)). This indicates that the radial components in the unheated tubes are excited by the corresponding radial components in the heated tube during the heating process, leading to large energy exchange. However, this cannot happen to DWNTs with cut in the middle (CNT IV) because the radial components only diffuse slowly in the middle of the heated tube and cannot reach the unheated tubes. Moreover, the tangential components and longitudinal components in the unheated tubes of CNT VI also gain a higher amount of energy (with magnitudes below 0.004 eV) than CNT III and CNT IV, but they are much smaller than the radial components. Diffusion like behavior in the middle of the CNTs is found for the three components of both CNT V and CNT VI. CNT III and CNT IV have shown ineffective interfacial energy transmitting by the strong tangential components and weak longitudinal components excited by the heat pulse in the heated tube. So the tangential and longitudinal components in unheated tube of CNT V and CNT VI are excited by the radial components in the heated tube.

5.3 Wavelet Analysis of Energy Spectrum

The power spectrum of the three velocity components of each atom in the nanotube is computed using the wavelet transform (WT). By summing the power spectrum over all the atoms of a slab, a one-dimensional projection of the temporal spectra along the nanotube axis is calculated. In this way, temporally evolving spectra of the three velocity components for the entire spatiotemporal field are obtained.

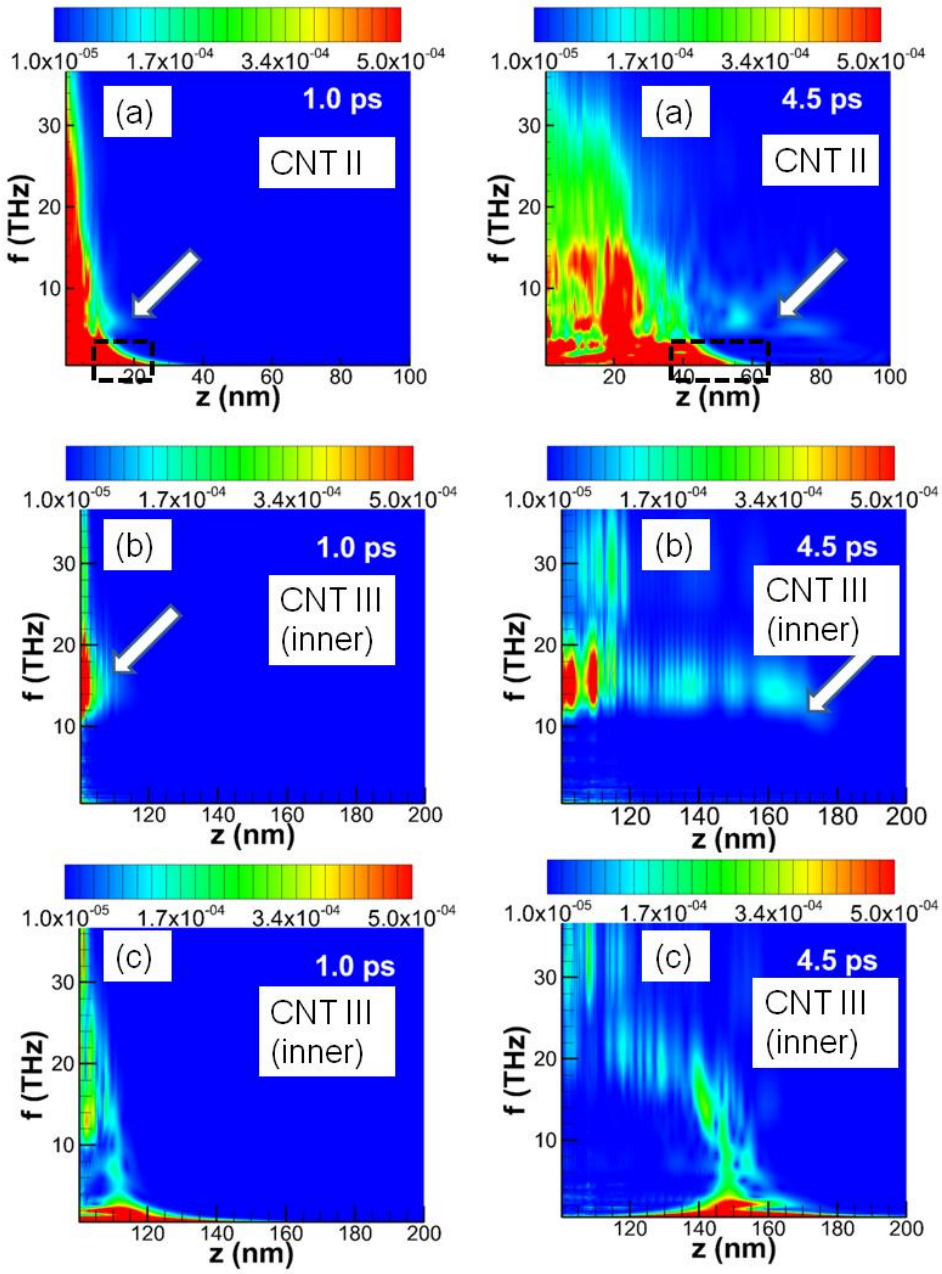

Figure 5.6 Frequency spectrum along the right half of the heated tubes of CNT II and CNT III at different time instants: (a) Radial component of CNT II; (b) Radial component of heated tube of CNT III; (c) Tangential component of heated tube of CNT III.

As discussed in the heat pulse analysis of CNT I and CNT II, the leading radial components may be mainly composed of TA and RBM phonon modes. Figure 5.6 (a)

shows the frequency spectrum along the right half of the heated tubes of CNT II at different time instants. It can be clearly observed that the leading radial components contain two frequency regions: the low frequency region with high power intensity (marked by dashed rectangular) and the high frequency region with low power intensity (marked by white arrow). The low frequency modes have smaller group velocity than LA and TW modes, and may be composed of TA modes. The high frequency modes are centered at 8 THz which is same as the fast moving radial modes of heated tube of CNT VI (see Figure 5.8 (a)). This frequency is one half of the corresponding fast moving mode frequency (16 THz) of CNT III in Figure 5.6 (b). This is understandable because CNT II and the heated tube of CNT VI has a chirality of (12, 0), and its diameter is twice of the (6, 0) heated tube of CNT III. Reference [209] shows the inverse dependence of the RBM frequency *f* on the tube diameter *D, i.e., f~1/D*. So the fast moving radial modes at high frequency are mainly contributed by RBM phonons [209].

Besides, frequency spectrum of radial components also shows much high frequency modes with high power intensity and smaller velocity, and they may be composed of optical phonon modes related to radial vibrations. As shown in Figure 5.6 (b), the radial components of heated tube of CNT III are only composed of high frequency phonon modes (greater than 10 THz). The absence of low frequency modes (compared to Figure 5.6 (a)) indicates the TA modes are not excited by the heat pulse. This may be because the deflections of inner/outer tube perpendicular the tube axis are restricted by the outer/inner tube for DWNTs (CNT III - CNT VI). Moreover, these high frequency radial components with high power intensity mainly diffuse in the middle, which is consistent with the heat pulse profiles shown in Figure 5.4. As discussed in the

heat pulse analysis of CNT III and IV, the leading wave packets of tangential components are mainly composed of TW modes. Figure 5.6 (c) shows that these TW modes are concentrated in the low frequency region with a high propagating speed (see Figure 5.4 (d)).

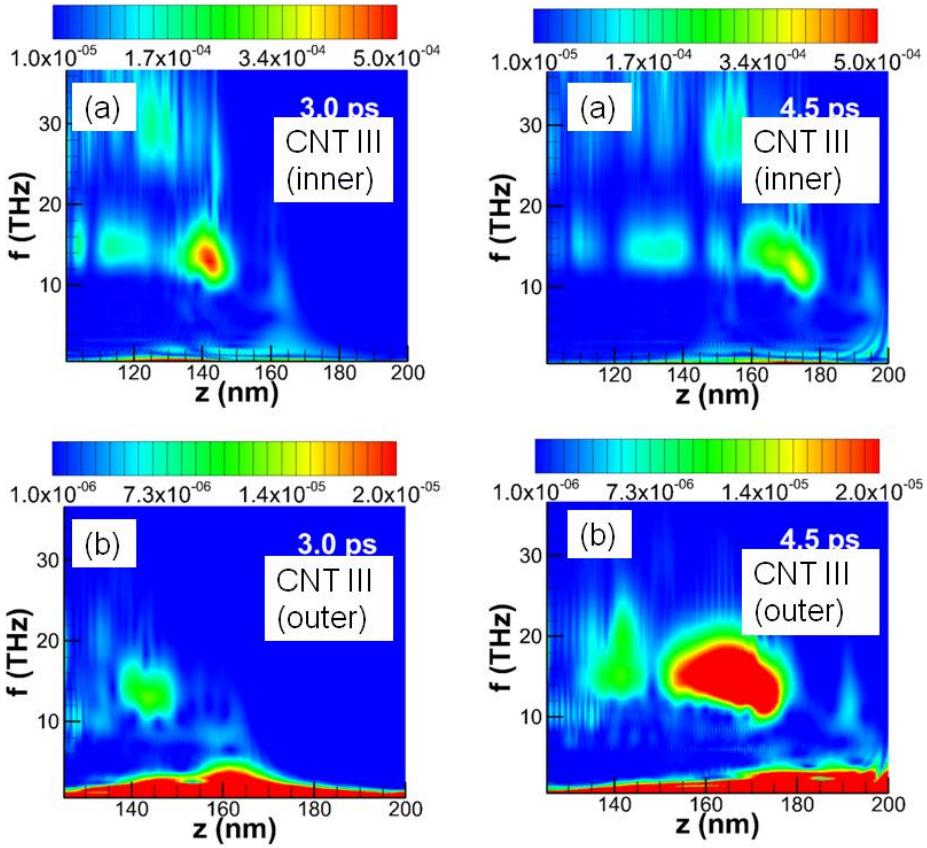

Figure 5.7 Frequency spectrum longitudinal velocity of CNT III at different time instants: (a) Longitudinal component of heated tube; (b) Longitudinal velocity of unheated tube.

Comparing Figure 5.7 (a) with (b), it can be seen that the frequency and propagation of the longitudinal components in the unheated tubes match well with the frequency and propagation of the longitudinal components in the heated tube. This

indicates that the longitudinal components in the unheated tubes may be excited by the corresponding longitudinal components in the heated tube. Together with the former discussion about heat pulse profiles in Figure 5.4, it can be concluded that the energy transfer between the tubes in CNT III and CNT IV is achieved by the longitudinal components. As mentioned previously, the kinetic temperature corresponding to the tangential components and radial components in the unheated tubes of CNT III and CNT IV are equal to the background temperature (0.01K); this is further confirmed by the wavelet analysis showing that the tangential and radial components are not excited in unheated tube. Although the leading wave packets of tangential components have high energy intensity (Figure 5.4 (d) and Figure 5.6 (c)) in the heated tube, they do not excite any phonon modes in unheated tubes as they propagate.

As discussed in the previous section, the enhancement of the energy transfer between tubes in CNT VI may result from the radial components. This can be further supported by the frequency spectrum in Figure 5.8. The frequency spectrums of the radial velocity of the heated tube and the unheated tubes in CNT VI are shown in Figure 5.8 (a) and (b). As shown in Figure 5.8 (a), the radial components are mainly composed of high frequency modes, which is similar to CNT III in Figure 5.6 (b). The fast moving modes of the radial component, the regions marked by the white arrows, is only a small portion at the frequency of about 8 THz, one half of the corresponding fast moving mode frequency (16 THz) of CNT III in Figure 5.6 (b). As discussed above, the fast moving modes of radial components are attributed to RBM phonons. Figure 5.5 (c) and (d) show that the energy intensity of these fast moving radial modes is very small. By comparing Figures 7 (a) and (b) and Figure 5.5 (f), it can be observed that the fast moving radial

modes in heated tube does not excite the corresponding part in the unheated tube. This can be attributed to their low energy intensity as well as the spectral mismatching between tubes with different diameters. On the contrary, the slow diffusing modes are excited in the unheated tube of CNT VI with similar frequency range of the slow diffusing modes in heated tube, Figure 5.8 (a) and (b). Thus, the slow diffusing radial components in the unheated tubes are excited by the slow diffusing radial components in the heated tube of CNT VI, considering that strong coupling and larger energy transfer can be expected between low speed phonon modes of similar frequencies.

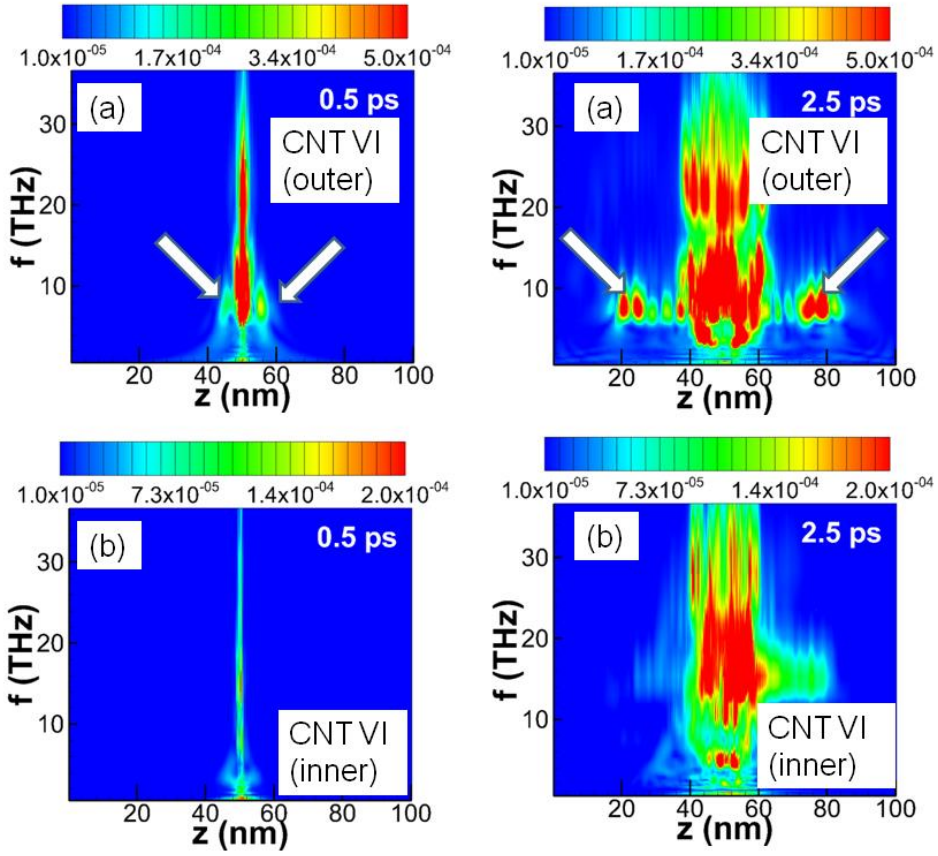

Figure 5.8 Frequency spectrum of the radial velocity of CNT VI at different time instants: (a) heated (outer) tube; (b) unheated (inner) tube.

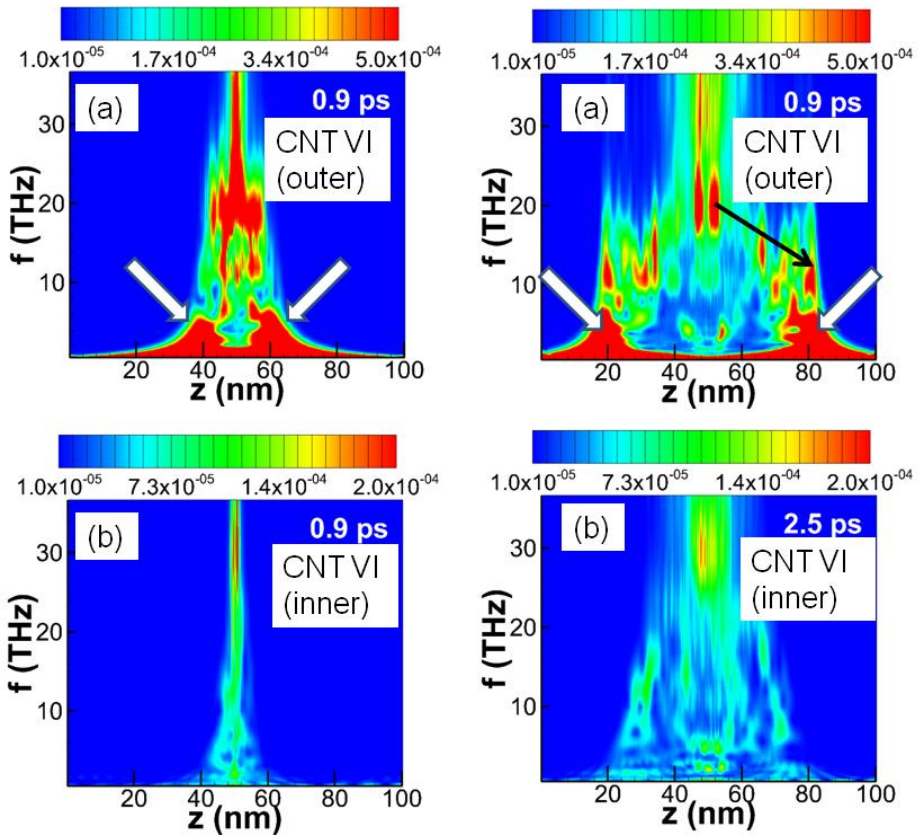

Figure 5.9 Frequency spectrum tangential velocity of CNT VI at different time instants: (a) heated (outer) tube; (b) unheated (inner) tube.

The tangential components of the heated tube have a different spectrum in comparison to the radial component, as shown in Figure 5.9 (a). The fast moving and low frequency tangential modes have very high intensity in the frequency spectrum of the tangential components. The evolution from high frequency modes to the low frequency modes can be also observed, as shown by the black arrow in Figure 5.9 (a). However, the fast moving and low frequency modes are not excited in the unheated tubes as shown in Figure 5.9 (b). Figure 5.9 (b) also shows that the tangential velocity spectrum of the unheated tube mainly consists of the high frequency modes, and the low frequency

spectrum is relatively weak. This indicates that typically high velocity phonon modes are inefficient in energy transfer.

5.4 Closure

In summary, this chapter investigates the heat pulse propagation in both SWNTs and DWNTs using MD and wavelet methods with a focus to analyze thermal coupling between the layers of DWNTS. In SWNTs, the strong radial components excited by the heat pulse only diffuse around the middle of the tube; longitudinal components have the least energy content but they propagate effectively along the tubes with a speed of LA phonon modes. In DWNTs, strong tangential components are excited by the heat pulse, and can propagate effectively along the tubes with the propagation speed similar to the TW acoustic phonon modes. However, these fast moving tangential components are very ineffective in energy transfer between the tubes. The heat pulse and wavelet analysis show that the longitudinal components gain only a small part of the energy during the heating process and hence are not effective in energy exchange between tubes. A large energy transfer is observed from outer tube to inner tube of a DWNT without any cut during the heating period; the transferred energy is primarily contained in the radial modes which show that energy can be transferred effectively by the radial modes. A detailed study is further required to explore the coupling of specific phonon modes between the layers of MWNTs.

CHAPTER 6

MOLECULAR DYNAMICS SIMULATIONS OF THERMAL CONDUCTIVITY OF GRAPHENE SUPPORTED ON METAL SUBSTRATE

Although the thermal conductivity of suspended single layer graphene (SLG) was measured to be as high as 3000 ~ 5300 W/mK [66, 67], the graphene-substrate interactions can significantly reduce the thermal conductivity of the supported SLG [70] and the supported few-layer graphene [210]. The thermal conductivity of SLG supported on SiO_2 was measured as 600 W/m/K at room temperature, which is much lower than the suspended SLG [70]. As graphene will be either supported or embedded in most of the applications such as field effect transistors or interconnects, the contact with metals is extremely important and unavoidable in the graphene based nanoelectronics. An investigation of the thermal conductivity of graphene supported on metals is crucial, *e.g.*, Cu in graphene/Cu hybrid interconnects [211]. The study on the phonon mode contribution to the thermal conductivity of graphene is of fundamental importance to understand its thermal transport mechanism. However, the outcomes of previous studies using BTE models [71, 146, 147, 152, 161] is still controversial in the context of contribution of different phonon modes to thermal conductivity, *e.g.*, the contribution of ZA phonon modes. The MD simulations can serve as an important supplement to the previous studies as it can consider atomistic structure at the interface and multi-phonon scattering is naturally included.

This chapter presents the investigation of the thermal transport in suspended SLG and SLG supported on Cu using molecular dynamics and relaxation time approximation

(RTA) approach at room temperature (~300 K). The equilibrium molecular dynamics (EMD) simulations and Green-Kubo method are employed in order to reduce the finite size and boundary effects that are concerns of non-equilibrium molecular dynamics (NEMD) simulations. The lifetime of each phonon mode is obtained by fitting the spectral energy density (SED) to the Lorentzian function, and the corresponding contribution to thermal conductivity is determined using the RTA approach.

6.1 Simulation Setup and Parameters

In the MD simulation, the most stable configuration of graphene on the Cu substrate [76, 212] is used. As shown in Figure 6.1, the SLG honeycomb lattice is positioned to match the triangular lattice of Cu (111) surfaces with one carbon atom on top of a Cu atom (A site) and the second carbon on a hollow site. Since, the Cu substrate is usually much thicker than the SLG, the lattice constant of SLG will tend to match Cu [212]. Therefore, the experimentally measured FCC lattice constant of copper (3.61 Å) is used, and the lattice constant of SLG is adapted correspondingly. The lattice constant of SLG is increased by 2.4% (compared to 2.492 Å calculated using the optimized Tersoff potential [145]) to match the Cu lattice. The dimension of the Cu substrate used in the simulation is 60 Å × 60 Å × 12.5 Å.

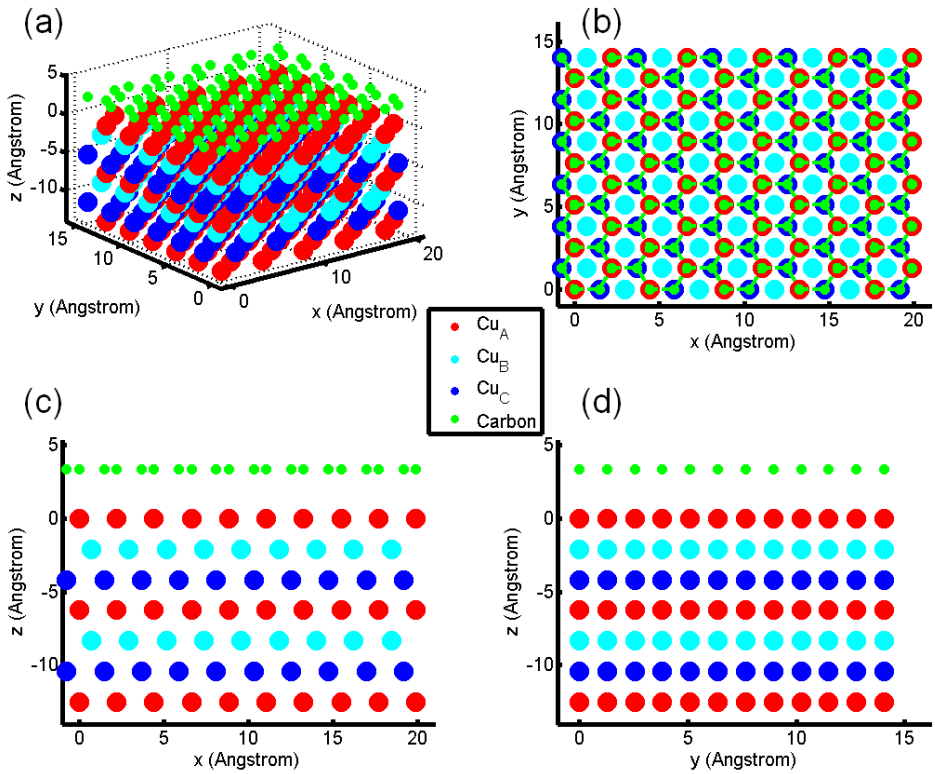

Figure 6.1 Schematic diagram of the single layer graphene and Cu-111 system. (a) 3D view; (b) x-y plane; (c) x-z plane; (d) y-z plane. (a)~(d) share the same legend.

The MD simulations are implemented using Lammps package [191]. The optimized Tersoff potential [145] and embedded-atom method (EAM) potential [213] are used to describe the C-C interactions and Cu-Cu interactions, respectively. The optimized Tersoff potential can give improved fits to the three acoustic phonon branches of graphene dispersion curve which play the most important role in the thermal transport in SLG. The van der Waals interaction between C-Cu atoms at the interface was modeled by Lennard-Jones (L-J) potential,

$$V_{ij}(r) = 4\chi\varepsilon_{ij}\left[\left(\sigma_{ij}/r\right)^{12} - \left(\sigma_{ij}/r\right)^{6}\right] \tag{6.1}$$

The present study employs the L-J parameterization used by Xu and Buehler [46], with

ε=25.78 meV and σ=3.0825 Å. The parameter χ is used to adapt the interaction strength between C and Cu atoms [195]. A time step of 0.5 fs is used in all the simulations.

6.2 Validation of Simulation Parameters

Parameter set of Tersoff potential optimized by Lindsay and Broido [145] is employed to describe the interatomic interactions in graphene. This parameter set can provide improved fits to the lattice constant and to the acoustic phonon velocities for graphite as shown in Figure 6.2.

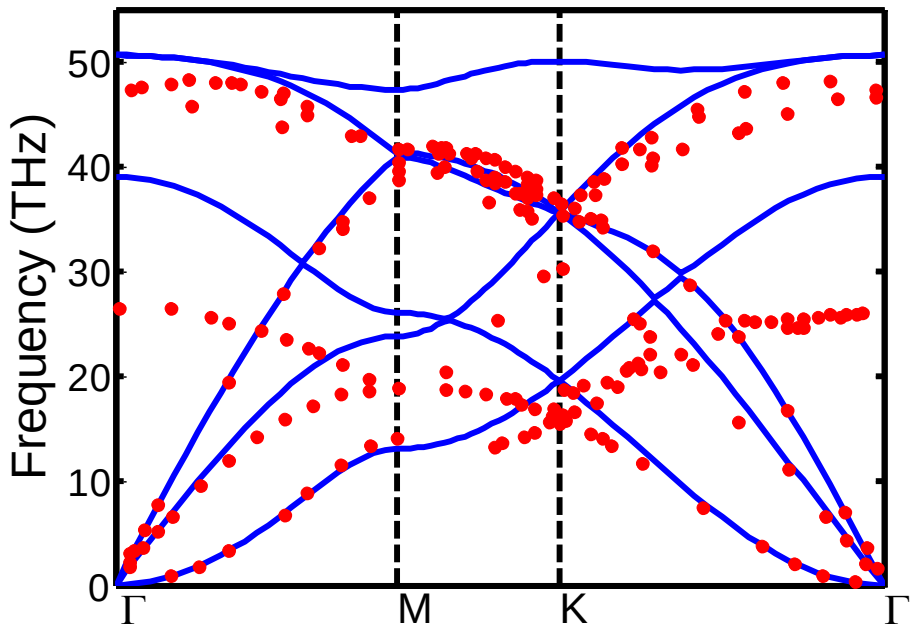

Figure 6.2 Phonon dispersion of graphene along high-symmetry directions obtained using optimized Tersoff potential (solid blue lines) [145]. The solid dots are in-plane experimental data points for graphite from Ref. [214, 215].

The parameter set of EAM potential for Cu is determined empirically by fitting to a series of properties including sublimation energy, equilibrium lattice constant, elastic constants, and vacancy-formation energies [213]. Although the electron transport is

absent in MD simulations of metal, the EAM potential can yield a phonon dispersion in good agreement with experiment [216].

The parameters of L-J potential for C-Cu interactions are obtained from Ref. [46] in which the parameters are calculated using mixing rule from parameters for graphite and face-centered cubic copper. Graphene has strong interaction and bonding with some metals such as Ti or Ni, but weakly interact with Cu [76]. At graphene/Cu interfaces, the van der Waals interactions can be well described by L-J potential for Cu-C interaction.

6.3 Thermal Conductivity of Isolated Single Layer Graphene

The thermal conductivity of isolated SLG is computed using Green-Kubo method described in the previous section. In order to achieve a good ergodicity of the phonon phase space, four independent simulations are performed for each case using different initial velocities of atoms following Gaussian distribution. The computed thermal conductivity of the isolated SLG is shown in Figure 6.3. As shown in Figure 6.3, a good convergence can be achieved by averaging over just four independent simulations. The thermal conductivity is obtained by averaging over a smooth region once the integral of heat flux autocorrelation function converges to constant values (red solid circles in Figure 6.3) [217].

Non-equilibrium molecular dynamic (NEMD) simulations uses heat source and sink which brings the size effect in the thermal conductivity calculations. The size effect in Green-Kubo method is much less severe than that in NEMD [116] as periodic boundaries are employed. However, the size effects still play a role in Green-Kubo method as for a system with very small size all long-wavelength phonon modes may not

get excited which may have important contribution to phonon thermal conductivity [68, 133, 154, 160, 178].

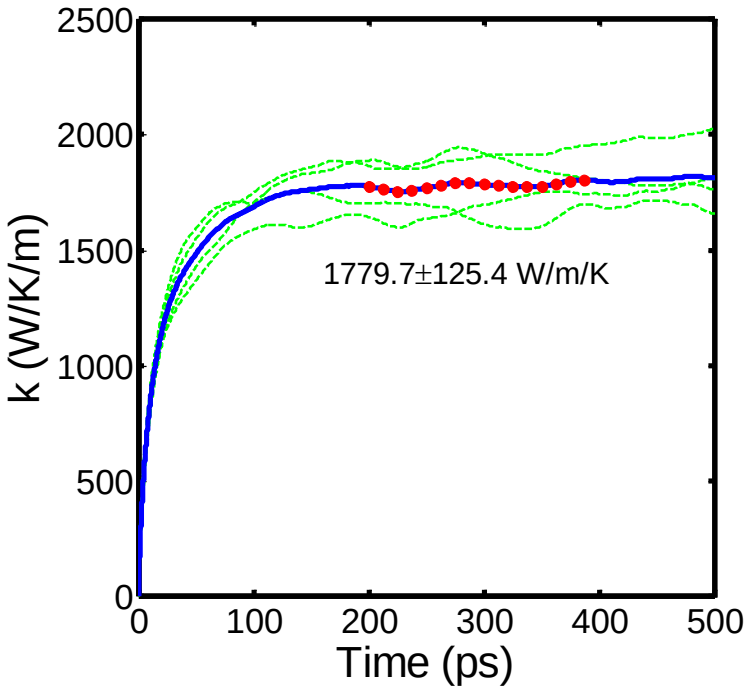

Figure 6.3 Thermal conductivity of isolated SLG of size 60 × 60 Å obtained from the integral of heat flux autocorrelation function. The blue solid line is the average of four independent simulations (green dotted lines). The thermal conductivity is obtained by averaging the region marked by red solid circles, and the standard deviation is calculated based on the four independent simulations.

The calculations using Green-Kubo method also indicate size dependent thermal conductivity of SLG. The thermal conductivity of 30 × 30 Å SLG is estimated as 2520 W/mK, which is close to the thermal conductivity obtained from MD simulations in previous studies on the SLG of similar size [68, 218]. The thermal conductivity is observed to decrease with increasing simulation domain of SLG when the size is small.

This trend is just opposite to what is typically observed for graphene nano-ribbon or systems with fixed boundaries in NEMD simulations. In the Green-Kubo calculation of the SLG with periodic boundary condition, phonons may pass the system several times without scattering [178], which is particularly more frequent for the small systems. In the absence of external scattering mechanism (*e.g.*, defect scattering, impurity scattering, and boundary scattering), only few three-phonon U-process exists for long wave length phonons. The number of excited phonon modes may be limited for the MD simulation with a small domain, and some long wave length phonons (phonons with wave length comparable to the system size) encounter few scattering event and travel ballistically, resulting in a large artificial thermal conductivity [154]. More phonon modes are excited with increasing system size but phonon-phonon scattering also increases [133]. Because of this trade-off, the thermal conductivity values saturate once the size of SLG approaches 200 × 200 Å.

However, the effect of decreasing SLG size on its thermal conductivity significantly reduces once SLG become larger than 60 × 60 Å. The computation is much more expensive for SLG supported on Cu (111) substrate due to the presence of thick Cu substrate. The SLG of 60 × 60 Å size is selected for the simulations of Cu supported SLG considering the trade-off between the eliminating size effect and reducing computational efforts. The modified Tersoff potential parameters are used for all MD simulations. The original Tersoff parameters [121] are also tested using Green-Kubo method which gives a much smaller thermal conductivity of 541 W/mK for the 60 × 60 Å SLG compared to 1779.7 W/mK given by the modified Tersoff potential parameters. The standard deviation as indicated in Figure 6.3 is 125.4 W/mK which is calculated based on the four

independent simulations.

6.4 Thermal Conductivity of Supported Single Layer Graphene

Large oscillations in the HCACF occur when atoms of different atomic masses are present at the interface which makes evaluation of the HCACF integral relatively difficult. To address these oscillations and convergence issues for supported SLG, the approach followed in Reference [180] is employed which neglects the convection term in the heat flux calculations. Large oscillations in the HCACF can be eliminated using this method as shown in Figure 6.4 (a). The convection term is also neglected for the isolated SLG. Only a small deviation in thermal conductivity is observed by neglecting convection term, *e.g.*, less than 6% for isolated SLG of size 60 × 60 Å.

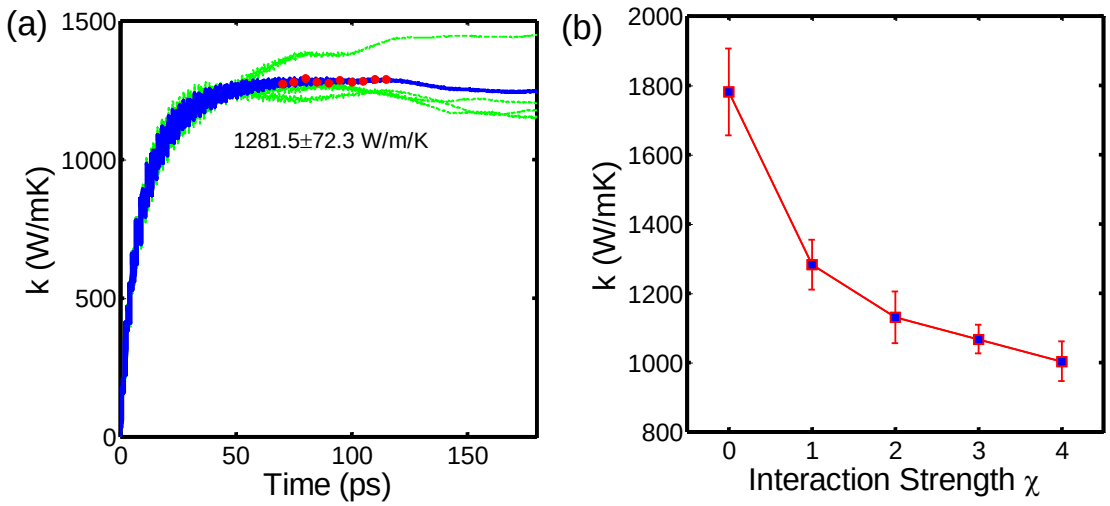

Figure 6.4 (a) Thermal conductivity obtained from the integral of heat flux autocorrelation function of Cu-supported SLG (60 × 60 Å). The blue solid line is the average of four independent simulations (green dotted lines). The thermal conductivity is obtained by averaging the region marked by red solid circles; (b) Variations of thermal conductivity with the L-J interaction strength factor χ between C and Cu atoms. The error

bars indicate the standard deviations from four independent MD simulations for each case.

By comparing Figure 6.3 (a) and Figure 6.4 (a), it can be observed that the integral of HCACF converges faster for the supported SLG than the isolated SLG. This indicates that the lifetime of certain phonon modes is shortened due to the scattering with substrate, and the corresponding contribution to HCACF and thermal conductivity is suppressed.

By varying the interaction strength factor χ in the L-J potential, the effects of C-Cu coupling strength on the thermal conductivity are investigated. As shown in Figure 6.4 (b), the point at χ=0 corresponds to the isolated SLG. The interactions with substrate result in 28% reduction of the SLG thermal conductivity using standard L-J parameters (χ=1) for the SLG-Cu (111) system. Thermal conductivity of SLG further reduces with increasing χ, but the rate of decrease slows down. A further reduction of 16% is observed (~total 44%) when the interaction strength factor χ is increased from 1 to 4. This reduction in thermal conductivity is smaller than the recent experimental results on graphene supported on SiO_2 substrate [70]. This may be due to two reasons: 1) the relatively smooth Cu (111) surface leads to less interface scattering of phonons; 2) neglect of quantum effects and the deviation of phonon distribution by the classical MD simulations. To further understand this, the contribution of different phonon modes to the thermal transport in SLG is determined using RTA method and the effects of thermal interactions at SLG-Cu interface are discussed.

6.5 Thermal Contribution of Different Phonon Modes

Some recent studies investigate the thermal transport in the SLG and multi-layer graphene using BTE based methods. The contribution from different phonon modes has been presented and the importance of appropriately considering the selection rules have been demonstrated [152, 156]. However, the role of phonon modes in the thermal transport of SLG supported on Cu substrate has not yet been quantitatively studied. In this section, the dispersion relations and phonon lifetime are predicted by means of spectral energy density (SED) using the velocities from equilibrium MD simulations, and then the contribution of different phonon modes to thermal conductivity is calculated using RTA method.

Figure 6.5 shows the dispersion curves of isolated SLG and Cu supported SLG, which is estimated from the contour plot of the sum of SED, $\Phi(q,\omega,s)$, of each mode. The $\Phi(q,\omega,s)$ is averaged over 20 independent simulations to mitigate the inherent fluctuation in MD simulation results. The black solid lines in Figure 6.5 (a) correspond to dispersion curves made by connecting the peaks of SED of each mode. By comparing Figure 6.5 (a) and (b), it can be observed that the substrate interactions do not have an obvious effect on the LA, TA and the three optical phonon modes. However, the ZA modes have been significantly changed due to the substrate interactions. Several modes related to out-of-plane vibrations appear at the low frequency and small wave vector region (~ dimensionless wave vector $q^* = q/q_M$ < 0.5), as marked by the yellow dashed rectangle and the inset in Figure 6.5 (b). These modes with non-zero frequency at Γ point are similar to the layer-breathing mode in bilayer graphene and graphite [150]. They correspond to the out-of-phase vibration of C-Cu atom pair in direction perpendicular to

graphene-Cu interface.

Reference [219] and [95] suggested that there exist a cut-off frequency below which the coupling with the substrate phonons and cross-plane phonons becomes strong in the supported SLG or graphite. As a result, the phonon energy leaks to the substrate and the contributions of these low frequency phonons to the in-plane thermal transport are reduced to negligible. The blurred region in Figure 6.5 (b) indicates a cut-off frequency of 6 THz for the ZA phonon modes in SLG supported on Cu. Since the ZA phonons have a maximum frequency of 14 THz at M point, this cut-off frequency has covered ZA phonon modes with $q^* \leq 0.5$, i.e., 50% of the allowed ZA phonon modes in Γ-M direction.

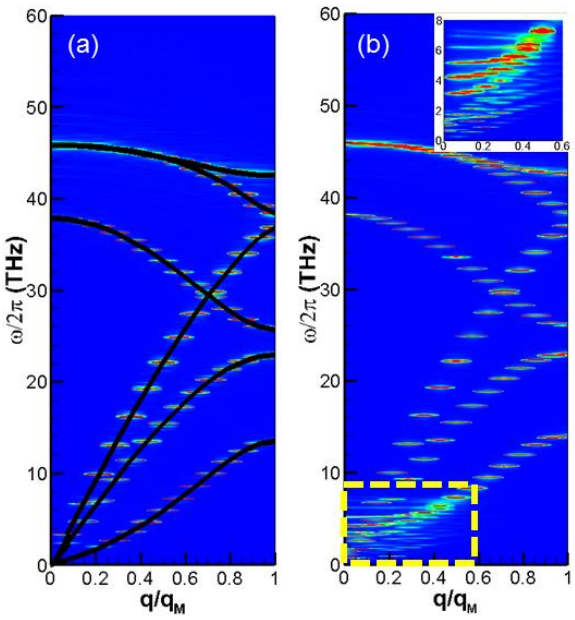

Figure 6.5 Phonon dispersion curves (a) isolated single layer graphene (SLG) and (b) SLG supported on Cu (111). The inset of (b) shows details of the low frequency region of ZA modes.

Figure 6.6 shows the semi-logarithmic plot of SED versus frequency along the Γ-M direction at q*=2/14 for the isolated and supported SLG. The corresponding fitting curves to Lorentzian function are also presented in this Figure. The SED at the other wave vectors has similar peak-and-valley profiles. Since, the SLG have 28 unit cells in the x direction, there are 14 allowed wave vectors in the Γ-M direction of phonon space.

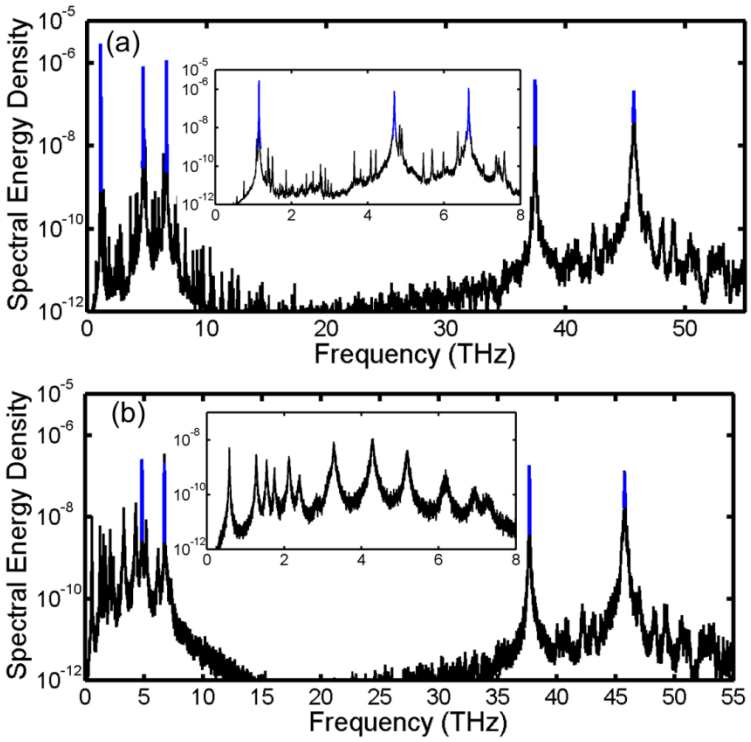

Figure 6.6 Semi-logarithmic plot (black line) of the spectral energy density (SED) along the Γ-M direction at q*=2/14. The blue lines show the fitting curves to Lorentzian function. (a) Isolated single layer graphene (SLG); the inset shows ZA, TA, and LA modes in the region below 8 THz. (b) Supported SLG; the inset shows the modes corresponding to out-of plane vibrations (including ZA mode) in the region below 8 THz.

Comparing Figure 6.6 (a) and (b), it is observed that the first peak corresponding to ZA mode in isolated SLG (Figure 6.6 (a)) is highly suppressed in the supported SLG

(Figure 6.6 (b)). Several new peaks corresponding to the out-of-plane vibration modes appears for supported SLG as shown in the inset of Figure 6.6 (b). The intensity of newly created peaks have been significantly diminished for wave vectors larger than 0.5. The ZA mode of the isolated SLG (the first peak in Figure 6.6 (a)) has the largest magnitude and narrowest width, which indicate a long lifetime. The magnitude of SED of ZA mode in supported SLG is more than 2 orders smaller than that of isolated SLG. The life time of ZA mode of isolated SLG is in the range of 12 ps to 165 ps; relatively long life time is observed in the small wave vector region. The suppressed ZA modes of supported SLG have a lifetime below 17 ps for all the allowed wave vectors. The newly created phonon modes due to the substrate scattering have small life time as well as small group velocities (as shown in the inset of Figure 6.5 (b)), which indicates a negligible contribution to the thermal transport. The TA and LA modes have relatively small phonon life time, 4 ps - 43 ps for the isolated SLG and 1.5 ps - 20 ps for the supported SLG.

The contribution of different phonon modes to thermal conductivity of isolated and supported SLG (χ=1) are listed in Table 6.1. The classical definition of phonon specific heat is $C_{ph} = k_B$. The mode contribution is calculated using both the classical and quantum definitions of C_{ph}. The contributions from the small wave vector region, q*<0.5, are also presented in Table I in brackets next to the total contribution. Even though ZA modes have a relatively long life time in the low wave vector region, the corresponding contribution to thermal conductivity is small (21% for isolated SLG) due to the small group velocity of ZA modes in this regime. The three optical modes also have small group velocity as well as little contribution to the thermal conductivity. The

peaks for ZA mode of supported SLG are difficult to locate out of those newly appearing modes from the semi-logarithmic plot of SED for the wave vectors q* below 0.5. So, the SED profiles of ZA modes are not fitted for q*<0.5, and the corresponding contribution to the thermal conductivity is neglected. This can be justified as the ZA modes have small contribution in this region due to small group velocity in addition to the large suppression of these modes in supported SLG.

Table 6.1 The mode contribution to thermal conductivity of isolated single layer graphene (SLG) and supported SLG (χ=1). The values in the brackets are the contributions from the small wave vector region (q*<0.5).

Phonon Mode		**ZA** (W/mK)	**TA** (W/mK)	**LA** (W/mK)	**ZO** (W/mK)	**LO** (W/mK)	**TO** (W/mK)	**Total** (W/mK)
Classical C_{ph}	Isolated SLG	361.9 *(77.5)*	330.5 *(198.1)*	654.2 *(303.1)*	180.5 *(25.4)*	73.2 *(0.8)*	6.5 *(1.3)*	1606.7 *(606.6)*
	Supported SLG	79.9 *(N/A)*	247.6 *(126.6)*	576.8 *(232.9)*	155.4 *(29.0)*	88.1 *(0.6)*	7.0 *(1.8)*	1154.8 *(390.9)*
Quantum C_{ph}	Isolated SLG	314.1*(76.0)*	240.2 *(171.0)*	310.7 *(225.7)*	34.0 *(2.9)*	4.7 *(0.0)*	0.3 *(0.0)*	903.9 *(475.7)*
	Supported SLG	63.7 *(N/A)*	168.8 *(107.1)*	247.3 *(172.8)*	29.3 *(3.3)*	5.6 *(0.0)*	0.3 *(0.1)*	514.9 *(283.3)*

Referring to Table 6.1, it is observed that the contributions from LA, ZO LO and TO modes to the thermal conductivity are reduced by 50% at least when the quantum definition of C_{ph} is used. This is because the quantum definition gives a small value of C_{ph} at high frequency region due to the low phonon population and major contributions to LA, ZO, LO and TO modes come from high frequency region. Table I shows the thermal conductivity estimations using classical definition of C_{ph} is in good agreement with the Green-Kubo results for both isolated and supported SLG. This is comprehensible

as the thermal conductivity predictions using Green-Kubo method is done using classical EMD results. The reduction in total thermal conductivity due to the substrate scattering is 28.1% using the classical definition of C_{ph}, which is also in good agreement with the Green-Kubo method.

The contributions from the three acoustic modes (ZA, TA, and LA) dominate the thermal conductivity for both isolated and supported SLG. In isolated SLG, the LA, TA, and ZA phonons contribute 654.2, 330.5, and 361.9 W/mK, respectively. The contribution of LA phonons is about 40% at the room temperature while TA and ZA phonons contribute 20% and 22%, respectively. The study in Ref. [95] showed the contributions of 50% and 49% from LA and TA phonons and negligible contribution from the rest of phonons at T=400K. In the SLG supported on Cu, the ZA modes have been highly suppressed due to the substrate scattering. The reduction in ZA mode contribution is about 282 W/mK (78%) and 250 W/mK (80%) for the classical and quantum definition of C_{ph}, respectively. As indicated in Figure 6.5 (b) and Figure 6.6 (b), the ZA phonons below 6 THz ($q^* \leq 0.5$) have been suppressed, but their contributions are only 77.5 W/mK (see Table 6.1) which are much smaller than the total reduction in ZA mode contribution. This suggests that the phonon lifetimes of ZA phonons above 6 THz ($q^* > 0.5$) are also significantly reduced due to the interaction with the substrate. The thermal conductivities of LA and TA phonons decrease by 12% and 25% for the classical definition of C_{ph}. However, as the contributions of the LA and TA phonons are large in the isolated SLG, the absolute value of their reduction is comparable to that of ZA phonons.

6.6 Closure

In summary, the contribution of different phonon modes to the thermal conductivity of both isolated and Cu supported SLG is studied using equilibrium MD simulations. While using the classical definition of specific heat, the results from the Green-Kubo and RTA methods are in good agreement for both isolated and supported SLG. The analysis using Green-Kubo method shows a thermal conductivity reduction of 28%~44% due to the substrate scattering which strongly depends on the interaction strength between C and Cu atoms. The thermal transport in the isolated SLG is dominated by the three acoustic modes, the LA, TA, and ZA phonons modes which contribute 654.2, 330.5, and 361.9 W/mK to lattice thermal conductivity, respectively. The interaction with Cu-substrate results in several new phonon modes but with negligible contribution to the thermal conductivity as they have small group velocities and life time. The thermal conductivity contribution of LA, TA, and ZA phonons are reduced by 12%, 25%, and 78%, respectively due to the interaction with Cu substrate. The reduction in phonon thermal conductivity of SLG supported on different metals or dielectric materials will be different as interfacial interaction strongly depends on the bonding and structure at the interface.

The MD predictions of the substrates effects on SLG thermal conductivity are consist with previous experimental and numerical studies at the same level of magnitude. Unfortunately, no experimental work has been reported for the detailed phonon mode contribution to the SLG thermal conductivity. Instead of the direct measurements of contribution from each phonon mode, the phonon mean free path dependence of thermal conductivity has been experimentally determined for some materials such as bulk

crystalline silicon [220] and silicon membrane [221]. The phonon mean free path can be obtained from the phonon lifetime presented in the current work, which can be used for the future validation with similar experimental measurement on graphene.

CHAPTER 7

ATOMISTIC GREEN'S FUNCTION CALCULATION OF THERMAL BOUNDARY CONDUCTANCE AT GRAPHENE/CU INTERFACES

In graphene based electronic devices, thermal transport across graphene-metal interfaces becomes particularly important [74] when contact resistance become obstacle in effective heat removal from the devices, *e.g.*, contacts in short channel field effect transistors (FETs) and graphene-Cu hybrid-interconnects [72, 73, 222]. The thermal boundary conductance (TBC) between graphene/graphite and various metals has been measured, and relatively low TBC at interfaces (*e.g.*, 7-20 MW/m^2K for graphene-Au [84, 107, 108] and 40-60 MW/m^2K graphene-Cu [223] at room temperature) were reported. Low TBC at graphene interfaces [105, 224] can become a critical challenge for high frequency applications of graphene FETs and interconnects. The prediction of phonon transmission and TBC at graphene/metal interfaces can serve as important inputs for models of the electro-thermal transport in graphene devices.

This chapter presents the investigation of the phonon transmission and TBC across graphene/Cu interfaces. AGF based model compute the TBC across Cu/SLG/Cu interfaces using the atomic structure and IFCs predicted from the DFT calculations. The impact of interactions at interface on the phonon dispersion and vibrational DOS of graphene and Cu contact are discussed. AGF calculations are performed for two cases with different in-plane lattice constants in order to investigate the influence of stress on the phonon transmission function and TBC. The calculated phonon dispersion for

graphene and the prediction of TBC across SLG/Cu interface by AGF are compared against the experimental measurements.

7.1 DFT Optimization of SLG/Cu Structures

A single layer graphene (SLG) sandwiched between two Cu layers is considered in the AGF calculations as shown in Figure 7.1 (a). At SLG/Cu interfaces, the SLG honeycomb lattice is positioned to match the Cu (111) lattice to form the top face-centered cubic (top-FCC) configuration Figure 7.1 (b), which is demonstrated to be the most stable configuration with lowest energy. [76, 212] In the absence of accurate empirical model to describe the graphene/Cu interactions, DFT calculations are employed to determine the IFCs.

DFT calculations with local density approximation (LDA) [225] functional are performed to determine the optimized lattice constants of isolated SLG and bulk Cu, and equilibrium spacing d between SLG and Cu substrate, respectively. As shown in Figure 7.1 (c), the in-plane lattice constant of SLG/Cu system is defined as length a which is also the definition of lattice constant of graphene primitive unit cell. The FCC lattice constant of bulk Cu is $a_{\mathrm{FCC}} = \sqrt{2}a$. Here, the lattice constant of graphene primitive unit cell a is used for the following discussion of bulk Cu, SLG, and SLG/Cu systems. The optimized lattice constants and equilibrium spacing are listed in Table 7.1.

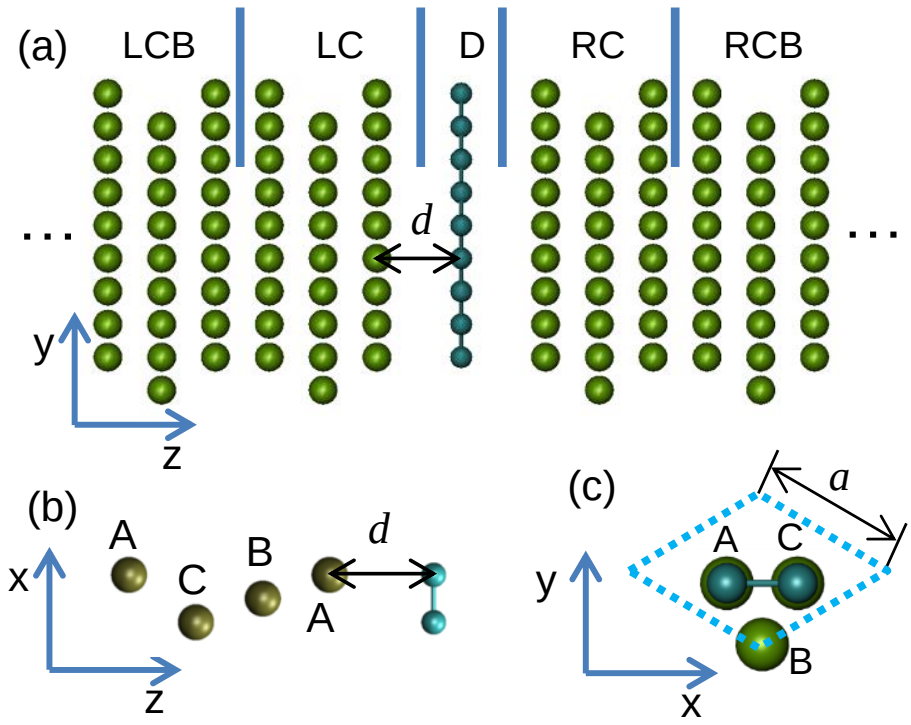

Figure 7.1 (a) Schematic of Cu/SLG/Cu system for the AGF calculation. A single layer graphene (SLG) is considered as the device (D). It is sandwiched between two Cu contacts: left contact (LC) and right contact (RC). The regions beyond LC or RC are defined as the left contact bulk (LCB) and right contact bulk (RCB), which do not interact with the device region. View in (b) x-z plane and (c) x-y plane of a unit cell with 2 C atoms on Cu atoms. Only four layers of Cu are shown in (b).

Table 7.1 Lattice constant (*a*) of unit cell shown in Fig. 1c and corresponding SLG-Cu equilibrium spacing (*d*).

	Case I	Case II
SLG lattice constant (Å)	2.45	2.49
SLG-Cu spacing (Å)	3.23	3.18

The effects of stress on the TBC and phonon interactions at graphene-Cu interface are studied by comparing two cases which have different lattice constants for the unit cell in Figure 7.1 (c): Case I with graphene lattice constant of a =2.45 Å and corresponding d =3.23 Å; Case II with Cu lattice constant of a =2.49 Å and corresponding d =3.18 Å. In Case I, The SLG structure is optimized using LDA, and Cu lattice is compressed and matched to SLG lattice. In Case II, the lattice constant of the FCC structure of Cu is optimized using LDA, and SLG lattice is stretched to match the Cu lattice. The equilibrium spacing in Case II is reduced by 0.05 Å compared to Case I as the SLG lattice constant is increased from 2.45 Å in Case I to 2.49 Å in Case II. This indicates that the interaction between SLG and Cu can be enhanced by stretching the SLG lattice. The IFCs between C-C, Cu-Cu, and C-Cu atom pairs are determined using DFT calculations for the optimized lattice constants and equilibrium spacing.

7.2 Validation of IFCs Calculation using Phonon Dispersions

The phonon dispersion of SLG is determined by diagonalizing the dynamical matrix constructed using IFCs obtained from the DFT simulations with LDA functional. Figure 7.2 (a) compares the phonon dispersion of isolated SLG with unstretched lattice constant a =2.45 Å and stretched lattice constant a =2.49 Å, and experimental measurements [226]. As the lattice constant a is stretched by 1.6%, TO and LO modes are strongly softened by 3 THz for the entire Γ-K branch. The softening in LA modes increases from Γ point to K point with the largest softening of 2.3 THz at K point. The softening of LA, TO, and LO modes indicates the decrease of in-plane stretching force constant and increase of out-of-plane bending force constant due to the increase of C-C

bond length [227, 228]. Compared to the experimentally measured dispersion relation of surface phonons of graphite in Figure 7.2 (a), the DFT calculation with unstretched lattice constant has a good agreement except for the ZA/ZO and LA/LO modes at K point. The present calculations show no splitting of the ZA/ZO modes and LA/LO modes at K point, but splitting of modes is observed in the experimental measurements. [226, 229] This disagreement might be because the thin flake of graphite used in the experiments [229, 230] had the possible admixture of micro-crystallites of different orientations [182].

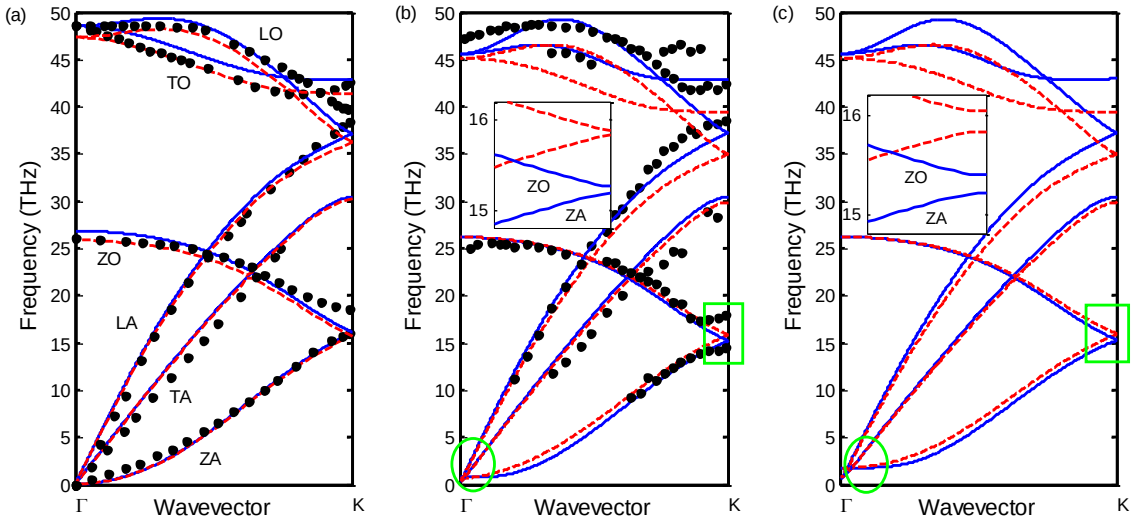

Figure 7.2 Phonon dispersions of (a) isolated SLG; (b) SLG supported on Cu (111); (c) SLG sandwiched between two Cu (111) surfaces. Black dots in (a) and (b) are experimental measurements from Ref. [226] for surface phonons of pure graphite and phonon modes of graphene in graphene/Cu/Ni, respectively. Solid blue lines and red dashed lines in (a), (b) and (c) are calculated for the unstretched and stretched SLG, respectively. The insets in (b) and (c) are the zoom-in plot of ZA and ZO modes around K point as indicated by the green boxes. The lifting in ZA modes at Γ points is marked with green circles in (b) and (c).

Figure 7.2 (b) shows the phonon dispersions of Cu supported SLG for unstretched graphene with lattice constant a =2.45 Å, stretched graphene with lattice constant a =2.49 Å, and experimental measurements [226]. In the experiments by Shikin *et al.* [226, 231] about one layer of Cu was intercalated underneath the SLG supported on Ni (111). In comparison to the phonon dispersion of isolated SLG in Figure 7.2 (a), TO and LO modes at Γ point are significantly softened, and ZO modes from Γ to K are slightly softened, which can be observed in both the DFT calculations and experimental measurements. The softening in TO, LO and ZO modes is because of the charge transfer from the *d* bands of Cu to C atoms in SLG which weakens the π bonding in SLG. The inset of Figure 7.2 (b) zooms in the region of green box which shows the ZA and ZO modes near K point. The slight splitting between ZA and ZO modes can be observed at K point. It is 0.05 THz for the unstretched SLG and 0.08 THz for the stretched SLG. Besides, a small lifting of acoustic modes is observed at Γ point (*e.g.*, 0.76 THz and 0.67 THz for ZA modes of the unstretched and stretched SLG), as indicated by the green circle in Figure 7.2 (b) [94]. When the SLG is sandwiched between the Cu layers, the gaps between ZA and ZO modes at K point are 0.17 THz and 0.2 THz for the two cases, respectively, as shown in Figure 7.2 (c). According to the previous studies [227, 228], the gap between ZA and ZO modes at K points indicates the interaction strength between SLG and the metal substrate. The increase of the interaction strength can directly change the TBC that will be shown by AGF calculations.

7.3 Phonon Density of States at SLG/Cu Interface

The density of states (DOSs) of the lattices near the interface indicates the phonon population available for interfacial coupling over the frequency range of interest. The effects of SLG-Cu interactions on the density of states (DOSs) of Cu and SLG are shown in Figure 7.3. In left contact (LC) or right contact (RC) region, the strong Cu-Cu bonding at the SLG/Cu interface is replaced by weak interactions between Cu atoms and C atoms. This leads to a shift in Cu phonon DOSs to the lower frequencies (see blue line in Figure 7.3 (a)). This red-shift has also been observed in the DOSs of surface phonons in transition metals and silicon [78, 232, 233]. The interaction with Cu substrate also affects the DOSs of graphene as shown in Figure 7.3 (b). The DOSs of graphene are suppressed at low frequencies (< 1.7 THz marked with red circle in Figure 7.3 (b)), while a new peak is observed around 46 THz (marked with black arrow in Figure 7.3 (b)) for the sandwiched SLG. The LO and TO modes are softened to frequencies around 46 THz (see Figure 7.2 (c)), and the abundance of these phonon modes around Γ point create the new peak in DOSs around 46 THz.

Figure 7.3 (c) compares the DOSs of device graphene for the two cases in low frequency region (0-10 THz). The DOSs of device graphene for Cases I and II is nearly zero below 1.8 THz, which corresponds to the lifting of ZA modes at Γ point in Figure 7.3 (c). At frequencies near zero, the longitudinal acoustic (LA) and transverse acoustic (TA) phonon branches show linear relationship between frequency and wave vector while the out-of-plane acoustic (ZA) phonon branch has a quadratic dispersion [145]. DOSs of isolated graphene near zero frequency is populated by ZA modes [185, 234]. However, the DOSs of the device graphene decreases to almost zero at low frequency (<

1.7 THz) which indicates that the ZA modes are highly suppressed at low frequency as shown in Figure 7.3 (c) [70].

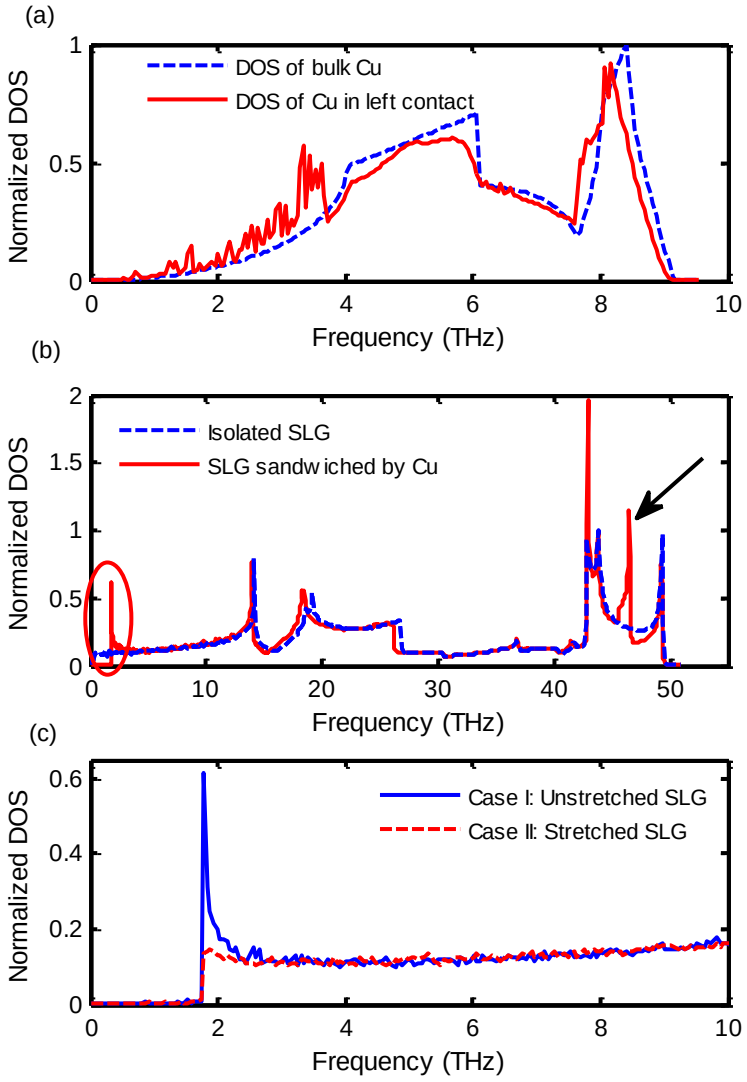

Figure 7.3 (a) Density of states (DOSs) of bulk Cu and Cu in LC region of Cu/SLG/Cu system with unstretched SLG lattice constant. (b) DOSs of isolated SLG and SLG sandwiched between Cu layers of Cu/SLG/Cu system with unstretched SLG lattice constant. Region with suppressed ZA modes is marked with red circle while the new peak created by the softening of TO and LO modes is marked with black arrow. (c) DOSs of unstretched and stretched SLG in Cu/SLG/Cu system below 10 THz.

7.4 Effects of Stress on Thermal Boundary Conductance

A distinct phonon spectrum mismatch between Cu and graphene is observed by comparing Figure 7.3 (a) and Figure 7.3 (b). The phonon modes in Cu are below 9 THz while the vibrational frequencies of graphene are up to 50 THz. This mismatch in phonon spectrum between graphene and Cu restricts the phonon transmission to the frequencies below 9 THz as shown in the inset of Figure 7.4. By comparing transmission function with DOSs of SLG in Figure 7.3 (c), it can be observed that the behavior of phonon transmission at low frequency (below 1.7 THz) in each case is in agreement with the trends in DOSs of sandwiched SLG. The suppressed ZA modes below 1.7 Hz cannot contribute to the phonon transmission across Cu/SLG/Cu interfaces.

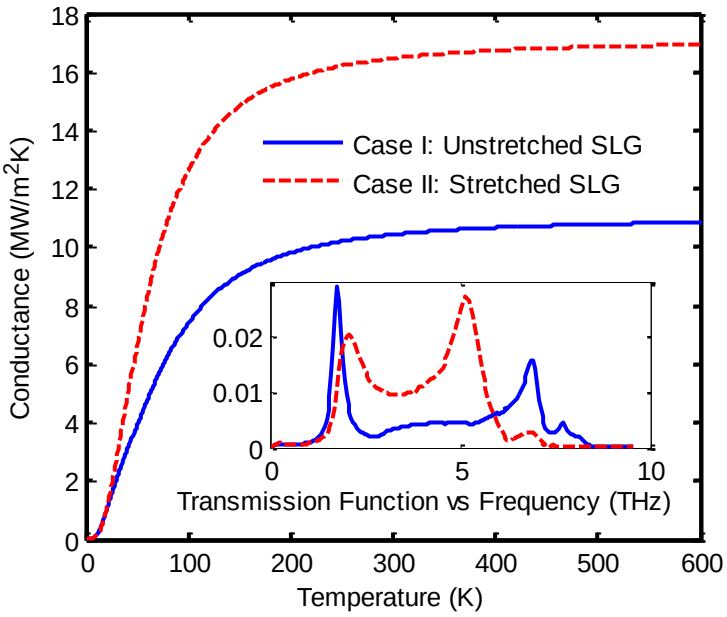

Figure 7.4 Thermal boundary conductance at Cu/SLG/Cu interfaces as a function of temperature for unstretched and stretched SLG. The inset shows transmission function for the two cases.

Figure 7.4 also shows the TBC as a function of temperature. Because the phonon transmission is generally limited to frequencies below 9 THz, the TBC levels off beyond 300 K. The TBC for Cases I and II is 10.4 MW/m^{2}K and 16.5 MW/m^{2}K at 300 K, respectively. The lattice constant of graphene is increased by 1.6%, and the equilibrium spacing is reduced by 1.6% from Case I to Case II (see Table 7.1), but the TBC is increased by 59%. The interaction strength between SLG and Cu is increased in Case II compared with Case I, which is also in agreement with the phonon band gap increase between ZA and ZO modes at K point from Case I to II.

The TBC shown in Figure 7.4 corresponds to two Cu-graphene interfaces. Neglecting the thermal resistance across SLG [107], the TBC across single SLG/Cu interface at 300 K should be twice of the value shown in Figure 7.4, i.e., 20.8 and 33 MW/m^{2}K for Cases I and II. Experimental measurements have been reported for TBC across interface of highly ordered pyrolytic graphite (HOPG) and Cu [83]. The as-cleaved sample had highest TBC of 60 MW/m^{2}K, while the vacuum-cleaved sample yielded a lower TBC around 55 MW/m^{2}K [83]. The TBC for as-cleaved sample is higher because of the presence of absorbed impurities at interface which may have been introduced during the deposition of Cu on HOPG in the presence of the water and hydrocarbons [83]. The crystalline Cu with smooth surface is used in current work, and the calculated TBC (20.8 MW/m^{2}K and 33.0 MW/m^{2}K for unstretched and stretched cases respectively) is lower but comparable to the experimental measurements. However, the higher TBC in the experimental measurements indicates stronger interaction between Cu and graphite which depends on the deposition technique and complicated interface structure. The elevated temperature during the metal deposition can also increase the

reactivity between metal and HOPG. Besides, the inelastic scattering at the interface, which is a challenge to include in the AGF calculation, can also contribute to the interfacial thermal transport. For materials with significant mismatch of phonon spectrum, the inelastic phonon scattering can open new channels for thermal transport [84, 235-237].

7.5 Closure

In summary, the effects of SLG and Cu lattice constants on the phonon transmission across Cu/SLG/Cu interfaces are investigated using AGF and DFT simulations. The results show that the phonon DOSs of SLG and phonon transmission across SLG/Cu is nearly zero below 1.7 THz because of the suppression of ZA phonon modes in graphene. Low TBCs from 10 to 16.5 MW/m^2K are obtained across Cu/SLG/Cu interfaces, which can be attributed to the weak atomic interactions and significant mismatch of phonon spectrum. Stretching the SLG lattice to match Cu lattice reduces the spacing between SLG and Cu and enhances the interfacial interaction which significantly increases the TBC (~ by 59%).

CHAPTER 8

IMPACT OF BONDING AT GRAPHENE/METAL INTERFACES ON THERMAL BOUNDARY CONDUCTANCE

The single layer pristine graphene sheet has very small bandgap which makes it un-suitable for logic applications [72]. Bandgap of MLG can be tuned by controlling the stacking order while maintaining high carrier mobility [75, 238]. The recent progress in fabrication and structure-manipulation techniques has made MLG a promising material for nano-electronic devices [239-241]. MLG can have considerable contact with metal electrodes in its electronic devices which can also be an important pathway of heat dissipation. [222, 242] Many previous studies have measured TBC between graphene/graphite and various metals such as Cu, Au, Ti, Al, *etc*. [83, 84, 106, 108]. Very low TBC has been reported for some metals such as 7-20 MW/m^2K for graphene/Au interfaces [84]. The low TBC can hinder the effective heat removal from the nano-electronic devices leading to degradation of performance and reliability [242]. Therefore, it is crucial to estimate TBC and decipher phonon transport mechanism at various graphene/metal interfaces to engineer these interfaces for effective thermal management and enhanced performance.

This chapter studies the impact of interfacial bonding on thermal transport between MLG and different metals using DFT and AGF based calculations. The phonon transmission and TBC across metal/SLG/metal and metal/MLG/metal interfaces are determined for three different materials: Cu and Au for the weak

physisorption bonding and Ti for strong chemisorption bonding. The phonon coupling at interfaces with different chemistry and bonding strength is discussed. NEMD simulations are performed to validate the findings of AGF calculations and examine the anharmonic effects. The findings in this study will provide insights to understand recent experimental measurements of TBC at graphene/metal interfaces and to engineer these interfaces to enhance TBC.

8.1 Simulation Setup and Parameters

8.1.1 Atomistic Structures at Graphene/Metal Interfaces

The phonon transmission and TBC at metal/SLG/metal and metal/MLG/metal interfaces are considered for three different materials: Cu and Au for the weak physisorption interactions and Ti for strong chemisorption interactions. Figure 8.1 (a) and (b) show the structures of SLG/metal and MLG/metal interfaces considered in the AGF calculations. The SLG or MLG is sandwiched between two metal contacts to form the symmetrical metal/SLG/metal or metal/MLG/metal structures. The phonon transmission and TBC across the device (SLG or MLG) region involve two identical interfaces, and the values across single interface can be obtained by a multiplication of 2. A top view, in x-y plane, of the graphene/metal interfaces are shown in Figure 8.1 (c), (d), and (e) for Cu, Au and Ti, respectively. Cu (111), Au (111), and Ti (0001) surfaces are cleaved to make contact with graphene sheets; these surfaces are perpendicular to z axis (see Figure 8.1). In order to form periodic lattices in x and y directions, a

graphene/Cu unit cell consists of one graphene unit cell while the graphene/Au and graphene/Ti unit cells consist of four graphene unit cells.

8.1.2 DFT Calculations of Optimized Distance and Interatomic Force Constants

DFT simulations are implemented in Vienna *ab initio* package (VASP). [243] Plane wave basis sets with a kinetic energy cutoff of 400 eV are used in the projector augmented-wave (PAW) method. [244] 32 × 32 × 1 k-point grids for Cu/SLG system and 21 × 21 × 1 k-point grids for Au/SLG and Ti/SLG structures are used. The optimized in-plane lattice constant *a* of graphene is 2.45 Å, and the metal lattices are adjusted to match graphene lattices. With *a*=2.45 Å, the spacings *d* between graphene and metal surfaces are further optimized using DFT calculations. The optimized spacing are 3.23 Å, 3.37 Å, and 2.15 Å for the Cu, Au, and Ti interfaces with graphene respectively as shown in Figure 8.1 (c), (d), and (e), which is consistent with previous DFT studies [76, 212]. The graphene/Ti spacing is quite closed to the Ti-C bonding length (2.13 Å) in a TiC crystal which indicates the chemisorption interactions for the two Ti-C pairs at graphene/Ti interface in a unit cell as shown in Figure 8.1 (e).

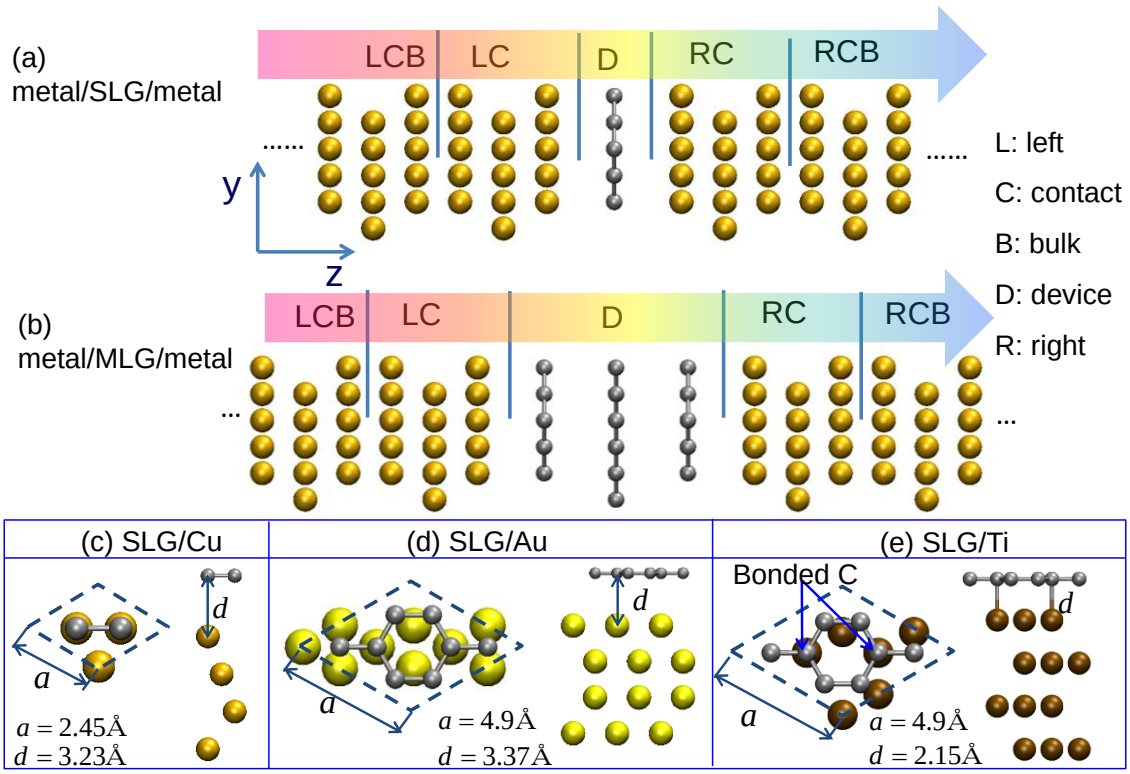

Figure 8.1 Schematic of (a) metal/SLG/metal system and (b) metal/MLG/metal system for the AGF calculations. Multi-layer graphene consists of single layer graphene (SLG) with AB stacking. The SLG and MLG are considered as the devices (D) which are sandwiched between two metal contacts: left contact (LC) and right contact (RC). The regions beyond LC or RC are defined as the left contact bulk (LCB) and right contact bulk (RCB), which do not interact with the device region. Views in x-y plane and x-z plane of a unit cell for (c) SLG/Cu, (d) SLG/Au and (e) SLG/Ti structures, respectively. These structures have been optimized using DFT simulations to calculate the equilibrium distance between metal and graphene. Only four layers of metal atoms are shown.

The second order IFCs for C-C, metal-metal, and metal-C atom pairs are obtained by DFT calculations using a 5×5 supercell for Cu/SLG system and a 3×3 supercell for Au/SLG and Ti/SLG system [245]. Brillouin zone of this supercell is sampled with 3×3

× 1 k-point grids, and each atom in the unitcell is displaced in two directions: in plane and orthogonal to the graphene plane. The displacement magnitudes are ±0.03 Å in both cases.

8.1.3 Non-equilibrium Molecular Dynamics Simulations Parameters

NEMD simulations are performed on Cu/3LG/Cu structures using Lammps package [191]. The optimized Tersoff potential [145] and embedded-atom method (EAM) potential [213] to describe the C-C interactions and Cu-Cu interactions, respectively. Lennard-Jones (L-J) potential the interaction is used to model the interactions between C-Cu atoms at the interface. Details of the parameter sets can be found in Chapter 6.1. A time step of 0.5 fs is used in all simulations. The system is periodic in the cross-section perpendicular to the graphene plane. One atomic layer beyond the heating/cooling bath is fixed. The dimensions of the system are 38.8 Å × 42.3 Å × 267.5 Å and the total number of atoms in system is 40,392. Each system is first equilibrated in NVT at 300K for 0.5 ns and in NVE for another 0.5 ns. Then a heat rate of +/- 45 nW is applied at the heating/cooling bath which consists of 3519 atoms. Each case is simulated for 5 ns to first obtain a steady state, and then the data is sampled for additional 5 ns which is used for the estimation of temperature profiles.

8.2 Atomic Interactions at Interfaces between Graphene and Metals

The bonding between graphene and metal atoms at the interface can be illustrated by the distribution of electron localization function (ELF) as shown in Figure 8.2. ELF

describes chemical bonds by the probability of finding another same-spin electron in the neighborhood of a reference electron [246]. ELF is normalized to have values between 0 and 1, where ELF=1 corresponds to complete localization and ELF=0.5 corresponds to uniform electron gas [247].

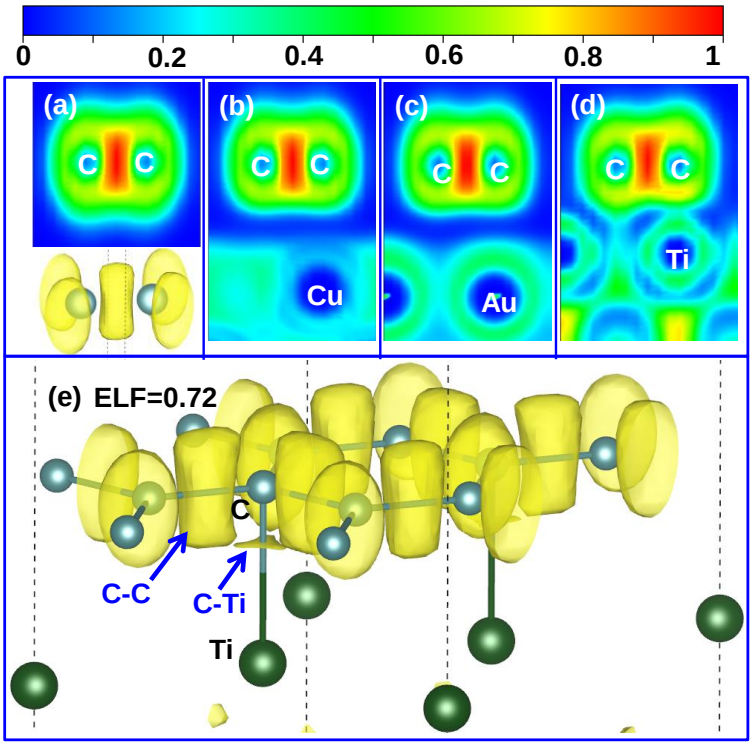

Figure 8.2 Electron localization function (ELF) for isolated single layer graphene (SLG) and SLG on metal substrates. (a) ELF contour and iso-surfaces with ELF=0.72 for isolated SLG; (b) ELF contour for SLG on Cu (111); (c) ELF contour for SLG on Au (111); (d) ELF contour for SLG on Ti (0001); (e) ELF iso-surfaces with ELF=0.72 for SLG on Ti (0001). The arrows in (e) indicates the electron localization between C atoms in SLG and between C and Ti atoms at SLG/Ti interface, respectively.

Figure 8.2 (a) shows the ELF contour of a unit cell of SLG in a cross-section perpendicular to SLG sheet and containing a C-C bond [248]. The red region with high

ELF values between two C atoms indicates C-C sp^2 bonding in SLG while the lower part of Figure 8.2 (a) shows the iso-surfaces of ELF=0.72. Figure 8.2 (b) to (d) show the ELF contour around C and metal atoms at SLG-metal interfaces. At SLG-Cu or SLG-Au interface, electron localization is not observed and the ELF distribution of SLG remains almost same as isolated SLG. However, the strong interaction with Ti has distorted the ELF distribution of SLG. The overlap in ELF of SLG and Ti can be observed in Figure 8.2 (d). Figure 8.2 (e) shows the iso-surfaces of ELF=0.72 at SLG-Ti interface. A strong electron localization can be observed at SLG-Ti interface between C and Ti atoms, whose position is closer to C atom. This indicates that the two C atoms located just above Ti atoms in a unit cell (see Figure 8.1 (e)) make chemical bonds with corresponding Ti atoms, while other six C atoms of the unit cell are not bonded to Ti. Gengler *et al.* examined the interfacial chemistry for thin titanium films deposited on HOPG using X-ray photoelectron spectroscopy, and showed that Ti-C can be formed at Ti/HOPG interface depending on the deposition conditions which is consistent with the simulations in this work [83]. The ELF for non-bonded C atoms is also distorted (see Figure 8.1 (d)) but electron localization is not observed.

8.3 Phonon Density of States at SLG/Metal Interfaces

In order to investigate the effects of graphene-metal interaction on phonon distribution, the phonon density of states (DOSs) of the SLG supported on metal substrate are calculated using IFCs estimated from the DFT simulations. Figure 8.3 (a) shows the DOSs of isolated SLG while Figure 8.3 (b) to (d) show the DOSs of SLG supported on Cu (111), Au (111), and Ti (0001), respectively.

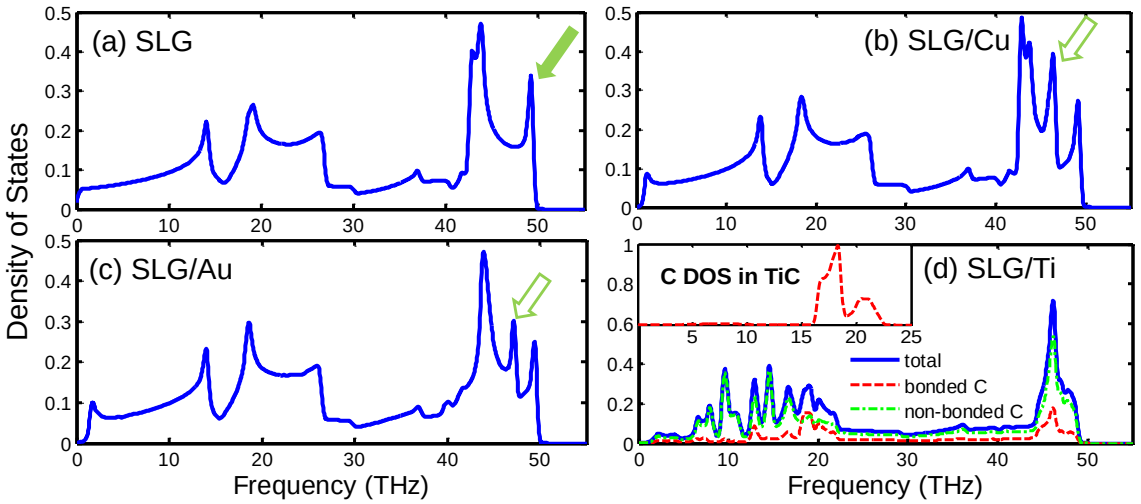

Figure 8.3 Phonon density of states (DOSs) of (a) isolated single layer graphene (SLG), (b) SLG on Cu (111), (c) SLG on Au (111) and (d) SLG on Ti (0001). The DOSs in (d) is decomposed to partial DOSs of Ti-bonded C atoms and non-bond C atoms. The inset in (d) shows the partial DOSs of C atoms in TiC crystal. The scale of y-axis in inset is from 0 to 1. The partial DOSs of C in TiC diminish to zero beyond 25 THz. The solid arrow in (a) indicates the optical phonon states near zone-center in isolated SLG while hollow arrows in (b) and (c) indicate the phonon states due to softening of optical phonon states near zone-center by Cu or Au substrate.

Comparing to the DOSs of isolated SLG, the major changes in DOSs of SLG supported on Cu (111) and Au (111) are around zero frequency and high frequency region, which are associated with the effects of Cu (111) or Au (111) substrate on acoustic and optical phonon modes near the zone-center (Γ point), respectively. As shown in Figure 8.3 (b) and (c), the DOSs near zero-frequency is first suppressed and then increased rapidly with a small overshoot near 1.2 THz and 1.7 THz for SLG/Cu and SLG/Au structures, respectively. This is due to the interactions with substrate which

break the symmetry of SLG for out-of-plane acoustic (ZA) modes and ZA modes near zone-center leading to non-zero frequencies for these modes at zone center [85, 228]. A high frequency peak (~ 49 THz) in SLG DOSs is indicated by a solid arrow in Figure 8.3 (a) which can be attributed to the longitudinal and transverse optical modes near zone-center. The physisorption interactions with substrate soften the LO and TO modes near zone-center to lower frequencies and create the peaks around 46.4 THz and 47.2 THz which are indicated by hollow arrows in Figure 8.3 (b) and (c) [85, 228].

In contrast to physisorption interactions, the chemisorption interactions with Ti substrate substantially change the DOSs of SLG as shown in Figure 8.3 (d). As discussed during the analysis of ELF for SLG/Ti system, two C atoms located just above the Ti atoms are bonded with Ti atoms while the other six C atoms are not bonded. The DOSs of SLG is decomposed to the partial DOSs of these two types of C atoms as shown in Figure 8.3 (d). The partial DOSs of both bonded and non-bonded C atoms are significantly changed throughout the phonon spectrum due to the strong SLG-Ti interactions. SLG-Ti (0001) spacing d (~2.17 Å) is close to Ti-C bond length (~2.13 Å) [249] in TiC. In addition, the peak in phonon DOSs around 20 THz also agrees with the DOSs of C atoms in TiC as shown in the inset of Figure 8.3 (d), which implies chemical interactions between Ti and C atoms in SLG/Ti (0001) system is similar to TiC.

8.4 Thermal Boundary Conductance across Single-Layer Graphene

Figure 8.4 shows the phonon transmission functions across metal/SLG/metal interfaces calculated from the AGF method. The sizes of a unit cell in three metal/graphene systems are different (Figure 8.1). For comparison, the transmission

functions are divided by the number of SLG primitive unit cells (with two C atoms) in the corresponding metal/graphene system. Because of the harmonic assumption in the AGF method, only phonons of same frequency can interact at the interfaces. Since the phonon spectrum of Cu, Au and Ti are below 10 THz and much smaller than the phonon spectrum of SLG (up to 50 THz), the phonon transmission is also restricted to frequencies below 10 THz. The coupling between higher-frequency phonons in SLG and phonons in metal contacts is neglected in AGF calculations. However, its contribution to the phonon transport is not significant unless high pressure is applied to enhance the SLG/substrate interactions [79].

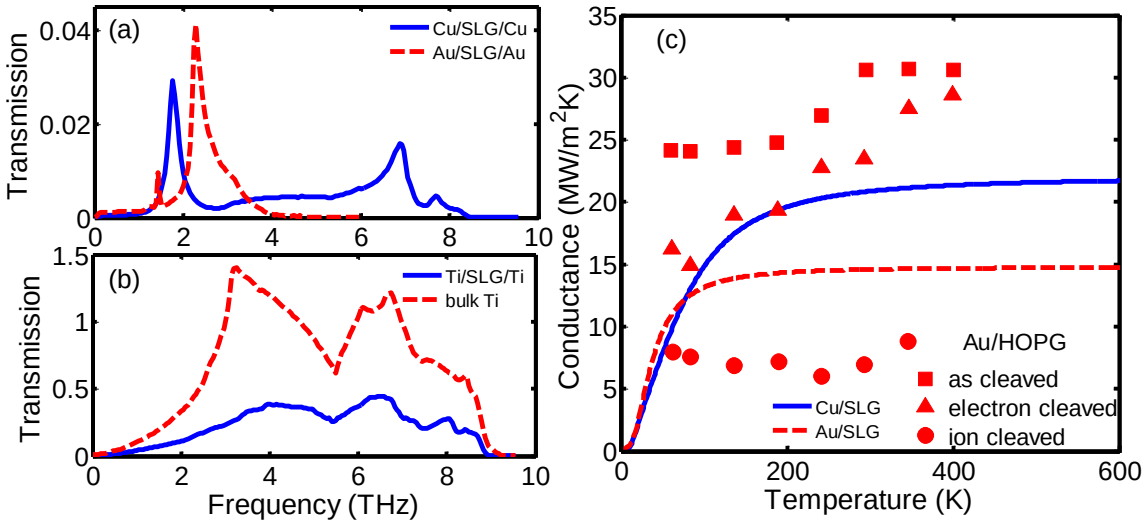

Figure 8.4 Phonon transmission as a function of frequency in (a) Cu/SLG/Cu and Au/SLG/Au structures and (b) Ti/SLG/Ti system and bulk Ti. (c) Thermal boundary conductance (TBC) at Cu/SLG and Au/SLG interfaces as a function of temperature (lines from current work). Experimental measurement (markers) [84] of TBC at Au/HOPG interfaces for three different methods of surface treatment (as cleaved, electron cleaved and ion cleaved) of HOPG before Au deposition.

As shown in Figure 8.4 (a), the transmission functions across Cu/SLG/Cu and Au/SLG/Au interfaces are very small (<0.04). The frequency of the first peak in the transmission curve of Cu/SLG/Cu or Au/SLG/Au system corresponds to the peak in DOSs of sandwiched SLG (see Figure 8.3 (b) and (c) near zero-frequency). The transmission function across Ti/SLG/Ti interfaces (see Figure 8.4 (b)) is much larger than Cu/SLG/Cu and Au/SLG/Au structures because of the strong bonding strength at SLG/Ti interfaces with chemisorption interactions. Also shown in Figure 8.4 (b) is the transmission function in bulk Ti crystal with pristine lattices. Ti/SLG interface have reduced phonon transmission in comparison to the Ti/Ti interface, but the transmission function across Ti/SLG/Ti resembles with bulk Ti and has similar order of magnitude, which indicates good phonon coupling at Ti/SLG interface.

The TBCs in the three systems are calculated by Landauer formula using the transmission function estimated from the AGF calculations. Figure 8.4 (c) shows TBC as a function of temperature at Cu/SLG and Au/SLG interfaces calculated from the AGF calculations. In absence of inelastic scattering at metal/SLG interfaces, TBC estimated from AGF calculations saturates to 21.5 MW/m^2K and 14.4 MW/m^2K around ~400 K and ~200 K for Cu/SLG and Au/SLG interfaces, respectively. These temperatures are close to their Debye temperature (343.5 K for Cu and 170 K for Au) above which all phonon modes are excited.

Figure 8.4 (c) also compares the AGF prediction of TBC against the experimental measurements at Au/HOPG interfaces from Ref. [84]. As shown in Figure 8.4 (c), the surface treatment of HOPG can lead to different surface impurity, defects and roughness and thereby significantly change the TBC for three different surface treatments (as

cleaved, electron cleaved and ion cleaved HOPG) before Au deposition. Smooth Au/SLG interface without any defect or contaminant is considered in present work. The prediction of TBC at Au/metal interface by AGF lies between the highest and lowest values of experimental measurements at Au/HOPG interfaces considering three different surface treatments. Considering the difference in the interface conditions, the agreement between the AGF predictions in this work and experiment measurements is reasonably good.

In the experimental measurements as shown in Figure 8.4 (c), the electron cleaned HOPG surfaces are expected to have better condition, *e.g.*, reduced contamination and disorder/defects. Their TBC increases with temperature beyond the Debye temperature of Au (~170 K) which leads to the deviation from the AGF predictions in current work. This temperature dependence indicates the contribution of inelastic phonon-phonon scattering at interfaces which is absent in current AGF model with harmonic assumption. Extension of measurements to the low temperature range (< 100 K) is suggested for further validation of AGF prediction of TBC at graphene/Au interfaces. However, inclusion of inelastic scattering in the Green's function method is required to improve the prediction at interfaces involving materials with low Debye temperature (*e.g.*, Au).

For Ti/SLG/Ti system, the AGF calculations predict extremely large TBC (~ 1000 MW/m^2K around room temperature), which is about one order of magnitude larger than the experimental measurements at Ti/HOPG interface (~120 MW/m^2K around room temperature) [72, 107]. Besides the different interface condition between Ti/SLG interfaces in AGF calculations and Ti/HOPG interfaces in experiments, the difference in the phonon transport mechanism at Ti/SLG and Ti/MLG interfaces may also play an

important role which has not been explored before and will be discussed in the next section.

8.5 Thermal Boundary Conductance across Multi-Layer Graphene

An important query, which is a topic of investigation of some recent studies [71, 82, 156, 173, 174, 250-253], is how the number of graphene layers (*n*) in a MLG affects its thermal conductivity and TBC across its interfaces. The thickness of MLG is generally much smaller than the phonon mean free path of HOPG in cross-plane direction; therefore boundary/interface scattering of phonons is dominant for thermal transport across MLG. It has been demonstrated that the cross-plane thermal conductivity of MLG is smaller than that of HOPG and have a strong dependence on *n* as phonon mean free path in MLG is limited by its thickness [174, 253]. However, both experiments [107] and simulations [82, 173, 250] have shown that the increasing *n* from 3 to 10 only slightly reduces or has no effect on the TBC across embedded MLG. When *n* is less than or equal to three (i.e., single, bilayer or trilayer embedded graphenes), the effect of n on TBC may depend on the contact materials [82, 173, 250]. For SiO_2/graphene interfaces, increasing graphene layers from single to few layers slightly reduces [107, 173] or does not changes [82] the TBC. However, the effect of *n* on TBC at metal/graphene interfaces becomes complicated because of the different interfacial chemistry at different metal interfaces.

In current work, two contact resistances should be considered for the phonon transport analysis at metal/MLG interfaces: (1) R_{MG} which is associated with the coupling of phonons between metal and first layer of MLG; this is investigated in previous section using metal/SLG/metal structures, and (2) R_{GG} which is related with the

phonon coupling between first layer of graphene with the following graphene layer due to different phonon DOSs (see Figure 8.3 (b)). In the metal/MLG/metal system, metal contacts have either physisorption or chemisorption interactions with the first layer of MLG which can significantly change phonon DOSs of this graphene layer. Therefore, significant mismatch in phonon DOSs may exists between the first layer of MLG and following layer which results in the thermal contact resistance R_{GG} in the AGF calculations. This phonon mismatch between layers of graphene depends on the interaction strength with metal contact: physisorption interaction results in small phonon mismatch (Figure 8.3 (b) for Cu/SLG and (c) for Au/SLG) while chemisorption interaction leads to a significant phonon mismatch (Figure 8.3 (d) for Ti/SLG). In order to quantify the effects of metal/graphene interaction on the phonon coupling at two types of interfaces, AGF calculations for metal/MLG/metal structures (Figure 8.1 (b)) for different number of graphene layers ($1 \le n \le 31$) are carried out to determine the phonon transmission and TBC at metal/MLG interfaces.

8.5.1 Thermal Boundary Conductance across Interfaces of MLG with Cu and Au

Figure 8.5 (a) and (b) show the phonon transmission function across Cu/MLG/Cu and Au/MLG/Au interfaces for different *n*. The transmission function across metal/MLG is characterized with multi-peaks at frequencies below 4 THz; the number of peaks equals the number of graphene layers, *e.g.*, 3 or 5 peaks for $n = 3$ or $n = 5$ in Fig. 5 (a) and (b). As the number of graphene layers increases, the peaks diminish and become indistinguishable, *e.g.*, transmission across 31 layers of graphene as shown in Figure 8.5 (a) and (b). Beyond 4 THz, the transmission curves changes insignificantly with

increasing *n*. The transmission function from AGF calculations is consistent with the transmission coefficients obtained from the wave-packet simulations using MD by Shen, *et al*.[82] The study in Ref. [82] only considered the transmission of longitudinal acoustic (LA) phonons; a fine sampling in longitudinal wave vectors and incidence angles requires a huge number of simulations as wave-packets need to be generated for each case. Besides, AGF calculations use plane-wave formulation with a fine sampling in transverse Brillouin zone $\vec{k}_{\parallel} = (k_x, k_y)$. Therefore the transmission of all phonon modes from different incidence angles can be efficiently incorporated in present work.

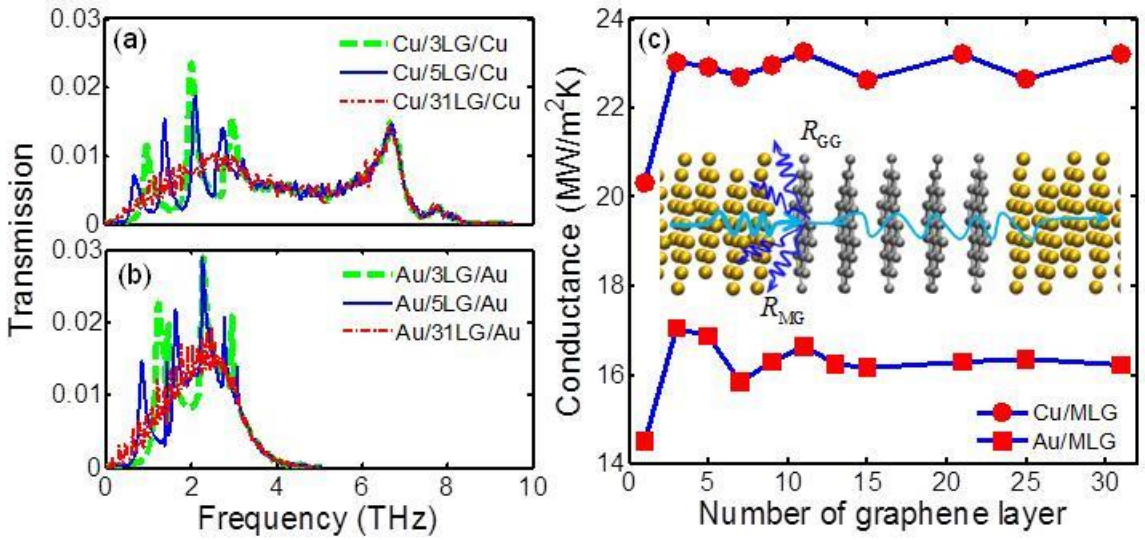

Figure 8.5 Phonon transmission as a function of frequency in (a) Cu/MLG/Cu structures and (b) Au/MLG/Au structures. (c) TBC at Cu/MLG and Au/MLG interfaces as a function of number of graphene layers. The inset chart in (c) shows the dominant phonon scattering is at metal/graphene interface.

The peaks and valleys in transmission curves can be explained by the phonon interference effects [82]. The addition of graphene layers between metal contacts increase

the thickness of MLG as well as the wavelength range of allowed phonon waves so that a new peak in transmission function is created with the addition of a new graphene layer . According to Ref. [82], the oscillatory period in frequency Δf depends on the group velocity v of transmitting phonons and thickness of MLG t: $t = v/2\Delta f$. The averaged group velocity of LA phonons in bulk graphite is around 1989 m/s where the group velocities at each wave vector is calculated by $v(q) = d\omega/dq$. Δf is extracted from Figure 8.5 (a) and (b) and $v/2\Delta f$ is then determined. A good agreement is observed between $v/2\Delta f$ and the corresponding MLG thickness t for both Cu/MLG/Cu and Au/MLG/Au structures, which indicates that the transmitting phonons may be dominated by LA phonons. This is also consistent with Ref. [82] where only transmission of LA modes was calculated. Alternatively, the peaks and valleys of transmission function can be interpreted in terms of phonon coupling. Increasing number of graphene layers introduce inter-layer phonon modes in MLG and opens new channels for phonon coupling with phonons in metal contact. The peaks in transmission function represent good coupling between phonons in metal contacts and inter-layer phonon modes of MLG. The peaks of transmission curve are below 4 THz because the phonon modes of MLG in cross-plane direction have a spectrum below 4 THz [252, 254].

In comparison to the transmission function across Cu/SLG/Cu and Au/SLG/Au (Figure 8.4 (a)), the magnitude of transmission function across Cu/MLG/Cu and Au/MLG/Au interfaces does not change significantly. This indicates that the small phonon mismatch between first layer of graphene and the following layers does not introduce a large R_{GG}. Figure 8.5 (c) shows the TBC at Cu/MLG and Au/MLG interfaces as a function of *n*. The TBC increases by 2 to 3 MW/m^{2}K for Cu (~20 to 23 MW/m^{2}K)

or Au contacts (~14 to 17 MW/m^{2}K) when n increases from one to two. Further increasing graphene layers have little effect on TBC for both Cu/MLG and Au/MLG interfaces which is also observed in MD simulations for Cu/MLG/Cu structure in previous studies.[82, 250] This trend seems counterintuitive because adding graphene layers will increase R_{GG} and reduce the overall thermal conductance. Phonon mismatch between the first graphene layer and the following graphene layer caused by the weak physisorption interaction with Cu or Au is small resulting in small R_{GG}. So, R_{MG} dominates the thermal transport while R_{GG} can be negligible for Cu/MLG or Au/MLG interfaces as illustrated in the inset of Figure 8.5 (c).

Recent MD simulations [82, 250] predicted different trend for TBC across Cu/MLG/Cu, i.e., TBC decreases significantly from Cu/SLG/Cu to Cu/MLG/Cu. It should be noted that the L-J potential is used in these studies and corresponding IFCs are much larger than IFCs predicted by the DFT simulations, which will be discussed in the foregoing section on NEMD simulations. IFCs are indications of bonding strength between Cu and graphene. The metal/graphene bonding strength does not only affect the phonon coupling at metal/graphene interfaces but also the phonon coupling among graphene layers; its impact on phonon transmission and TBC can be different for metal/SLG/metal and metal/MLG/metal structures, which will be demonstrated next for Ti/MLG/Ti structure.

8.5.2 Thermal Boundary Conductance across Interfaces of MLG with Ti

In comparison to Cu/MLG or Au/MLG interfaces, Ti/MLG interface has negligible R_{MG} which is reflected in high TBC at Ti/SLG interface (~1000 W/m^{2}K). As

R_{MG} is low, phonon coupling between graphene layers with distinct phonon DOSs and the associated R_{GG} may become important for the thermal transport at Ti/MLG interfaces. Figure 8.6 (a) shows the phonon transmission function across Ti/MLG/Ti structure with *n* from 1 to 25. The transmission across Ti/MLG/Ti structure with three graphene layers (*n*=3) is one order of magnitude smaller than the Ti/SLG/Ti (*n*=1) structure (Figure 8.4 (b)). As *n* increases beyond three, the magnitude of transmission function changes slightly. This suggests good phonon coupling among middle graphene layers and weak phonon coupling at the interface between the first graphene layer and the following layer as expected from the significant mismatch of phonon DOSs (Figure 8.3 (a) and (d)).

Similar to Cu/MLG/Cu and Au/MLG/Au structures, the transmission curves of Ti/MLG/Ti structures also have multiple peaks below 4 THz. But the number of peaks is less than the number of graphene layers by two, which is equal to the number of graphene layers not bonded with Ti contacts. The peaks in transmission curves are associated with the interference between propagating and reflected phonons. The interference effects are only observed for the middle graphene layers in Ti/MLG/Ti structures, which can be explained by the coupling mechanism between phonons in metal contacts and inter-layer phonon modes of MLG. Due to the significant mismatch in phonon DOSs with the middle graphene layers, the two graphene layers bonded to Ti contacts do not contribute in the formation of the inter-layer phonon modes [71, 156] as in the case of Cu/MLG/Cu or Au/MLG/Au structures, and their coupling with Ti contacts does not reflect as peak in transmission curves.

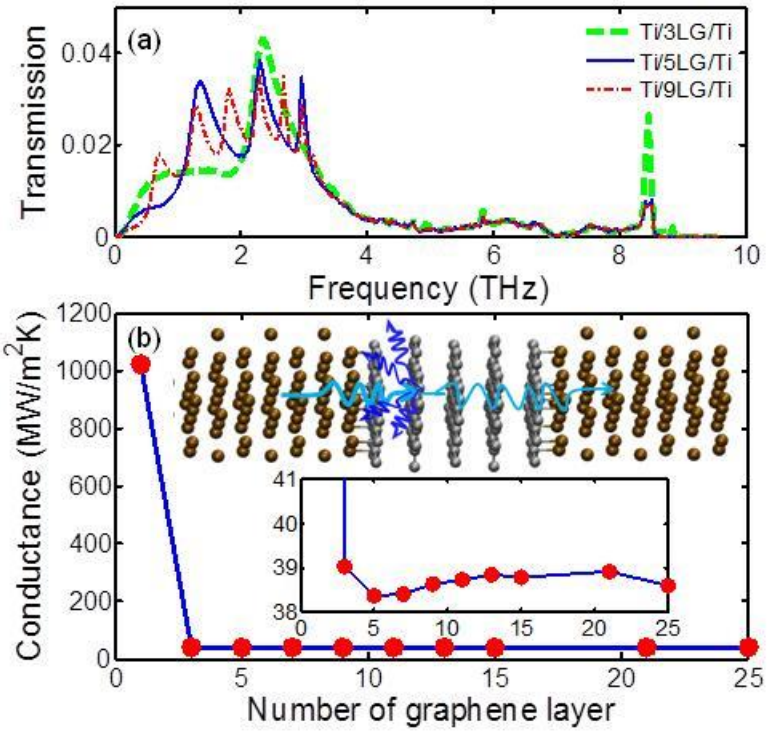

Figure 8.6 (a) Phonon transmission as a function of frequency in Ti/MLG/Ti structures. (b) TBC at Ti/MLG interfaces as a function of number of graphene layers. The upper inset in (b) shows the dominant phonon scattering is at the interface between graphene bonded to Ti and the following graphene layer. The lower inset in (b) shows TBC variations for $n \geq 3$.

The significant reduction in transmission function and TBC in Ti/MLG/Ti structure by increasing *n* from one to three implies the importance of phonon scattering at interfaces between graphene layers due to significant phonon mismatch. Due to the harmonic assumption in AGF calculations, the phonon scattering is not realized among the non-bonded graphene layers of nearly identical phonon DOSs. So, the change in TBC is very small in the Ti/MLG/Ti system as *n* increases beyond three. The AGF calculations

predict TBC of 39 W/m^2K at 300K for smooth Ti/HOPG interfaces, which is in agreement with the experimental measurements of TBC at Ti/HOPG interfaces (~70 - 100 W/m^2K around room temperature) [83, 107, 108]. Most of the experimental measurements have been performed for Ti/HOPG structures or Ti/MLG/SiO_2 structures and so the dramatic decrease of TBC by increasing *n* from one to three has never been reported for metal/MLG/metal structures. It will be worthwhile to examine these using advanced measurement techniques such as time domain thermal reflectance.

Besides, the Ti/graphene interfaces in experiments may not be as smooth and clean as considered in the AGF calculations; the defects and roughness can change the Ti/graphene bonding strength and also number the number of bonded atoms at the interface. The decrease in Ti/graphene bonding strength will increase R_{MG}, but the decrease of Ti/graphene bonding strength can attenuate the mismatch in phonon properties of the first and second graphene layers leading to a decrease in R_{GG}. So, the change in TBC across Ti/MLG/Ti will depend on the interplay between R_{MG} and R_{GG}. To better understand this interplay, it is important to examine how the TBC will change if the bonding strength between Ti/graphene is scaled down.

8.6 Effects of Interfacial Bonding Strength on Thermal Boundary Conductance

The AGF results in previous sections show the interfacial bonding strength have different effects on R_{MG} and R_{GG}. So there is a tradeoff between R_{MG} and R_{GG}, which suggests a method to manipulate TBC across metal/MLG/metal interfaces by tuning bonding strength. A series of AGF calculations on both metal/SLG/metal and metal/MLG/metal structures are carried out by scaling the force constants (using a factor

f) for SLG-metal interactions obtained from the DFT simulations. X-ray photoelectron spectroscopy of thin titanium films deposited on HOPG shows characteristics of partial carbide bonds at the Ti/HOPG interface which depends on the deposition conditions [83]. Changing deposition conditions (*e.g.*, changing energy of sputtering) can be analogous to changing f in the present study.

Figure 8.7 (a) and (b) show the TBC (normalized with TBC G_0 at $f = 1$) at 300 K as a function of scaling factor f for Ti/SLG/Ti, Ti/3LG/Ti, Cu/SLG/Cu and Cu/3LG/Cu structures. Since the bonding strength at chemisorption interface between Ti and graphene is inherently strong, it can be scaled down in order to reduce R_{GG}, but increase R_{MG}. On the contrary, the physisorption interaction at Cu/graphene or Au/graphene interfaces is weak, so it need to be enhanced the bonding strength in order to reduce R_{MG}, but increase R_{GG}.

As shown in Figure 8.7 (a), the normalized TBC G/G_0 across Ti/3LG/Ti interfaces increases with decreasing f, achieves peak value at $f = 0.1$ and then rapidly decreases to zero. But, the G/G_0 across Ti/SLG/Ti interfaces decreases monotonically to zero with the decreasing f because R_{GG} is absent and R_{MG} increases with the decreasing f. At $f = 0.1$, the TBC across Ti/3LG/Ti at 300 K is increased by 100% and reaches 80 W/m^{2}K. Similar to the Ti interfaces, a peak is observed in G/G_0 for Cu/MLG/Cu but not for Cu/SLG/Cu system as f is increased from 1 to 8, as shown in Figure 8.7 (b). Previous non-equilibrium MD studies have shown TBC across Cu/SLG/Cu can be much larger than TBC across Cu/MLG/Cu but TBC for SiO_2/SLG

and SiO_2/MLG interfaces are not very different. The present AGF calculations for the metal/MLG/metal structures with three different metals indicate the metal/graphene bonding strength and phonon coupling among MLG are responsible for the different trends with increasing *n* for different substrates.

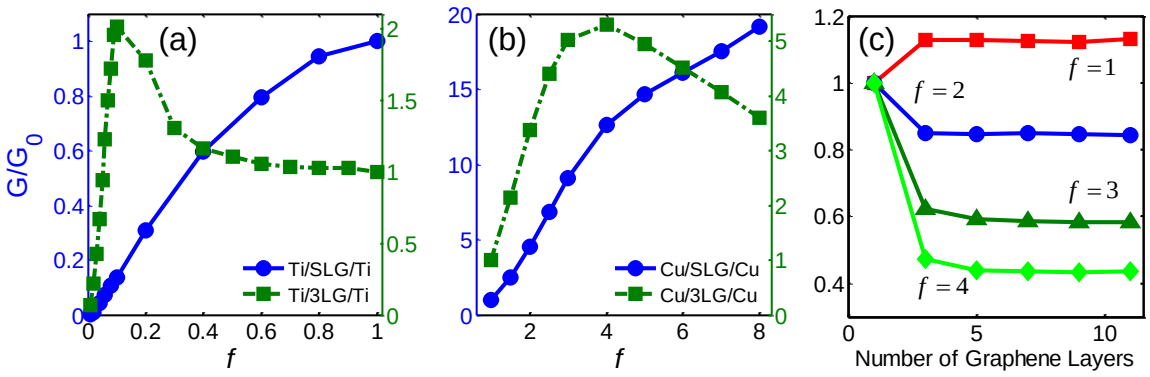

Figure 8.7 Normalized thermal boundary conductance (TBC) G/G_0 as a function of scaling factor f in (a) Ti/SLG/Ti and Ti/3LG/Ti structures, (b) Cu/SLG/Cu and Cu/3LG/Cu structures. G_0 is the TBC in the system with $f=1$. (c) G/G_0 as a function of number of graphene layers n at different f for Cu/MLG/Cu structure. G_0 is the TBC in the system with $n=1$.

Figure 8.7 (c) shows the variations of normalized TBC G/G_0 across Cu/MLG/Cu structure with increasing *n* for different scaling factors f (~1-4). For f equal to one, the TBC increases when *n* is increased from one to two, but this trend in TBC variation with *n* is reversed when f is increased to two. Further increasing f (to 3 or 4) lead to even sharper decrease in TBC when *n* is increased from one to two. TBC is almost constant when $n>3$ for all values of f considered here. Comparison of the reduction in TBC across Cu/MLG/Cu against previous MD simulation results [82, 250] suggests that L-J

potential corresponds to these high values of f. That is why previous MD simulations [82, 250] predict different trend of TBC for Cu/MLG/Cu structures with increasing *n* than the DFT and AGF calculations (f =1) in this work. This also suggests that first principle simulations are important to accurately present the interfacial interactions.

8.7 Non-equilibrium Molecular Dynamics Simulations of Cu/MLG/Cu structures with Different Interaction Strengths

The thermal resistance between non-bonded graphene layers of MLG with similar DOSs is neglected in present AGF calculations due to the harmonic approximations. Since MD naturally includes all anharmonic interactions (Figure 8.8 (a) and (b)), NEMD simulations are performed for the thermal transport across Cu/SLG/Cu and Cu/3LG/Cu structures in order to justify the findings of AGF calculations for metal/MLG/metal interfaces. The interactions between Cu and graphene are described using L-J potential, and the scaling factor χ is used to strengthen the interactions which are similar to scaling up f in the AGF calculations. Figure 8.8 (c) to (h) show the temperature profiles from the heating bath to cooling bath under a constant heating/cooling rate of +/- 45 nW in Cu/SLG/Cu and Cu/3LG/Cu structures with $\chi = 1.0$, $\chi = 0.2$, and $\chi = 4.0$.

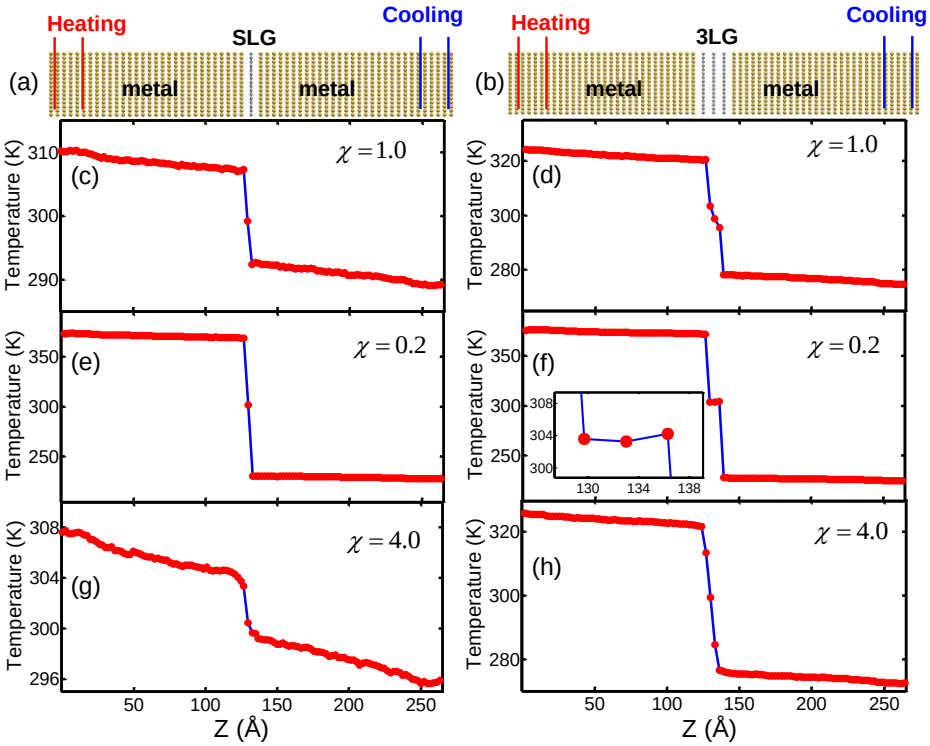

Figure 8.8 Schematic of (a) Cu/SLG/Cu and (b) Cu/3LG/Cu structures for non-equilibrium molecular dynamics simulations. Temperature profiles across Cu/SLG/Cu for (c) χ=1.0, (e) χ=0.2, and (g) χ=4.0 . Temperature profiles across Cu/3LG/Cu for (d) χ=1.0, (f) χ=0.2, and (h) χ=4.0. χ is the scaling factor in Lennard-Jones potential model for Cu/graphene interactions. The inset in (f) shows the close up of temperature profile in three graphene layers.

Table 8.1 summarizes the corresponding results at steady state including the equilibrium spacing between Cu and graphene d_{MG}, the equilibrium spacing between graphene layers d_{GG}, the temperature difference between Cu and graphene ΔT_{MG}, the temperature difference across graphene layers ΔT_{MLG}, and TBC G across the interfaces. As shown in Table 8.1, the change of d_{MG} (~0.01 Å) is negligible as n increases from 1

to 3 when $\chi = 1$. The same interfacial structure indicates same interaction strength between Cu and graphene in the two structures. However, under the same heat flux, ΔT_{MG} increases from 7.3 K to 17.1 K, and ΔT_{MLG} is non-negligible (8.1 K) in Cu/3LG/Cu. As a result, G decreases from 183.5 to 64.9 MW/m^{2}K as shown in Table 8.1.

Table 8.1 NEMD simulation results for heat transfer under constant heat flux across Cu/SLG/Cu and Cu/MLG/Cu structures with different scaling factor χ in Lennard-Jones potential model: equilibrium spacing between Cu and graphene d_{MG}, the equilibrium spacing between graphene layers d_{GG}, the temperature difference between Cu and graphene ΔT_{MG}, the temperature difference across graphene layers ΔT_{MLG}, and TBC G across the interfaces.

	$\chi = 1.0$		$\chi = 0.2$		$\chi = 4.0$	
n	1	3	1	3	1	3
d_{MG} **(Å)**	3	3.01	3.06	3.05	2.99	2.98
d_{GG} **(Å)**	N/A	3.29	N/A	3.31	N/A	3.18
ΔT_{MG} **(K)**	7.3	17.1	68.8	72.2	2.0	8.1
ΔT_{MLG} **(K)**	Neg.	8.1	Neg.	Neg.	Neg.	28.8
G **(MW/m^{2}K)**	183.5	64.9	19.9	19.0	693.4	60.7

The decrease (~65%) in G with increasing n, when $\chi = 1$, is also observed in the NEMD studies by Chang *et al.* [250] and Shen *et al.* [82] Here it is clearly shown, by comparing ΔT_{MG} and ΔT_{MLG} between Cu/SLG/Cu and Cu/3LG/Cu structures, adding graphene layers into Cu/SLG/Cu structures leads to the increase of both R_{MG} and R_{GG}.

As the interaction strength between Cu and graphene is same in Cu/SLG/Cu and Cu/3LG/Cu structures, it can be reasonably inferred that the addition of graphene/graphene interfaces reduces phonon transmission in Cu/3LG/Cu structures when $\chi = 1$.

It is worth noting that TBC predicted by NEMD simulations with L-J potential ($\chi = 1$) is much larger than TBC predicted by AGF calculations using IFCs from the DFT simulations. It implies the interaction strength described by L-J potential is much stronger than that predicted by DFT calculations. Due to the strong Cu/graphene interaction specified by the L-J potential in MD simulations, significant phonon mismatch is created between graphene layer in contact with Cu and the middle graphene layer in the Cu/3LG/Cu structure. Based on the analysis of DOSs using AGF calculations in the previous sections, it can be inferred that the interfacial phonon coupling is weak at graphene/graphene interfaces due to large phonon mismatch. Therefore, in the NEMD simulations, the hot phonons emitted from heating bath will be reflected back to the left Cu contact by graphene/graphene interfaces, which reduces the phonon transmission as well as TBC across Cu/3LG/Cu structure and increases both ΔT_{MG} and ΔT_{MLG}.

For a better comparison between the predictions of NEMD and AGF calculations, it is necessary to use similar interaction strength at Cu/graphene interfaces. So the interaction scaling factor χ is reduced to 0.2 in L-J potential model, and NEMD simulations are performed under the same heat flux. As shown in Table 8.1, TBC predicted by NEMD simulations at $\chi = 0.2$ is significantly reduced to 19.9 and 19.0 MW/m^{2}K for Cu/SLG/Cu and Cu/3LG/Cu structures, respectively, which is comparable to the predictions by AGF calculations. For Cu/3LG/Cu structure, ΔT_{MLG} is not

distinguishable while the temperature difference across Cu/graphene interfaces ΔT_{MG} is noticeable. So TBC only decreases by ~5% as n increase from 1 to 3, which is similar to that of SiO_2/MLG/SiO_2 structures in the NEMD simulations by Shen *et al.*[82]. This also confirms the AGF calculations in present work: the phonon transport is ballistic through MLG in the metal/MLG/metal structure with weak metal/graphene interaction strength.

Similarly, the phonon transport across metal/MLG/metal structures with strong interaction strength is studied by scaling χ to 4 in the NEMD simulations. As shown in Figure 8.8 (g), the temperature variation in Cu/SLG/Cu structure becomes nonlinear near the Cu/graphene interface because the strong interfacial interaction increases phonon scattering and reduces the thermal conductivity of the near-interface region of the semi-infinite Cu contact [255]. With the same interfacial interaction strength ($\chi = 4$), the temperature variation remains linear in the Cu/3LG/Cu structure. This implies the effects of interfacial atomic reconstruction of the metal contact are more important in metal/SLG/metal structure with strong interaction strength. As shown in Table 8.1, ΔT_{MLG} has been larger than ΔT_{MG} in Cu/3LG/Cu at $\chi = 4$, which suggests thermal resistance at graphene/graphene interface becomes more important for metal/MLG/metal structures with strong interaction strength. As a result, TBC decreases by one order of magnitude as n increases from 1 to 3, which is similar to the Ti/SLG/Ti and Ti/MLG/Ti structures in the AGF calculations.

Finally, the results of NEMD simulations demonstrate the increase of ΔT_{GG} with χ because the increasing Cu/graphene interaction strength leads to larger mismatch in phonon DOSs and reduced phonon coupling between the first and middle graphene layer, which is consistent with results of AGF calculations. This also confirms that trends in

TBC with increasing *n* for different metal/MLG/metal structures considered in present work will be valid even after including anaharmonic interactions in the AGF calculations.

8.8 Closure

In summary, the impact of interface bonding on the phonon transmission and TBC at metal/SLG and metal/MLG interfaces is investigated. DFT calculations show strong electron localization at Ti/graphene interface as a result of the chemisorption interactions; these strong interactions significantly change the phonon DOSs of graphene layer in immediate contact with metal. The physisorption interactions of graphene with Cu and Au only change the graphene DOSs around the Brillouin zone-center. Due to this difference in interfacial interactions, the dominant thermal resistance in Cu/MLG/Cu and Au/MLG/Au structures is at the interface of metal and first layer of graphene while the thermal resistance at the interface between the first graphene layer bonded to Ti and middle graphene layers is more important in Ti/MLG/Ti structures.

The AGF calculations show that the TBC can be enhanced through a moderate attenuation of bonding strength at Ti/MLG interfaces which will reduce the mismatch in phonon DOSs between graphene layers and effectively enhance the phonon coupling between Ti and MLG. The findings from AGF calculations and the effects of anharmonic interactions are validated using NEMD simulations for Cu/SLG/Cu and Cu/MLG/Cu structures. This work will enhance the understanding of the phonon-mediated thermal transport at metal/graphene interfaces and provide insights into tuning the TBC across MLG/metal interfaces.

Previous experimental studies are mainly performed on metal/HOPG [84, 108] and metal/graphene/SiO_2 structures [107]. At metal/HOPG interfaces, the measured TBC is expected to be the value across the near-interface region. Due to the limited resolution, it is extremely difficult to exactly extract the TBC at metal/graphene interfaces. Similarly in metal/graphene/SiO_2 structures, the extracted values of TBC at graphene/metal interface subject to the knowledge of TBC at graphene/SiO_2 interfaces. In order to validate the important findings of the bonding strength effects on TBC at graphene/Ti interfaces, experimental measurements of TBC across MLG sandwiched between Ti are suggested. Besides, the proper experimental validation will also require a good characterization of interface condition at metal/MLG interfaces. For example, Raman spectroscopy measurements [94, 256-259] have been used to determine graphene sample quality and the number of layers of MLG. In case of Ti/MLG interfaces with strong chemisorption bonding, the Ti-bonded graphene layer can give different Raman signal since its phonon states have been significantly changed.

CHAPTER 9

SUMMARY AND FUTURE WORK

9.1 Summary of Current Work

In this work, thermal transport at interfaces of CNT and graphene has been studied using multiple atomistic simulation techniques including MD simulations, AGF calculations, DFT calculations and hybrid BTE models. The results and analysis presented in this thesis focus on understanding the phonon transport mechanism at interfaces and their engineering implication in thermal management of electronic devices using CNTs and graphene. The present work can be summarized into three topics as listed below.

Thermal transport at CNT interfaces

MD simulations demonstrate inefficient heat transfer at CNT-CNT junctions by comparing temperature responses of different junction structures under high heating power. The fully suspended CNTs will be prone to early breakdown in a CN-TFT with high density network. The primary energy exchange in CNT-CNT-oxide junctions is through low frequency phonons in the range of 0-10 THz. The energy carried by these low frequency phonons in the CNTs suspended on other CNTs decays in two stages. The second stage seems to corresponds to intra-tube energy exchange from high frequency bands to low frequency bands in top CNT and then to the bottom CNT and substrate.

Analysis of the heat pulse propagation in DWNTs using MD and wavelet methods shows: 1) strong tangential components excited by the heat pulse can propagate

effectively along the tubes, but they are very ineffective in energy transfer between the shells; 2) longitudinal components gain only a small part of the energy during the heating process, and hence they are not effective in energy exchange between shells; 3) energy can be transferred effectively by the radial modes between shells.

Thermal transport at graphene/metal interfaces

Results of equilibrium MD simulations with Green-Kubo method show a thermal conductivity reduction of 28% ~ 44% due to phonon scattering at Cu substrate which strongly depends on the interaction strength at interfaces. Calculations of phonon lifetime using SED approach indicate thermal transport in the isolated SLG is dominated by the three acoustic modes, but the contributions from ZA phonons are remarkably reduced due to the interaction with Cu substrate.

Using AGF and DFT calculations, the thermal boundary conductance is predicted at interfaces across SLG/MLG sandwiched by different metals including Cu, Au, and Ti. The work shows stretching the SLG lattice to match Cu lattice enhances the interfacial interaction which significantly increases the TBC (~ by 59%). Due to different chemistry of interfacial interactions, the dominant thermal resistance in Cu/MLG/Cu and Au/MLG/Au structures is at the interface of metal and first layer of graphene while the thermal resistance at the interface between the first graphene layer bonded to Ti and middle graphene layers is more important in Ti/MLG/Ti structures. The AGF calculations show that the TBC can be enhanced through a moderate attenuation of bonding strength at Ti/MLG interfaces which will reduce the mismatch in phonon DOSs between graphene layers and effectively enhance the phonon coupling between Ti and MLG.

9.2 Suggestions for Future Work

The work in present thesis can be extended and continued in several topics as suggested below.

9.2.1 Heat Transfer Enhancement at CNT Junctions on SiO_2 Substrate

The study in Chapter 4 demonstrates extremely inefficient heat transfer at CNT-CNT junctions, which can lead to early breakdown of the CNT network in TFTs. It is of great importance to enhance the heat transfer at CNT junctions on SiO_2 substrate, especially the CNTs fully suspended by other CNTs. The spectral analysis in Chapter 4 also demonstrates the optical phonons carry majority of heat but they decay slowly to substrate via CNT junctions. Molecular engineering techniques such as chemical functionalization can be explored to improve the contact of CNT junctions with SiO_2 substrate and enhance phonon coupling. Besides, using long and aligned CNT arrays can be another method to avoid the poor contact at CNT junctions in their devices. The atomistic modeling of thermal cross-talk in aligned CNT arrays on SiO_2 should also be explored in detail.

9.2.2 Inelastic Phonon Scattering in Green's Function Method

Harmonic assumption is employed for the AGF calculations in Chapter 7 and Chapter 8. This assumption is valid in present work because the interface scattering due to phonon mismatch dominates the phonon transport in the AGF model of present work. However, inclusion of inelastic phonon scattering can extend the modeling capability of Green's function calculations to thermal transport problems where phonon-phonon

scattering cannot be neglected. Moreover, inclusion of electron-phonon scattering in Green's function formalism is also crucial for the study of electron and phonon transport in metallic materials.

9.2.3 Modeling Electron-Phonon Coupled Transport under Electrical Field

The electron-phonon interaction (EPI) is important and has been extensively studied in the characterization of graphene properties. For example, Raman technique [66-69] is one of the techniques widely used to characterize graphene properties, including measurement of number of graphene layers [257], stacking order measurement of MLG [258, 260], crystallographic orientation of graphene [259], thermal conductivity measurements [66, 67], the strain effects [256], and the doping effects [261]. During the measurements, the heat absorbed by electrons is transferred to phonons via electron-phonon interactions (EPI), followed by the phonon-dominated thermal transport in graphene and heat dissipation to its surroundings such as substrate and contacts. A detailed study on the energy exchange between electrons and phonons can benefit the interpretation of the related experimental measurement.

Beside the characterization of graphene properties, the electron-phonon coupled transport is also crucial in the modeling of Joule heating which has become a challenge in graphene-based nano-electronic devices such as GFETs for high-field high-power applications. The effective heat dissipation from graphene to its surroundings such as dielectric substrate and metal electrode becomes critical for performance [1, 262-264]. However, the energy transport mechanism in graphene nanostructures is complicated by several important elements. Firstly, the low dimensionality of graphene needs special

consideration of the anisotropic transport processes. For example, a mode-dependent transport model should be used to describe the transport of out-of-plane acoustic (ZA) phonons which have very long mean free path in pristine single layer graphene [70, 152]. Secondly, graphene in electronic devices is generally surrounded by complicated structures with different interfacial coupling mechanisms. At the interface of graphene and SiO_2 substrate, phonons are the major heat carriers while the electron contribution can be neglected [162]. At the interface of graphene and metal electrodes, both phonons and electrons are important energy carriers [83, 84, 106, 108]. Thirdly, the thermal transport involves multiple types of energy carriers including electrons and phonons, and the coupling and energy exchange between different types of energy carriers have significant impact on the thermal transport [31]. Finally, the small length and different time scales of carrier relaxation that define the transport process can create highly non-local and non-equilibrium effects which requires a careful treatment of size effects and boundary scattering [217, 265]. In order to properly consider these mechanisms, a hybrid model is required, *e.g.* a BTE based model that can describe ballistic transport of different carriers and electron-phonon interactions.

Besides, high-electric-field effects cannot be ignored in the modeling of coupled electron-phonon thermal transport in transistors. The electron transport behavior under high electric field should be modeled, *e.g.*, integrating the Poisson's equations with electron BTEs. Besides, the electron-phonon interaction under high-electric field is also different from the zero-field conditions. This can be explored in the DFT calculations by applying electric field.

REFERENCES

1. Pop, E., *Energy Dissipation and Transport in Nanoscale Devices.* Nano Research, 2010. **3**(3): p. 147-169.
2. !!! INVALID CITATION !!!
3. Iijima, S., *Helical Microtubules of Graphitic Carbon.* Nature, 1991. **354**(6348): p. 56-58.
4. Iijima, S. and T. Ichihashi, *Single-Shell Carbon Nanotubes of 1-Nm Diameter.* Nature, 1993. **363**(6430): p. 603-605.
5. Wang, X.S., et al., *Fabrication of Ultralong and Electrically Uniform Single-Walled Carbon Nanotubes on Clean Substrates.* Nano Letters, 2009. **9**(9): p. 3137-3141.
6. Flahaut, E., et al., *Gram-scale CCVD synthesis of double-walled carbon nanotubes.* Chemical Communications, 2003(12): p. 1442-1443.
7. Novoselov, K.S., et al., *Electric field effect in atomically thin carbon films.* Science, 2004. **306**(5696): p. 666-669.
8. Ho, Y.H., et al., *Electronic and optical properties of monolayer and bilayer graphene.* Philosophical Transactions of the Royal Society a-Mathematical Physical and Engineering Sciences, 2010. **368**(1932): p. 5445-5458.
9. Nakada, K., et al., *Edge state in graphene ribbons: Nanometer size effect and edge shape dependence.* Physical Review B, 1996. **54**(24): p. 17954-17961.
10. Brady, G.J., et al., *Polyfluorene-Sorted, Carbon Nanotube Array Field-Effect Transistors with Increased Current Density and High On/Off Ratio.* Acs Nano, 2014. **8**(11): p. 11614-11621.
11. Schie ß l, S.P., et al., *Polymer-Sorted Semiconducting Carbon Nanotube Networks for High-Performance Ambipolar Field-Effect Transistors.* Acs Applied Materials & Interfaces, 2014. **7**(1): p. 682-689.
12. Cao, Q., et al., *Medium-scale carbon nanotube thin-film integrated circuits on flexible plastic substrates.* Nature, 2008. **454**(7203): p. 495-U4.
13. Christou, A., *Electromigration and electronic device degradation*. 1994, New York: Wiley. xiv, 343 p.
14. Collins, P.G., et al., *Current saturation and electrical breakdown in multiwalled carbon nanotubes.* Physical Review Letters, 2001. **86**(14): p. 3128-3131.
15. Wei, B.Q., R. Vajtai, and P.M. Ajayan, *Reliability and current carrying capacity of carbon nanotubes.* Applied Physics Letters, 2001. **79**(8): p. 1172-1174.
16. Kreupl, F., et al., *Carbon nanotubes in interconnect applications.* Microelectronic Engineering, 2002. **64**(1-4): p. 399-408.
17. Ngo, Q., et al., *Electron transport through metal-multiwall carbon nanotube interfaces.* Ieee Transactions on Nanotechnology, 2004. **3**(2): p. 311-317.
18. Lin, Y.M., et al., *Operation of Graphene Transistors at Gigahertz Frequencies.* Nano Letters, 2009. **9**(1): p. 422-426.
19. Li, X.L., et al., *Chemically derived, ultrasmooth graphene nanoribbon semiconductors.* Science, 2008. **319**(5867): p. 1229-1232.

20. Wang, X., L.J. Zhi, and K. Mullen, *Transparent, conductive graphene electrodes for dye-sensitized solar cells.* Nano Letters, 2008. **8**(1): p. 323-327.
21. Bai, J.W., et al., *Graphene nanomesh.* Nature Nanotechnology, 2010. **5**(3): p. 190-194.
22. Wang, Y., et al., *Large area, continuous, few-layered graphene as anodes in organic photovoltaic devices.* Applied Physics Letters, 2009. **95**(6).
23. Jo, G., et al., *Large-scale patterned multi-layer graphene films as transparent conducting electrodes for GaN light-emitting diodes.* Nanotechnology, 2010. **21**(17).
24. Kim, B.J., et al., *Large-area transparent conductive few-layer graphene electrode in GaN-based ultra-violet light-emitting diodes.* Applied Physics Letters, 2011. **99**(14).
25. Liu, C.G., et al., *Graphene-Based Supercapacitor with an Ultrahigh Energy Density.* Nano Letters, 2010. **10**(12): p. 4863-4868.
26. McGaughey, A.J.H. and M. Kaviany, *Phonon Transport in Molecular Dynamics Simulations: Formulation and Thermal Conductivity Prediction,* in *Advances in Heat Transfer*, J.P.H.A.B.-C. George A. Greene and I.C. Young, Editors. 2006, Elsevier. p. 169-255.
27. Swope, W.C., et al., *A Computer-Simulation Method for the Calculation of Equilibrium-Constants for the Formation of Physical Clusters of Molecules - Application to Small Water Clusters.* Journal of Chemical Physics, 1982. **76**(1): p. 637-649.
28. Bayin, S.S.u., *Mathematical methods in science and engineering*. 2006, Hoboken, N.J.: Wiley-Interscience. xxvii, 679 p.
29. Sadasivam, S., et al., *The atomistic Green's function method for interfacial phonon transport.* Ann. Rev. Heat Transfer, 2014. **17**: p. 89-145.
30. Loy, J.M., D. Singh, and J.Y. Murthy, *Non-Gray Phonon Transport Using a Hybrid Bte-Fourier Solver.* Ht2009: Proceedings of the Asme Summer Heat Transfer Conference 2009, Vol 2, 2009: p. 601-610.
31. Vallabhaneni, A.K., et al. *A Study of Spatially-Resolved Non-Equilibrium in Laser-Irradiated Graphene Using Boltzmann Transport Equation*. in *ASME 2013 International Mechanical Engineering Congress and Exposition*. 2013. San Diego, California, USA: ASME.
32. Engel, E. and R.M. Dreizler, *Density functional theory : an advanced course*. Theoretical and mathematical physics,. 2011, Heidelberg Germany ; New York: Springer. xv, 531 p.
33. Hohenberg, P. and W. Kohn, *Inhomogeneous Electron Gas.* Physical Review B, 1964. **136**(3B): p. B864-+.
34. Ha, T.J., et al., *Highly Stable Hysteresis-Free Carbon Nanotube Thin-Film Transistors by Fluorocarbon Polymer Encapsulation.* Acs Applied Materials & Interfaces, 2014. **6**(11): p. 8441-8446.
35. Valletta, A., et al., *Self-heating effects in polycrystalline silicon thin film transistors.* Applied Physics Letters, 2006. **89**(9): p. 093509.
36. Kumar, S., et al., *Self-consistent electrothermal analysis of nanotube network transistors.* Journal of Applied Physics, 2011. **109**(1).

37. Estrada, D. and E. Pop, *Imaging Dissipation and Hot Spots in Carbon Nanotube Network Transistors.* Appl. Phys. Lett., 2011. **98**(7): p. 073102.
38. Shekhar, S., et al., *Correlated electrical breakdown in arrays of high density aligned carbon nanotubes.* Appl. Phys. Lett., 2011. **98**(24): p. 243121.
39. Strus, M.C., et al., *Accelerated reliability testing of highly aligned single-walled carbon nanotube networks subjected to DC electrical stressing.* Nanotechnology, 2011. **22**(26): p. 265713.
40. Liao, A., et al., *Thermal dissipation and variability in electrical breakdown of carbon nanotube devices.* Physical Review B, 2010. **82**(20): p. 205406.
41. Ong, Z.Y. and E. Pop, *Frequency and polarization dependence of thermal coupling between carbon nanotubes and SiO2.* Journal of Applied Physics, 2010. **108**(10).
42. Ong, Z.Y. and E. Pop, *Molecular dynamics simulation of thermal boundary conductance between carbon nanotubes and SiO2.* Physical Review B, 2010. **81**(15).
43. Ong, Z.Y., E. Pop, and J. Shiomi, *Reduction of phonon lifetimes and thermal conductivity of a carbon nanotube on amorphous silica.* Physical Review B, 2011. **84**(16).
44. Pop, E., et al., *Electrical and thermal transport in metallic single-wall carbon nanotubes on insulating substrates.* Journal of Applied Physics, 2007. **101**(9): p. 093710.
45. Tsai, C.L., et al., *Electrical power dissipation in semiconducting carbon nanotubes on single crystal quartz and amorphous SiO2.* Applied Physics Letters, 2011. **99**(5).
46. Xu, Z.P. and M.J. Buehler, *Nanoengineering Heat Transfer Performance at Carbon Nanotube Interfaces.* Acs Nano, 2009. **3**(9): p. 2767-2775.
47. Yang, J.K., et al., *Contact thermal resistance between individual multiwall carbon nanotubes.* Applied Physics Letters, 2010. **96**(2): p. 023109.
48. Chalopin, Y., S. Volz, and N. Mingo, *Upper bound to the thermal conductivity of carbon nanotube pellets.* Journal of Applied Physics, 2009. **105**(8): p. 084301.
49. Zhong, H.L. and J.R. Lukes, *Interfacial thermal resistance between carbon nanotubes: Molecular dynamics simulations and analytical thermal modeling.* Physical Review B, 2006. **74**(12): p. 125403.
50. Prasher, R.S., et al., *Turning Carbon Nanotubes from Exceptional Heat Conductors into Insulators.* Phys. Rev. Lett., 2009. **102**(10): p. 105901.
51. Hu, L., D.S. Hecht, and G. Grüner, *Percolation in Transparent and Conducting Carbon Nanotube Networks.* Nano Lett., 2004. **4**(12): p. 2513-2517.
52. Kumar, S., J.Y. Murthy, and M.A. Alam, *Percolating Conduction in Finite Nanotube Networks.* Phys. Rev. Lett., 2005. **95**(6): p. 066802.
53. Lyons, P.E., et al., *The relationship between network morphology and conductivity in nanotube films.* J. Appl. Phys., 2008. **104**(4): p. 044302.
54. Nirmalraj, P.N., et al., *Electrical Connectivity in Single-Walled Carbon Nanotube Networks.* Nano Lett., 2009. **9**(11): p. 3890-3895.
55. Kumar, S., M.A. Alam, and J.Y. Murthy, *Effect of percolation on thermal transport in nanotube composites.* Appl. Phys. Lett., 2007. **90**(10): p. 104105.

56. Fuhrer, M.S., et al., *Crossed Nanotube Junctions.* Science, 2000. **288**(5465): p. 494-497.
57. Javey, A., et al., *High-Field Quasiballistic Transport in Short Carbon Nanotubes.* Phys. Rev. Lett., 2004. **92**(10): p. 106804.
58. Seidel, R.V., et al., *Bias dependence and electrical breakdown of small diameter single-walled carbon nanotubes.* J. Appl. Phys., 2004. **96**(11): p. 6694-6699.
59. Maune, H., H.-Y. Chiu, and M. Bockrath, *Thermal resistance of the nanoscale constrictions between carbon nanotubes and solid substrates.* Appl. Phys. Lett., 2006. **89**(1): p. 013109-3.
60. Varshney, V., et al., *Modeling of Thermal Conductance at Transverse CNT-CNT Interfaces.* Journal of Physical Chemistry C, 2010. **114**(39): p. 16223-16228.
61. Yang, J.K., et al., *Enhanced and switchable nanoscale thermal conduction due to van der Waals interfaces.* Nature Nanotechnology, 2012. **7**(2): p. 91-95.
62. Naeemi, A. and J.D. Meindl, *Carbon Nanotube Interconnects.* Ispd'07: Proceedings of the 2007 International Symposium on Physical Design, 2007: p. 77-84.
63. Naeemi, A. and J.D. Meindl, *Performance benchmarking for graphene nanoribbon, carbon nanotube, and Cu interconnects.* Proceedings of the Ieee 2008 International Interconnect Technology Conference, 2008: p. 183-185.
64. Begtrup, G.E., et al., *Probing nanoscale solids at thermal extremes.* Physical Review Letters, 2007. **99**(15).
65. Liebau, M., et al., *Electrical interconnects made of carbon nanotubes.* Electronic Properties of Synthetic Nanostructures, 2004. **723**: p. 536-539.
66. Balandin, A.A., et al., *Superior thermal conductivity of single-layer graphene.* Nano Letters, 2008. **8**(3): p. 902-907.
67. Ghosh, S., et al., *Extremely high thermal conductivity of graphene: Prospects for thermal management applications in nanoelectronic circuits.* Applied Physics Letters, 2008. **92**(15): p. 151911.
68. Chen, S.S., et al., *Thermal conductivity of isotopically modified graphene.* Nature Materials, 2012. **11**(3): p. 203-207.
69. Cai, W.W., et al., *Thermal Transport in Suspended and Supported Monolayer Graphene Grown by Chemical Vapor Deposition.* Nano Letters, 2010. **10**(5): p. 1645-1651.
70. Seol, J.H., et al., *Two-Dimensional Phonon Transport in Supported Graphene.* Science, 2010. **328**(5975): p. 213-216.
71. Lindsay, L., D.A. Broido, and N. Mingo, *Flexural phonons and thermal transport in multilayer graphene and graphite.* Physical Review B, 2011. **83**(23): p. 235428.
72. Schwierz, F., *Graphene transistors.* Nature Nanotechnology, 2010. **5**(7): p. 487-496.
73. Yu, T.H., et al., *Three-Dimensional Stacked Multilayer Graphene Interconnects.* Ieee Electron Device Letters, 2011. **32**(8): p. 1110-1112.
74. Liao, A.D., et al., *Thermally Limited Current Carrying Ability of Graphene Nanoribbons.* Physical Review Letters, 2011. **106**(25).
75. Zheng, J.X., et al., *Interfacial Properties of Bilayer and Trilayer Graphene on Metal Substrates.* Scientific Reports, 2013. **3**: p. 2081.

76. Giovannetti, G., et al., *Doping graphene with metal contacts.* Physical Review Letters, 2008. **101**(2): p. 026803.
77. Liu, X.J., et al., *Metals on graphene: correlation between adatom adsorption behavior and growth morphology.* Physical Chemistry Chemical Physics, 2012. **14**(25): p. 9157-9166.
78. Adamska, L., et al., *Atomic and electronic structure of simple metal/graphene and complex metal/graphene/metal interfaces.* Physical Review B, 2012. **85**(19): p. 195443.
79. Chalopin, Y., et al., *Large effects of pressure induced inelastic channels on interface thermal conductance.* Applied Physics Letters, 2012. **101**(22): p. 221903.
80. Zhang, G. and H.S. Zhang, *Thermal conduction and rectification in few-layer graphene Y Junctions.* Nanoscale, 2011. **3**(11): p. 4604-4607.
81. Mao, R., et al., *First-principles calculation of thermal transport in metal/graphene systems.* Physical Review B, 2013. **87**(16): p. 165410.
82. Shen, M., P.K. Schelling, and P. Keblinski, *Heat transfer mechanism across few-layer graphene by molecular dynamics.* Physical Review B, 2013. **88**(4): p. 045444.
83. Gengler, J.J., et al., *Limited thermal conductance of metal-carbon interfaces.* Journal of Applied Physics, 2012. **112**(9): p. 094904.
84. Norris, P.M., et al., *Prediction and Measurement of Thermal Transport Across Interfaces Between Isotropic Solids and Graphitic Materials.* Journal of Heat Transfer-Transactions of the Asme, 2012. **134**(2): p. 020910.
85. Chen, L., Z. Huang, and S. Kumar, *Phonon transmission and thermal conductance across graphene/Cu interface.* Applied Physics Letters, 2013. **103**(12): p. 123110
86. Kim, P., et al., *Thermal transport measurements of individual multiwalled nanotubes.* Physical Review Letters, 2001. **8721**(21): p. 215502.
87. Choi, T.Y., et al., *Measurement of thermal conductivity of individual multiwalled carbon nanotubes by the 3-omega method.* Applied Physics Letters, 2005. **87**(1).
88. Yu, C.H., et al., *Thermal conductance and thermopower of an individual single-wall carbon nanotube.* Nano Letters, 2005. **5**(9): p. 1842-1846.
89. Pop, E., et al., *Thermal conductance of an individual single-wall carbon nanotube above room temperature.* Nano Letters, 2006. **6**(1): p. 96-100.
90. Yi, W., et al., *Linear specific heat of carbon nanotubes.* Physical Review B, 1999. **59**(14): p. R9015-R9018.
91. Yang, D.J., et al., *Thermal conductivity of multiwalled carbon nanotubes.* Physical Review B, 2002. **66**(16).
92. Hone, J., et al., *Thermal conductivity of single-walled carbon nanotubes.* Physical Review B, 1999. **59**(4): p. R2514-R2516.
93. Hone, J., et al., *Electrical and thermal transport properties of magnetically aligned single walt carbon nanotube films.* Applied Physics Letters, 2000. **77**(5): p. 666-668.
94. Calizo, I., et al., *Temperature dependence of the Raman spectra of graphene and graphene multilayers.* Nano Letters, 2007. **7**(9): p. 2645-2649.

95. Nika, D.L., et al., *Lattice thermal conductivity of graphene flakes: Comparison with bulk graphite.* Applied Physics Letters, 2009. **94**(20).
96. Chen, S.S., et al., *Raman Measurements of Thermal Transport in Suspended Monolayer Graphene of Variable Sizes in Vacuum and Gaseous Environments.* Acs Nano, 2011. **5**(1): p. 321-328.
97. Lee, J.U., et al., *Thermal conductivity of suspended pristine graphene measured by Raman spectroscopy.* Physical Review B, 2011. **83**(8).
98. Itkis, M.E., et al., *Thermal conductivity measurements of semitransparent single-walled carbon nanotube films by a bolometric technique.* Nano Letters, 2007. **7**(4): p. 900-904.
99. Pop, E., *The role of electrical and thermal contact resistance for Joule breakdown of single-wall carbon nanotubes.* Nanotechnology, 2008. **19**(29).
100. Panzer, M.A., et al., *Temperature-Dependent Phonon Conduction and Nanotube Engagement in Metalized Single Wall Carbon Nanotube Films.* Nano Letters, 2010. **10**(7): p. 2395-2400.
101. Xu, J. and T.S. Fisher, *Enhanced thermal contact conductance using carbon nanotube array interfaces.* Ieee Transactions on Components and Packaging Technologies, 2006. **29**(2): p. 261-267.
102. Cola, B.A., et al., *Effects of growth temperature on carbon nanotube array thermal interfaces.* Journal of Heat Transfer-Transactions of the Asme, 2008. **130**(11).
103. Cola, B.A., et al., *Photoacoustic characterization of carbon nanotube array thermal interfaces.* Journal of Applied Physics, 2007. **101**(5).
104. Cola, B.A., J. Xu, and T.S. Fisher, *Contact mechanics and thermal conductance of carbon nanotube array interfaces.* International Journal of Heat and Mass Transfer, 2009. **52**(15-16): p. 3490-3503.
105. Chen, Z., et al., *Thermal contact resistance between graphene and silicon dioxide.* Applied Physics Letters, 2009. **95**(16).
106. Hopkins, P.E., et al., *Manipulating Thermal Conductance at Metal-Graphene Contacts via Chemical Functionalization.* Nano Letters, 2012. **12**(2): p. 590-595.
107. Koh, Y.K., et al., *Heat Conduction across Monolayer and Few-Layer Graphenes.* Nano Letters, 2010. **10**(11): p. 4363-4368.
108. Schmidt, A.J., et al., *Thermal conductance and phonon transmissivity of metal-graphite interfaces.* Journal of Applied Physics, 2010. **107**(10): p. 104907.
109. Mak, K.F., C.H. Lui, and T.F. Heinz, *Measurement of the thermal conductance of the graphene/SiO2 interface.* Applied Physics Letters, 2010. **97**(22).
110. Wang, C., et al., *Carbon nanotube electronics - moving forward.* Chem. Soc. Rev., 2013. **42**(7): p. 2592-2609.
111. Park, S., M. Vosguerichian, and Z. Bao, *A review of fabrication and applications of carbon nanotube film-based flexible electronics.* Nanoscale, 2013. **5**(5): p. 1727-1752.
112. Zhang, J.L., et al., *Separated Carbon Nanotube Macroelectronics for Active Matrix Organic Light-Emitting Diode Displays.* Nano Letters, 2011. **11**(11): p. 4852-4858.
113. Reuss, R.H., et al., *Macroelectronics: Perspectives on Technology and Applications.* Proc. IEEE, 2005. **93**(7): p. 1239-1256.

114. Ha, M., et al., *Printed, Sub-3V Digital Circuits on Plastic from Aqueous Carbon Nanotube Inks.* ACS Nano, 2010. **4**(8): p. 4388-4395.
115. Kim, S., et al., *Fully Transparent Pixel Circuits Driven by Random Network Carbon Nanotube Transistor Circuitry.* ACS Nano, 2010. **4**(6): p. 2994-2998.
116. Donadio, D. and G. Galli, *Thermal conductivity of isolated and interacting carbon nanotubes: Comparing results from molecular dynamics and the Boltzmann transport equation.* Physical Review Letters, 2007. **99**(25): p. 255502.
117. Berber, S., Y.K. Kwon, and D. Tomanek, *Unusually high thermal conductivity of carbon nanotubes.* Physical Review Letters, 2000. **84**(20): p. 4613-4616.
118. Che, J.W., T. Cagin, and W.A. Goddard, *Thermal conductivity of carbon nanotubes.* Nanotechnology, 2000. **11**(2): p. 65-69.
119. Grujicic, M., G. Cao, and W.N. Roy, *Computational analysis of the lattice contribution to thermal conductivity of single-walled carbon nanotubes.* Journal of Materials Science, 2005. **40**(8): p. 1943-1952.
120. Zhang, W., et al., *Chirality dependence of the thermal conductivity of carbon nanotubes.* Nanotechnology, 2004. **15**(8): p. 936-939.
121. Tersoff, J., *New Empirical-Approach for the Structure and Energy of Covalent Systems.* Physical Review B, 1988. **37**(12): p. 6991-7000.
122. Brenner, D.W., *Empirical Potential for Hydrocarbons for Use in Simulating the Chemical Vapor-Deposition of Diamond Films.* Physical Review B, 1990. **42**(15): p. 9458-9471.
123. Maruyama, S., *A molecular dynamics simulation of heat conduction in finite length SWNTs.* Physica B-Condensed Matter, 2002. **323**(1-4): p. 193-195.
124. Maruyama, S., *A molecular dynamics simulation of heat conduction of a finite length single-walled carbon nanotube.* Microscale Thermophysical Engineering, 2003. **7**(1): p. 41-50.
125. Shiomi, J. and S. Maruyama, *Heat conduction of single-walled carbon nanotube isotope superlattice structures: A molecular dynamics study.* Physical Review B, 2006. **74**(15).
126. Shiomi, J. and S. Maruyama, *Molecular dynamics of diffusive-ballistic heat conduction in single-walled carbon nanotubes.* Japanese Journal of Applied Physics, 2008. **47**(4): p. 2005-2009.
127. Brenner, D.W., et al., *A second-generation reactive empirical bond order (REBO) potential energy expression for hydrocarbons.* Journal of Physics-Condensed Matter, 2002. **14**(4): p. 783-802.
128. Yao, Z.H., et al., *Thermal conduction of carbon nanotubes using molecular dynamics.* Physical Review B, 2005. **71**(8).
129. Zhang, G. and B.W. Li, *Thermal conductivity of nanotubes revisited: Effects of chirality, isotope impurity, tube length, and temperature.* Journal of Chemical Physics, 2005. **123**(11).
130. Padgett, C.W. and D.W. Brenner, *Influence of chemisorption on the thermal conductivity of single-wall carbon nanotubes.* Nano Letters, 2004. **4**(6): p. 1051-1053.
131. Lukes, J.R. and H.L. Zhong, *Thermal conductivity of individual single-wall carbon nanotubes.* Journal of Heat Transfer-Transactions of the Asme, 2007. **129**(6): p. 705-716.

132. Thomas, J.A., et al., *Predicting phonon dispersion relations and lifetimes from the spectral energy density.* Physical Review B, 2010. **81**(8): p. 081411.
133. Evans, W.J., L. Hu, and P. Keblinski, *Thermal conductivity of graphene ribbons from equilibrium molecular dynamics: Effect of ribbon width, edge roughness, and hydrogen termination.* Applied Physics Letters, 2010. **96**(20): p. 203112.
134. Zhang, H.J., G. Lee, and K. Cho, *Thermal transport in graphene and effects of vacancy defects.* Physical Review B, 2011. **84**(11).
135. Hu, J.N., X.L. Ruan, and Y.P. Chen, *Thermal Conductivity and Thermal Rectification in Graphene Nanoribbons: A Molecular Dynamics Study.* Nano Letters, 2009. **9**(7): p. 2730-2735.
136. Hu, J.N., et al., *Tuning the thermal conductivity of graphene nanoribbons by edge passivation and isotope engineering: A molecular dynamics study.* Applied Physics Letters, 2010. **97**(13).
137. Savin, A.V., Y.S. Kivshar, and B. Hu, *Suppression of thermal conductivity in graphene nanoribbons with rough edges.* Physical Review B, 2010. **82**(19).
138. Zhang, H.J., et al., *Isotope Effect on the Thermal Conductivity of Graphene.* Journal of Nanomaterials, 2010.
139. Cao, J.X., et al., *Thermal conductivity of zigzag single-walled carbon nanotubes: Role of the umklapp process.* Physical Review B, 2004. **69**(7).
140. Xiao, Y., et al., *Three-phonon Umklapp process in zigzag single-walled carbon nanotubes.* Journal of Physics-Condensed Matter, 2003. **15**(23): p. L341-L347.
141. Hepplestone, S.P. and G.P. Srivastava, *Phonon-phonon interactions in single-wall carbon nanotubes.* Physical Review B, 2006. **74**(16).
142. Gu, Y.F. and Y.F. Chen, *Thermal conductivities of single-walled carbon nanotubes calculated from the complete phonon dispersion relations.* Physical Review B, 2007. **76**(13).
143. Mingo, N. and D.A. Broido, *Length dependence of carbon nanotube thermal conductivity and the "problem of long waves".* Nano Letters, 2005. **5**(7): p. 1221-1225.
144. Lindsay, L., D.A. Broido, and N. Mingo, *Lattice thermal conductivity of single-walled carbon nanotubes: Beyond the relaxation time approximation and phonon-phonon scattering selection rules.* Physical Review B, 2009. **80**(12).
145. Lindsay, L. and D.A. Broido, *Optimized Tersoff and Brenner empirical potential parameters for lattice dynamics and phonon thermal transport in carbon nanotubes and graphene.* Physical Review B, 2010. **81**(20): p. 205441.
146. Ghosh, S., et al., *Dimensional crossover of thermal transport in few-layer graphene.* Nature Materials, 2010. **9**(7): p. 555-558.
147. Nika, D.L., E.P. Pokatilov, and A.A. Balandin, *Theoretical description of thermal transport in graphene: The issues of phonon cut-off frequencies and polarization branches.* Physica Status Solidi B-Basic Solid State Physics, 2011. **248**(11): p. 2609-2614.
148. Aksamija, Z. and I. Knezevic, *Lattice thermal conductivity of graphene nanoribbons: Anisotropy and edge roughness scattering.* Applied Physics Letters, 2011. **98**(14).

149. Aksamija, Z. and I. Knezevic, *Anisotropy and Edge Roughness Scattering in the Lattice Thermal Conductivity of Graphene Nanoribbons.* Fullerenes, Nanotubes, and Carbon Nanostructures - 219th Ecs Meeting, 2011. **35**(25): p. 195-200.
150. Kong, B.D., et al., *First-principles analysis of lattice thermal conductivity in monolayer and bilayer graphene.* Physical Review B, 2009. **80**(3): p. 033406.
151. Klemens, P.G. and D.F. Pedraza, *Thermal-Conductivity of Graphite in the Basal-Plane.* Carbon, 1994. **32**(4): p. 735-741.
152. Lindsay, L., D.A. Broido, and N. Mingo, *Flexural phonons and thermal transport in graphene.* Physical Review B, 2010. **82**(11): p. 115427.
153. Lindsay, L., D.A. Broido, and N. Mingo, *Diameter dependence of carbon nanotube thermal conductivity and extension to the graphene limit.* Physical Review B, 2010. **82**(16).
154. Singh, D., J.Y. Murthy, and T.S. Fisher, *On the accuracy of classical and long wavelength approximations for phonon transport in graphene.* Journal of Applied Physics, 2011. **110**(11).
155. Singh, D., J.Y. Murthy, and T.S. Fisher, *Spectral phonon conduction and dominant scattering pathways in graphene.* Journal of Applied Physics, 2011. **110**(9).
156. Singh, D., J.Y. Murthy, and T.S. Fisher, *Mechanism of thermal conductivity reduction in few-layer graphene.* Journal of Applied Physics, 2011. **110**(4): p. 044317.
157. McGaughey, A.J.H. and M. Kaviany, *Thermal conductivity decomposition and analysis using molecular dynamics simulations. Part I. Lennard-Jones argon.* International Journal of Heat and Mass Transfer, 2004. **47**(8-9): p. 1783-1798.
158. McGaughey, A.J.H. and M. Kaviany, *Thermal conductivity decomposition and analysis using molecular dynamics simulations - Part II. Complex silica structures.* International Journal of Heat and Mass Transfer, 2004. **47**(8-9): p. 1799-1816.
159. McGaughey, A.J.H. and M. Kaviany, *Quantitative validation of the Boltzmann transport equation phonon thermal conductivity model under the single-mode relaxation time approximation.* Physical Review B, 2004. **69**(9): p. 094303.
160. Balandin, A.A., *Thermal properties of graphene and nanostructured carbon materials.* Nature Materials, 2011. **10**(8): p. 569-581.
161. Nika, D.L., et al., *Phonon thermal conduction in graphene: Role of Umklapp and edge roughness scattering.* Physical Review B, 2009. **79**(15): p. 155413.
162. Ong, Z.Y. and E. Pop, *Effect of substrate modes on thermal transport in supported graphene.* Physical Review B, 2011. **84**(7).
163. Qiu, B. and X.L. Ruan, *Reduction of spectral phonon relaxation times from suspended to supported graphene.* Applied Physics Letters, 2012. **100**(19).
164. Diao, J., D. Srivastava, and M. Menon, *Molecular dynamics simulations of carbon nanotube/silicon interfacial thermal conductance.* Journal of Chemical Physics, 2008. **128**(16).
165. Hu, M., et al., *Interfacial thermal conductance between silicon and a vertical carbon nanotube.* Journal of Applied Physics, 2008. **104**(8).
166. Huxtable, S.T., et al., *Interfacial heat flow in carbon nanotube suspensions.* Nature Materials, 2003. **2**(11): p. 731-734.

167. Shenogin, S., et al., *Role of thermal boundary resistance on the heat flow in carbon-nanotube composites.* Journal of Applied Physics, 2004. **95**(12): p. 8136-8144.
168. Carlborg, C.F., J. Shiomi, and S. Maruyama, *Thermal boundary resistance between single-walled carbon nanotubes and surrounding matrices.* Physical Review B, 2008. **78**(20): p. 205406.
169. Greaney, P.A. and J.C. Grossman, *Nanomechanical energy transfer and resonance effects in single-walled carbon nanotubes.* Physical Review Letters, 2007. **98**(12): p. 125503.
170. Kumar, S. and J.Y. Murthy, *Interfacial thermal transport between nanotubes.* Journal of Applied Physics, 2009. **106**(8): p. 084302.
171. Xu, Z. and M.J. Buehler, *Nanoengineering Heat Transfer Performance at Carbon Nanotube Interfaces.* Acs Nano, 2009. **3**(9): p. 2767-2775.
172. Hu, L., T. Desai, and P. Keblinski, *Determination of interfacial thermal resistance at the nanoscale.* Physical Review B, 2011. **83**(19).
173. Ni, Y.X., Y. Chalopin, and S. Volz, *Few layer graphene based superlattices as efficient thermal insulators.* Applied Physics Letters, 2013. **103**(14): p. 141905.
174. Ni, Y.X., Y. Chalopin, and S. Volz, *Significant thickness dependence of the thermal resistance between few-layer graphenes.* Applied Physics Letters, 2013. **103**(6): p. 061906.
175. Hu, L., T. Desai, and P. Keblinski, *Thermal transport in graphene-based nanocomposite.* Journal of Applied Physics, 2011. **110**(3).
176. Huang, Z., T. Fisher, and J. Murthy, *An atomistic study of thermal conductance across a metal-graphene nanoribbon interface.* Journal of Applied Physics, 2011. **109**(7).
177. Xu, J. and T.S. Fisher, *Enhancement of thermal interface materials with carbon nanotube arrays.* International Journal of Heat and Mass Transfer, 2006. **49**(9-10): p. 1658-1666.
178. Schelling, P.K., S.R. Phillpot, and P. Keblinski, *Comparison of atomic-level simulation methods for computing thermal conductivity.* Physical Review B, 2002. **65**(14): p. 144306.
179. Cuniberti, G., et al., *Control of Thermal and Electronic Transport in Defect-Engineered Graphene Nanoribbons.* Acs Nano, 2011. **5**(5): p. 3779-3787.
180. Landry, E.S., M.I. Hussein, and A.J.H. McGaughey, *Complex superlattice unit cell designs for reduced thermal conductivity.* Physical Review B, 2008. **77**(18): p. 184302.
181. Gale, J.D. and A.L. Rohl, *The General Utility Lattice Program (GULP).* Molecular Simulation, 2003. **29**(5): p. 291-341.
182. Wirtz, L. and A. Rubio, *The phonon dispersion of graphite revisited.* Solid State Communications, 2004. **131**(3-4): p. 141-152.
183. Alfe, D., *PHON: A program to calculate phonons using the small displacement method.* Computer Physics Communications, 2009. **180**(12): p. 2622-2633.
184. Togo, A., F. Oba, and I. Tanaka, *First-principles calculations of the ferroelastic transition between rutile-type and CaCl(2)-type SiO(2) at high pressures.* Physical Review B, 2008. **78**(13).

185. Huang, Z., T.S. Fisher, and J.Y. Murthy, *Simulation of phonon transmission through graphene and graphene nanoribbons with a Green's function method.* Journal of Applied Physics, 2010. **108**(9): p. 094319.
186. Zhang, W., T.S. Fisher, and N. Mingo, *Simulation of interfacial phonon transport in Si-Ge heterostructures using an atomistic Green's function method.* Journal of Heat Transfer-Transactions of the Asme, 2007. **129**(4): p. 483-491.
187. Zhang, W., T.S. Fisher, and N. Mingo, *The atomistic Green's function method: An efficient simulation approach for nanoscale phonon transport.* Numerical Heat Transfer Part B-Fundamentals, 2007. **51**(4): p. 333-349.
188. Estrada, D. and E. Pop, *Imaging dissipation and hot spots in carbon nanotube network transistors.* Applied Physics Letters, 2011. **98**(7): p. 073102.
189. Gupta, M.P., et al., *Impact of thermal boundary conductances on power dissipation and electrical breakdown of carbon nanotube network transistors.* Journal of Applied Physics, 2012. **112**(12): p. 124506.
190. Hata, K., et al., *Water-Assisted Highly Efficient Synthesis of Impurity-Free Single-Walled Carbon Nanotubes.* Science, 2004. **306**(5700): p. 1362-1364.
191. Plimpton, S., *Fast Parallel Algorithms for Short-Range Molecular-Dynamics.* Journal of Computational Physics, 1995. **117**(1): p. 1-19.
192. Stuart, S.J., A.B. Tutein, and J.A. Harrison, *A reactive potential for hydrocarbons with intermolecular interactions.* Journal of Chemical Physics, 2000. **112**(14): p. 6472-6486.
193. Munetoh, S., et al., *Interatomic potential for Si-O systems using Tersoff parameterization.* Computational Materials Science, 2007. **39**(2): p. 334-339.
194. Rappe, A.K., et al., *Uff, a Full Periodic-Table Force-Field for Molecular Mechanics and Molecular-Dynamics Simulations.* Journal of the American Chemical Society, 1992. **114**(25): p. 10024-10035.
195. Ong, Z.Y. and E. Pop, *Molecular dynamics simulation of thermal boundary conductance between carbon nanotubes and SiO(2).* Physical Review B, 2010. **81**(15): p. 155408.
196. Ong, Z.Y., E. Pop, and J. Shiomi, *Reduction of phonon lifetimes and thermal conductivity of a carbon nanotube on amorphous silica.* Physical Review B, 2011. **84**(16): p. 165418.
197. Dresselhaus, M.S. and P.C. Eklund, *Phonons in carbon nanotubes.* Advances in Physics, 2000. **49**(6): p. 705-814.
198. Bandow, S., et al., *Effect of the growth temperature on the diameter distribution and chirality of single-wall carbon nanotubes.* Physical Review Letters, 1998. **80**(17): p. 3779-3782.
199. Saito, R., et al., *Raman intensity of single-wall carbon nanotubes.* Physical Review B, 1998. **57**(7): p. 4145-4153.
200. Carpenter, J.M. and D.L. Price, *Correlated Motions in Glasses Studied by Coherent Inelastic Neutron-Scattering.* Physical Review Letters, 1985. **54**(5): p. 441-443.
201. Maune, H., H.Y. Chiu, and M. Bockrath, *Thermal resistance of the nanoscale constrictions between carbon nanotubes and solid substrates.* Applied Physics Letters, 2006. **89**(1): p. 013109.

202. Grujicic, M., G. Cao, and B. Gersten, *Atomic-scale computations of the lattice contribution to thermal conductivity of single-walled carbon nanotubes.* Materials Science and Engineering B-Solid State Materials for Advanced Technology, 2004. **107**(2): p. 204-216.
203. Ong, Z.Y. and E. Pop, *Frequency and polarization dependence of thermal coupling between carbon nanotubes and SiO(2).* Journal of Applied Physics, 2010. **108**(10): p. 103502.
204. Shiomi, J. and S. Maruyama, *Non-Fourier heat conduction in a single-walled carbon nanotube: Classical molecular dynamics simulations.* Physical Review B, 2006. **73**(20): p. 205420.
205. Osman, M.A. and D. Srivastava, *Molecular dynamics simulation of heat pulse propagation in single-wall carbon nanotubes.* Physical Review B, 2005. **72**(12): p. 125413.
206. Berendsen, H.J.C., et al., *Molecular-Dynamics with Coupling to an External Bath.* Journal of Chemical Physics, 1984. **81**(8): p. 3684-3690.
207. Lau, K.M. and H. Weng, *Climate signal detection using wavelet transform: How to make a time series sing.* Bulletin of the American Meteorological Society, 1995. **76**(12): p. 2391-2402.
208. Torrence, C. and G.P. Compo, *A practical guide to wavelet analysis.* Bulletin of the American Meteorological Society, 1998. **79**(1): p. 61-78.
209. Rao, A.M., et al., *Raman spectroscopy of pristine and doped single wall carbon nanotubes.* Thin Solid Films, 1998. **331**(1-2): p. 141-147.
210. Li, B.W., et al., *Thermal Transport in Suspended and Supported Few-Layer Graphene.* Nano Letters, 2011. **11**(1): p. 113-118.
211. Yu, T.H., et al., *Bilayer Graphene/Copper Hybrid On-Chip Interconnect: A Reliability Study.* Ieee Transactions on Nanotechnology, 2011. **10**(4): p. 710-714.
212. Xu, Z.P. and M.J. Buehler, *Interface structure and mechanics between graphene and metal substrates: a first-principles study.* Journal of Physics-Condensed Matter, 2010. **22**(48): p. 485301.
213. Foiles, S.M., M.I. Baskes, and M.S. Daw, *Embedded-Atom-Method Functions for the Fcc Metals Cu, Ag, Au, Ni, Pd, Pt, and Their Alloys.* Physical Review B, 1986. **33**(12): p. 7983-7991.
214. Tewary, V.K. and B. Yang, *Parametric interatomic potential for graphene.* Physical Review B, 2009. **79**(7).
215. Mohr, M., et al., *Phonon dispersion of graphite by inelastic x-ray scattering.* Physical Review B, 2007. **76**(3).
216. Nilsson, G. and Rolandso.S, *Lattice-Dynamics of Copper at 80 K.* Physical Review B, 1973. **7**(6): p. 2393-2400.
217. Sellan, D.P., et al., *Size effects in molecular dynamics thermal conductivity predictions.* Physical Review B, 2010. **81**(21): p. 214305.
218. Zhang, H., G. Lee, and K. Cho, *Thermal transport in graphene and effects of vacancy defects.* Physical Review B, 2011. **84**(11): p. 115460.
219. Klemens, P.G., *Theory of thermal conduction in thin ceramic films.* International Journal of Thermophysics, 2001. **22**(1): p. 265-275.
220. Minnich, A.J., *Determining Phonon Mean Free Paths from Observations of Quasiballistic Thermal Transport.* Physical Review Letters, 2012. **109**(20).

221. Johnson, J.A., et al., *Direct Measurement of Room-Temperature Nondiffusive Thermal Transport Over Micron Distances in a Silicon Membrane.* Physical Review Letters, 2013. **110**(2).
222. Liao, A.D., et al., *Thermally Limited Current Carrying Ability of Graphene Nanoribbons.* Physical Review Letters, 2011. **106**(25): p. 256801.
223. Gengler, J.J., et al., *Limited thermal conductance of metal-carbon interfaces.* Journal of Applied Physics, 2012. **112**(9).
224. Vallabhaneni, A.K., et al., *Interfacial thermal conductance limit and thermal rectification across vertical carbon nanotube/graphene nanoribbon-silicon interfaces.* Journal of Applied Physics, 2013. **113**(6).
225. Perdew, J.P. and A. Zunger, *Self-Interaction Correction to Density-Functional Approximations for Many-Electron Systems.* Physical Review B, 1981. **23**(10): p. 5048-5079.
226. Shikin, A.M., D. Farias, and K.H. Rieder, *Phonon stiffening induced by copper intercalation in monolayer graphite on Ni(111).* Europhysics Letters, 1998. **44**(1): p. 44-49.
227. Aizawa, T., et al., *Bond Softening in Monolayer Graphite Formed on Transition-Metal Carbide Surfaces.* Physical Review B, 1990. **42**(18): p. 11469-11478.
228. Allard, A. and L. Wirtz, *Graphene on Metallic Substrates: Suppression of the Kohn Anomalies in the Phonon Dispersion.* Nano Letters, 2010. **10**(11): p. 4335-4340.
229. Siebentritt, S., et al., *Surface phonon dispersion in graphite and in a lanthanum graphite intercalation compound.* Physical Review B, 1997. **55**(12): p. 7927-7934.
230. Yanagisawa, H., et al., *Analysis of phonons in graphene sheets by means of HREELS measurement and ab initio calculation.* Surface and Interface Analysis, 2005. **37**(2): p. 133-136.
231. Shikin, A.M., V.K. Adamchuk, and K.H. Rieder, *Formation of quasi-free graphene on the Ni(111) surface with intercalated Cu, Ag, and Au layers.* Physics of the Solid State, 2009. **51**(11): p. 2390-2400.
232. Ducastel.F and Cyrotlac.F, *Moments Developments and Their Application to Electronic Charge Distribution of D-Bands.* Journal of Physics and Chemistry of Solids, 1970. **31**(6): p. 1295-&.
233. Guinea, F., et al., *Effective Two-Dimensional Hamiltonian at Surfaces.* Physical Review B, 1983. **28**(8): p. 4397-4402.
234. Saito, K., J. Nakamura, and A. Natori, *Ballistic thermal conductance of a graphene sheet.* Physical Review B, 2007. **76**(11): p. 115409.
235. Hopkins, P.E., J.C. Duda, and P.M. Norris, *Anharmonic Phonon Interactions at Interfaces and Contributions to Thermal Boundary Conductance.* Journal of Heat Transfer-Transactions of the Asme, 2011. **133**(6): p. 062401.
236. Lyeo, H.K. and D.G. Cahill, *Thermal conductance of interfaces between highly dissimilar materials.* Physical Review B, 2006. **73**(14): p. 144301.
237. Stevens, R.J., L.V. Zhigilei, and P.M. Norris, *Effects of temperature and disorder on thermal boundary conductance at solid-solid interfaces: Nonequilibrium molecular dynamics simulations.* International Journal of Heat and Mass Transfer, 2007. **50**(19-20): p. 3977-3989.

238. Liu, Y.P., W.S. Lew, and L. Sun, *Enhanced weak localization effect in few-layer graphene.* Physical Chemistry Chemical Physics, 2011. **13**(45): p. 20208-20214.
239. Reina, A., et al., *Large Area, Few-Layer Graphene Films on Arbitrary Substrates by Chemical Vapor Deposition.* Nano Letters, 2009. **9**(1): p. 30-35.
240. Hou, J.B., et al., *Graphene-based electrochemical energy conversion and storage: fuel cells, supercapacitors and lithium ion batteries.* Physical Chemistry Chemical Physics, 2011. **13**(34): p. 15384-15402.
241. Brownson, D.A.C. and C.E. Banks, *The electrochemistry of CVD graphene: progress and prospects.* Physical Chemistry Chemical Physics, 2012. **14**(23): p. 8264-8281.
242. Freitag, M., et al., *Energy Dissipation in Graphene Field-Effect Transistors.* Nano Letters, 2009. **9**(5): p. 1883-1888.
243. Kresse, G. and J. Furthmuller, *Efficiency of ab-initio total energy calculations for metals and semiconductors using a plane-wave basis set.* Computational Materials Science, 1996. **6**(1): p. 15-50.
244. Kresse, G. and D. Joubert, *From ultrasoft pseudopotentials to the projector augmented-wave method.* Physical Review B, 1999. **59**(3): p. 1758-1775.
245. Saidi, W.A., et al., *Ab initio atomistic thermodynamics study of the early stages of Cu(100) oxidation.* Physical Review B, 2012. **86**(24): p. 245429.
246. Silvi, B. and A. Savin, *Classification of Chemical-Bonds Based on Topological Analysis of Electron Localization Functions.* Nature, 1994. **371**(6499): p. 683-686.
247. Savin, A., et al., *ELF: The electron localization function.* Angewandte Chemie-International Edition in English, 1997. **36**(17): p. 1809-1832.
248. Steinmann, S.N., Y.R. Mo, and C. Corminboeuf, *How do electron localization functions describe pi-electron delocalization?* Physical Chemistry Chemical Physics, 2011. **13**(46): p. 20584-20592.
249. Huang, Z., T. Fisher, and J. Murthy, *An atomistic study of thermal conductance across a metal-graphene nanoribbon interface.* Journal of Applied Physics, 2011. **109**(7): p. 074305.
250. Chang, S.W., A.K. Nair, and M.J. Buehler, *Geometry and temperature effects of the interfacial thermal conductance in copper- and nickel-graphene nanocomposites.* Journal of Physics-Condensed Matter, 2012. **24**(24): p. 245301.
251. Sadeghi, M.M., M.T. Pettes, and L. Shi, *Thermal transport in graphene.* Solid State Communications, 2012. **152**(15): p. 1321-1330.
252. Sun, K., M.A. Stroscio, and M. Dutta, *Graphite C-axis thermal conductivity.* Superlattices and Microstructures, 2009. **45**(2): p. 60-64.
253. Wei, Z.Y., et al., *Interfacial thermal resistance in multilayer graphene structures.* Physics Letters A, 2011. **375**(8): p. 1195-1199.
254. Nicklow, R., H.G. Smith, and Wakabaya.N, *Lattice-Dynamics of Pyrolytic-Graphite.* Physical Review B, 1972. **5**(12): p. 4951-4962.
255. Shin, S., et al., *Roles of atomic restructuring in interfacial phonon transport.* Physical Review B, 2010. **82**(8): p. 081302.
256. Mohiuddin, T.M.G., et al., *Uniaxial strain in graphene by Raman spectroscopy: G peak splitting, Gruneisen parameters, and sample orientation.* Physical Review B, 2009. **79**(20).

257. Ni, Z.H., et al., *Graphene thickness determination using reflection and contrast spectroscopy.* Nano Letters, 2007. **7**(9): p. 2758-2763.
258. Poncharal, P., et al., *Raman spectra of misoriented bilayer graphene.* Physical Review B, 2008. **78**(11).
259. You, Y.M., et al., *Edge chirality determination of graphene by Raman spectroscopy.* Applied Physics Letters, 2008. **93**(16).
260. Ni, Z.H., et al., *Reduction of Fermi velocity in folded graphene observed by resonance Raman spectroscopy.* Physical Review B, 2008. **77**(23).
261. Das, A., et al., *Monitoring dopants by Raman scattering in an electrochemically top-gated graphene transistor.* Nature Nanotechnology, 2008. **3**(4): p. 210-215.
262. Bae, M.H., et al., *Infrared Microscopy of Joule Heating in Graphene Field Effect Transistors.* 2009 9th Ieee Conference on Nanotechnology (Ieee-Nano), 2009: p. 818-821.
263. Bae, M.H., et al., *Infrared Imaging of Heat Dissipation in Graphene Transistors.* Graphene, Ge/Iii-V, and Emerging Materials for Post-Cmos Applications 2, 2010. **28**(5): p. 51-62.
264. Bae, M.H., et al., *Imaging, Simulation, and Electrostatic Control of Power Dissipation in Graphene Devices.* Nano Letters, 2010. **10**(12): p. 4787-4793.
265. Chen, G., *Size and interface effects on thermal conductivity of superlattices and periodic thin-film structures.* Journal of Heat Transfer-Transactions of the Asme, 1997. **119**(2): p. 220-229.